

# Electromagnetic Wave Scattering from Vegetation

by

XIAOYAN HUANG

Presented to the Faculty of the Graduate School of  
The University of Texas at Arlington in Partial Fulfillment  
of the Requirements  
for the Degree of

DOCTOR OF PHILOSOPHY

THE UNIVERSITY OF TEXAS AT ARLINGTON

August 2006

Copyright © by Xiaoyan Huang 2006  
All Rights Reserved

## **ACKNOWLEDGMENTS**

I would like to take this opportunity to thank the many people that have been helped to the successful completion of this dissertation.

Firstly I wish to express my deepest gratitude to my supervising professor, Prof. Adrian K. Fung, for taking me under his wings and his guidance, patience and insight during my whole study. I would also like to thank him for the time taken to make this dissertation presentable.

Secondly, I would like to thank the rest of my committee members: Professors Jonathan Bredow, Mingyu Lu, Kai-shing Yeung and Qiming Zhang for their good revising suggestions about my dissertation and taking time to be on my dissertation committee.

Thirdly, I would like to thank all the friends and colleagues in University of Texas at Arlington for their friendship and help during UTA.

Finally I would like to express my gratitude to my family. Throughout the past few years, the whole family supported me in pursuing my goal and fulfilling my dreams. I hope to have the chance to do the same thing for them.

May 31, 2006

# **ABSTRACT**

Electromagnetic Wave Scattering from Vegetation

Publication No. \_\_\_\_\_

Xiaoyan Huang, Ph.D.

The University of Texas at Arlington, 2006

Supervising Professor: Adrian K. Fung

This dissertation contains the theoretical study of microwave scattering from vegetated media and the development of microwave scattering models with applications to these media. A vegetation canopy may consist of deciduous or coniferous leaves, branches, and trunks with certain size and orientation distributions. The formulation of the scattering model for each element of the canopy is carried out and its scatter patterns versus its size and orientation for like and cross polarizations are computed and presented. In particular, an extension is made where vegetation with a compound-leaf pattern is considered. For this type of vegetation, several leaves that form a specific pattern will scatter coherently as a group as opposed to each leaf scattering independently. Hence, a basic scattering element is a compound leaf with a specific leaf-pattern. Based on the study of scattering patterns of different vegetation elements, the scattering models for different vegetation media are formulated. For a leafy vegetation, we model it as a scattering layer with a given type of leaf. For a forested area, we treat it as a two-layer medium: the layer on top is the crown layer consisted of leaves and branches and below it is the trunk layer. In order to verify the validity of the theoretical models for different types of vegetation canopy, extensive comparisons between models and measurements are carried out .

# TABLE OF CONTENTS

ACKNOWLEDGMENTS.....	iii
ABSTRACT.....	iv
LIST OF FIGURES.....	vii
LIST OF TABLES.....	xiv
Chapter	
1. INTRODUCTION.....	1
1.1 Motivation.....	1
1.2 Organization of the Dissertation.....	2
2. EXISTING SCATTERING MODELS FOR VEGETATED AREA.....	4
2.1 Introduction.....	4
2.2 Vegetation scattering model developed in Michigan (MIMICS).....	4
2.3 Vegetation scattering model based on the Born approximation.....	7
2.4 Vegetation scattering model developed at UTA.....	7
2.5 Branching model for vegetation.....	7
2.6 Monte Carlo Coherent Scattering Model.....	11
2.7 Vegetation scattering model for an electrically dense medium.....	15
2.8 Limitations of existing vegetation scattering models.....	16
3. MICROWAVE MODELING OF VEGETATION COMPONENTS.....	21
3.1 Introduction.....	21
3.2 Leaf Shape.....	22

3.3 Needle.....	34
3.4 Pinnately compound leaf pattern.....	43
3.5 A cone-like needle cluster pattern.....	56
3.6 Cylinder.....	68
4. SCATTERING FROM LEAFY VEGETATIONS.....	80
4.1 Introduction.....	80
4.2 Scattering Model Description for a Leafy Vegetation.....	80
4.3 Comparison with measurements.....	81
5. SCATTERING FROM A FORESTED AREA.....	86
5.1 Introduction.....	86
5.2 Description of Forest Scattering Model.....	86
5.3 Comparison with Measurements.....	97
6. CONCLUSIONS.....	109
REFERENCES.....	110
BIOGRAPHICAL STATEMENT.....	115

# LIST OF FIGURES

## Figure

2.1 MIMICS Canopy Model.....	6
2.2 Comparison between MIMICS predications and measurements at X-band for walnut orchard.....	6
2.3 A two-scale cluster branching model.....	9
2.4 Two-scale branching model for soybean.....	9
2.5 Two-scale branching model for pine.....	10
2.6 Comparison of branching model predications and measurements for soybean at early days of summer.....	10
2.7 Comparison of branching model predications and measurements for soybean at late days of summer.....	11
2.8 A computer-generated soybean plant.....	13
2.9 The computer-generated maple trees.....	13
2.10 Comparison of Monte-Carlo predictions and measurements for soybean at L-band.....	14
2.11 Comparison of Monte-Carlo predictions and measurements for soybean at L-band.....	14
2.12 Unit volume of cells with the scatterers randomly placed from the centers of the cells.....	16
2.13 A simple leaf.....	17
2.14 Even-pinnately compound leaves.....	18
2.15 Odd-pinnately compound leaves.....	18
2.16 Palmately compound leaves.....	19
2.17 Needles Growing in Cluster.....	19
2.18 Needles Growing Singly.....	20
3.1 The geometry of a Circular or Elliptic Disk.....	23
3.2 VV Scattering Pattern of a circular disc versus the incidence angle.....	29

3.3 HH Scattering Pattern of a circular disc versus the incidence angle.....	30
3.4 VH Scattering Pattern of a circular disc versus the incidence angle.....	30
3.5 VV backscattering coefficient versus the incidence angle with different distribution of the tilt angle $\beta$ at $0^\circ < \alpha < 360^\circ$ .....	32
3.6 VH backscattering coefficient versus the incidence angle with different distribution of the tilt angle $\beta$ at $0^\circ < \alpha < 360^\circ$ .....	32
3.7 VV backscattering coefficient versus the incidence angle (azimuth direction) with different distribution of the azimuth angle $\alpha$ at $0^\circ < \beta < 90^\circ$ .....	33
3.8 VH backscattering coefficient versus the incidence angle (azimuth direction) with different distribution of the azimuth angle $\alpha$ at $0^\circ < \beta < 90^\circ$ .....	33
3.9 Geometry of the needle problem.....	35
3.10 The VV scattering patterns versus the incidence angle for four different needle lengths.....	37
3.11 The HH scattering patterns versus the incidence angle for four different needle lengths.....	38
3.12 The VH scattering patterns versus the incidence angle for four different needle lengths.....	38
3.13 The VV backscattering coefficients versus the incidence angle for different distributions of the tilt angle $\beta$ , when $0^\circ < \alpha < 360^\circ$ .....	40
3.14 The HH backscattering coefficients versus the incidence angle for different distributions of the tilt angle $\beta$ , when $0^\circ < \alpha < 360^\circ$ .....	40
3.15 The VH backscattering coefficients versus the incidence angle for different distributions of the tilt angle $\beta$ , when $0^\circ < \alpha < 360^\circ$ .....	41
3.16 The VV backscattering coefficient versus the incidence angle for different distributions of the azimuth angle $\alpha$ , when $0^\circ < \beta < 90^\circ$ .....	41
3.17 The HH backscattering coefficient versus the incidence angle for different distributions of the azimuth angle $\alpha$ , when $0^\circ < \beta < 90^\circ$ .....	42
3.18 The VH backscattering coefficient versus the incidence angle for different distributions of the azimuth angle $\alpha$ , when $0^\circ < \beta < 90^\circ$ .....	42
3.19 A Pinnately compound leaf.....	43
3.20 Geometry of the scattering problem.....	44
3.21 Theoretical model for an odd-pinnately compound leaf.....	45



3.22 VV Scattering Pattern of a group leaves versus the incidence angle with different radius of each circular disc.....	49
3.23 HH Scattering Pattern of a group leaves versus the incidence angle with different radius of each circular disc.....	50
3.24 VH Scattering Pattern of a group leaves versus the incidence angle with different radius of each circular disc.....	50
3.25 VV Scattering Pattern of a group leaves versus the incidence angle with respective to different spacing between adjacent leaves.....	51
3.26 HH Scattering Pattern of a group leaves versus the incidence angle with respective to different spacing between adjacent leaves.....	51
3.27 VH Scattering Pattern of a group leaves versus the incidence angle with respective to different spacing between adjacent leaves.....	52
3.28 VV Scattering Pattern of a group leaves versus the incidence angle with respective to different number of leaves in a group.....	52
3.29 HH Scattering Pattern of a group leaves versus the incidence angle with respective to different number of leaves in a group.....	53
3.30 VH Scattering Pattern of a group leaves versus the incidence angle with respective to different number of leaves in a group.....	53
3.31 VV backscattering coefficient of a group leaves versus the incidence angle with respective to different distribution of the tilt angle $\beta$ for $0^\circ < \alpha < 360^\circ$ .....	54
3.32 VH backscattering coefficient of a group leaves versus the incidence angle with respective to different distribution of the tilt angle $\beta$ for $0^\circ < \alpha < 360^\circ$ .....	55
3.33 Needles Growing in Clusters.....	56
3.34 Theoretical model for a cluster of needles.....	57
3.35 VV Scattering Pattern of a cluster of needles versus the incidence angle for four different needle lengths (width of the cone is $\pi/3$ , $\Delta\theta = \pi/24$ and $\Delta\phi = \pi/5$ ; dimension of each needle: radius 0.17cm).....	59
3.36 HH Scattering Pattern of a cluster of needles versus the incidence angle for four different needle lengths (width of the cone is $\pi/3$ , $\Delta\theta = \pi/24$ and $\Delta\phi = \pi/5$ ; dimension of each needle: radius 0.17cm).....	60
3.37 HV Scattering Pattern of a cluster of needles versus the incidence angle for four different needle lengths (width of the cone is $\pi/3$ , $\Delta\theta = \pi/24$ and $\Delta\phi = \pi/5$ ; dimension of each needle: radius 0.17cm).....	60

3.38 VV Scattering Pattern of a cluster of needles versus the incidence angle when the number of needles in the $\phi$ -plane changes (width of the cone is $\pi/3$ , $\Delta\theta = \pi/(36)$ and $\Delta\phi = (2\pi)/ringnum$ ; dimension of each needle: length 6.67 cm and radius 0.17cm).....	61
3.39 HH Scattering Pattern of a cluster of needles versus the incidence angle when the number of needles in the $\phi$ -plane changes (width of the cone is $\pi/3$ , $\Delta\theta = \pi/(36)$ and $\Delta\phi = (2\pi)/ringnum$ ; dimension of each needle: length 6.67 cm and radius 0.17cm).....	61
3.40 VH Scattering Pattern of a cluster of needles versus the incidence angle when the number of needles in the $\phi$ -plane changes (width of the cone is $\pi/3$ , $\Delta\theta = \pi/(36)$ and $\Delta\phi = (2\pi)/ringnum$ ; dimension of each needle: length 6.67 cm and radius 0.17cm).....	62
3.41 VV Scattering Pattern of a cluster of needles versus the incidence angle when the number of needles in the $\theta$ -plane changes (width of the cone $=\pi/3$ , $\Delta\theta = \frac{\pi/6}{subnum}$ , $\Delta\phi = \frac{\pi}{2}$ , Dimension of each needle: length 6.67 cm and radius 0.17cm).....	62
3.42 HH Scattering Pattern of a cluster of needles versus the incidence angle when the number of needles in the $\theta$ -plane changes (width of the cone $=\pi/3$ , $\Delta\theta = \frac{\pi/6}{subnum}$ , $\Delta\phi = \frac{\pi}{2}$ , Dimension of each needle: length 6.67 cm and radius 0.17cm).....	63
3.43 VH Scattering Pattern of a cluster of needles versus the incidence angle when the number of needles in the $\theta$ -plane changes (width of the cone $=\pi/3$ , $\Delta\theta = \frac{\pi/6}{subnum}$ , $\Delta\phi = \frac{\pi}{2}$ , Dimension of each needle: length 6.67 cm and radius 0.17cm).....	63
3.44 VV backscattering coefficient for randomly oriented cluster of needles versus the incidence angle with respect to different length of needles( $0 < \beta < 30^\circ$ , $0^\circ < \alpha < 360^\circ$ , width of the cone is $\pi/3$ , $\Delta\theta = \pi/24$ and $\Delta\phi = \pi/5$ ; dimension of each needle: radius 0.17cm).....	64
3.45 HH backscattering coefficient for randomly oriented cluster of needles versus the incidence angle with respect to different length of needles( $0 < \beta < 30^\circ$ , $0^\circ < \alpha < 360^\circ$ , width of the cone is $\pi/3$ , $\Delta\theta = \pi/24$ and $\Delta\phi = \pi/5$ ; dimension of each needle:	

radius 0.17cm).....	65
3.46 VH backscattering coefficient for randomly oriented cluster of needles versus the incidence angle with respective to different length of needles( $0 < \beta < 30^\circ$ , $0^\circ < \alpha < 360^\circ$ , width of the cone is $\pi/3$ , $\Delta\theta = \pi/24$ and $\Delta\phi = \pi/5$ ; dimension of each needle: radius 0.17cm).....	66
3.47 VV backscattering coefficient for randomly oriented cluster of needles versus the incident angle with respective to different length of needles( $30^\circ < \beta < 90^\circ$ , $0^\circ < \alpha < 360^\circ$ , width of the cone is $\pi/3$ , $\Delta\theta = \pi/24$ and $\Delta\phi = \pi/5$ ; dimension of each needle: radius 0.17cm).....	66
3.48 HH backscattering coefficient for randomly oriented cluster of needles versus the incident angle with respective to different length of needles( $30^\circ < \beta < 90^\circ$ , $0^\circ < \alpha < 360^\circ$ , width of the cone is $\pi/3$ , $\Delta\theta = \pi/24$ and $\Delta\phi = \pi/5$ ; dimension of each needle: radius 0.17cm).....	67
3.49 VH backscattering coefficient for randomly oriented cluster of needles versus the incident angle with respective to different length of needles( $30^\circ < \beta < 90^\circ$ , $0^\circ < \alpha < 360^\circ$ , width of the cone is $\pi/3$ , $\Delta\theta = \pi/24$ and $\Delta\phi = \pi/5$ ; dimension of each needle: radius 0.17cm).....	67
3.50 The geometry of the cylinder.....	68
3.51 The VV scattering pattern of a cylinder versus the incidence angle for two different lengths of the cylinder ( $\epsilon_r = 29.6 - j7.1$ ).....	72
3.52 The HH scattering pattern of a cylinder versus the incidence angle for two different lengths of the cylinder ( $\epsilon_r = 29.6 - j7.1$ ).....	73
3.53 The VH scattering pattern of a cylinder versus the incidence angle for two different lengths of the cylinder ( $\epsilon_r = 29.6 - j7.1$ ).....	73
3.54 The VV scattering pattern of a cylinder versus the incidence angle for different radii of the cylinder ( $\epsilon_r = 29.6 - j7.1$ ).....	74
3.55 The HH scattering pattern of a cylinder versus the incidence angle for different radii of the cylinder ( $\epsilon_r = 29.6 - j7.1$ ).....	74
3.56 The VH scattering pattern of a cylinder versus the incidence angle for different radii of the cylinder ( $\epsilon_r = 29.6 - j7.1$ ).....	75

3.57 VV Backscattering Coefficient from half space of randomly oriented clinders versus the incidence angle with repective to different length of cylinders( $0^\circ < \alpha < 360^\circ$ , $0^\circ < \beta < 90^\circ$ , $\epsilon_r = 29.6 - j7.1$ ).....	76
3.58 HH Backscattering Coefficient from half space of randomly oriented clinders versus the incidence angle with repective to different length of cylinders( $0^\circ < \alpha < 360^\circ$ , $0^\circ < \beta < 90^\circ$ , $\epsilon_r = 29.6 - j7.1$ ).....	77
3.59 VH Backscattering Coefficient from half space of randomly oriented clinders versus the incidence angle with repective to different length of cylinders( $0^\circ < \alpha < 360^\circ$ , $0^\circ < \beta < 90^\circ$ , $\epsilon_r = 29.6 - j7.1$ ).....	77
3.60 VV Backscattering Coefficient from half space of randomly oriented clinders versus the incidence angle with repective to different radius of cylinders( $0^\circ < \alpha < 360^\circ$ , $0^\circ < \beta < 90^\circ$ , $\epsilon_r = 29.6 - j7.1$ ).....	78
3.61 HH Backscattering Coefficient from half space of randomly oriented clinders versus the incidence angle with repective to different radius of cylinders( $0^\circ < \alpha < 360^\circ$ , $0^\circ < \beta < 90^\circ$ , $\epsilon_r = 29.6 - j7.1$ ).....	78
3.62 VH Backscattering Coefficient from half space of randomly oriented clinders versus the incidence angle with repective to different radius of cylinders( $0^\circ < \alpha < 360^\circ$ , $0^\circ < \beta < 90^\circ$ , $\epsilon_r = 29.6 - j7.1$ ).....	79
4.1 Comparison of model calculations for VV backscattering coefficient with measurements from soybean at 1.1 GHz.....	83
4.2. Comparison of model calculations for VH backscattering coefficient with measurements from soybean at 1.1 GHz.....	84
4.3 Comparison of model calculations for VV Backscattering coefficient with measurements from soybean at 4.25 GHz.....	84
4.4 Comparison of model calculations for VH Backscattering coefficient with measurements from soybean at 4.25 GHz.....	85
4.5. Comparison of model calculations for VV and HH backscattering coefficients with measurements from soybean at 8.6 GHz.....	85
5.1 Geometry of a forested area.....	86
5.2 Scattering Mechanisms of the Zeroth-Order Solution.....	88
5.3 Scattering Mechanisms of the First-Order Solution.....	93

5.4 Crown-Crown interaction:. The incident signal is scattered upward twice before propagating towards the receiving antenna.....	93
5.5 Crown-Crown interaction:. The incident signal is scattered downward first and then upwards towards the receiving antenna.....	94
5.6 Behavior of Backscattering Coefficient of different scatterers(needle, cylinder) versus to variation of frequency.....	97
5.7 The probability distribution of the inclination angles for branch 1.....	100
5.8 The probability distributions of the inclination angles for branch 2.....	101
5.9 The probability distributions of the inclination angles for branch 3.....	101
5.10 The probability distributions of the inclination angles for branch 4.....	102
5.11 The probability distributions of the inclination angles for trunk.....	102
5.12 Comparison on backscattering coefficient between model predications and measure- ment data of walnut orchard at 9.6 GHz (X-band).....	103
5.13 Comparison on VV backscattering coefficient between model predications and measure- ment data of walnut orchard at 9.6 GHz (X-band).....	104
5.14 Comparison on HH backscattering coefficient between model predications and measure- ment data of walnut orchard at 9.6 GHz (X-band).....	104
5.15 Comparison on VH backscattering coefficient between model predications and measure- ment data of walnut orchard at 9.6 GHz (X-band).....	105
5.16 Comparison on backscattering coefficient between model predictions and measurement data of Japanese Cypress at 9.9 GHz (X-band).....	107
5.17 Comparison on backscattering coefficient between model predictions and measurement data of Japanese Cypress at 4.0 GHz (C-band).....	107
5.18 Comparison on backscattering coefficient between model predictions and measurement data of Japanese Cypress at 2.75 GHz (S-band).....	108

## LIST OF TABLES

Table

4.1. Soybean parameters used in the model for comparison with measurement.....	82
5.1. Parameters of the Crown Layer for Modeling a Walnut Orchard.....	99
5.2. Parameters of the Trunk Layer and Ground Surface for Modeling Walnut Orchard.....	100
5.3. Parameters Used in the Model Computation for Comparison with Japanese Cypress Measurement.....	106

# CHAPTER 1

## INTRODUCTION

### 1.1 Motivation

Vegetated areas have always been important to humans. For centuries, human beings have benefited economically from the use of forest resources. The vegetation cover plays an important role in environmental protection. Its foliage intercepts rainfall, causing absorptive and evaporative losses that reduce rainfall available for infiltration. Its roots and stems increase the roughness of the ground surface and the permeability of the soil, leading to increased infiltration capacity. Its leaves will absorb the  $CO_2$ , and further reduce atmospheric concentrations of  $CO_2$ , thus mitigating climate change. Therefore, it is necessary to find a good method to monitor the growth and changes in vegetation cover. Since the invention of remote sensing, it has evolved into an important tool for monitoring the status of vegetation canopy. The remote sensing may be separated into two categories based on the frequency band: optical remote sensing and microwave remote sensing. Optical remote sensing makes use of visible, near infrared and short-wave infrared sensors to form images of the earth's surface by detecting the solar radiation reflected from targets on the ground. Different materials reflect and absorb differently at different wavelengths. Thus, the targets can be differentiated by their spectral reflectance signatures in the remotely sensed images. Microwave sensing encompasses both active and passive forms of remote sensing. Passive microwave sensing is similar in concept to thermal remote sensing. A passive microwave sensor detects the naturally emitted microwave energy within its field of view. Active microwave sensors provide their own source of

microwave radiation to illuminate the target. Among the electromagnetic sources used in remote sensing applications, microwave remote sensing is gradually becoming important comparing with other sensors. This is because the microwave active sensors have their own illumination sources which allow them to work in all weather conditions. Over the last few decades,. microwave remote sensing applications in areas such as agriculture, forestry, ocean, sea ice, weather, water contents in snow fields, etc. have been developed and an abundance of relevant data has been collected and made available. Theoretical microwave scattering models have been developed to support the design of experiments and the understanding of the mechanisms involved in the scattering process. Unlike optical remote sensing the sensing wavelength is much longer at microwave frequencies. Hence, scattering is sensitive to both geometrical and physical characteristics of the vegetation canopy. A validated scattering model is useful for the retrieval of vegetation parameters and for classification studies. Thus, an accurate development of scattering models for a vegetation canopy is very important.

## **1.2 Organization of the Dissertation**

This dissertation is divided into a total of six chapters with the first one serving as an introduction. In Chapter 2, existing vegetation scattering models are reviewed briefly. In Chapter 3, the scattering properties of the basic elements of a vegetation canopy are presented. Illustrations are given showing the effects of the look angle, frequency, and polarization for each element. The scattering model for a leafy vegetation layer is formulated in Chapter 4. The theoretical predictions of such a model are first presented showing the effects of look angle, frequency, polarization, the size of the leaf and its orientation distributions. Then, comparisons between model predictions and measurements are shown. Chapter 5 contains the scattering model description for a forested area which may be of a deciduous or coniferous type. Gener-



ally, we expect the major scattering elements to be the leaves, branches, ground and trunk-ground interactions. A frequency study is carried out showing that different forest components may be dominating the scattering at different frequencies and/or look angles. The comparisons of theoretical predictions with measurements are shown to illustrate the relevance of the models presented. Finally, some conclusions and future research directions are presented in Chapter 6.

## **CHAPTER 2**

# **MICROWAVE SCATTERING MODELS FOR VEGETATION**

### **2.1 Introduction**

Over the years, various theoretical models [1~20] have been developed to study scattering mechanisms in the vegetation medium. The Michigan Microwave Canopy Scattering model (MIMICS) [1~3] used the first order radiative transfer solution to model wave scattering from vegetation. Born approximation [4, 5] was used to compute the backscatter from the forest. In [6~8], a more general scattering model based on the second order radiative transfer solution was generated. The coherence effects of clustered structures such as cylinder clusters in a multilayer model were considered and included in the branching model [9~11] for vegetation. The Monte Carlo approach to model coherent scattering from realistic tree structures was developed in [12~15] by including the relative phase difference between the scattered fields from different tree components. Recently, another vegetation model [18~20] was developed to account for scattering from vegetations where media can be considered electrical dense. This was done by making use of the antenna array concept to account for coherent scattering from a compound leaf.

### **2.2 Michigan Microwave Canopy Scattering Model (MIMICS)**

In [1~3], the MIMICS describes the canopy as having three regions (Figure 2.1): the crown region, the trunk region and the underlying ground region. The crown region is made up of leaves and branches where leaves are modeled as rectangular disks in the case of deciduous

canopies or as thin cylinders (or needles) in the case of coniferous canopies. The trunk region only contains trunks. Both the branches and trunks are modeled as finite-length, lossy dielectric cylinders. The underlying ground surface is assumed randomly rough characterized by a rms height and a correlation function. The dielectric constants of the branches, the leaves, the trunks and the ground surface are determined in terms of the moisture content, microwave frequency and physical temperature. The model is based on the first-order solution of the radiative transfer equation under the following assumptions: (1) The direct contribution from the trunk in the backscattering direction and the cross-polarization term in the phase matrix of the trunk can be ignored; (2) In forming the crown-ground and trunk-ground term, the ground is assumed to be flat; (3) The forward scattering theorem can be applied to compute the extinction coefficient within the canopy; and (4) Only single scattering is considered. There exists two major weaknesses in the MIMICS model. The assumption that the extinction coefficient within the canopy can be calculated by applying the forward scattering theorem is not valid in the first order solution, because it can only provide the loss due to absorption. The loss due to scattering is missing in the scattered field expression. The assumption where only single scattering is considered will be appropriate for low frequencies and sparse vegetation and may not be valid at high frequencies or for dense vegetation where contributions to the cross polarized backscattering coefficient from multiple scattering is significant. This is the reason why the model predictions from MIMICS were found lower than measurements at X-band (9.6 GHz) as shown in Figure 2.2.

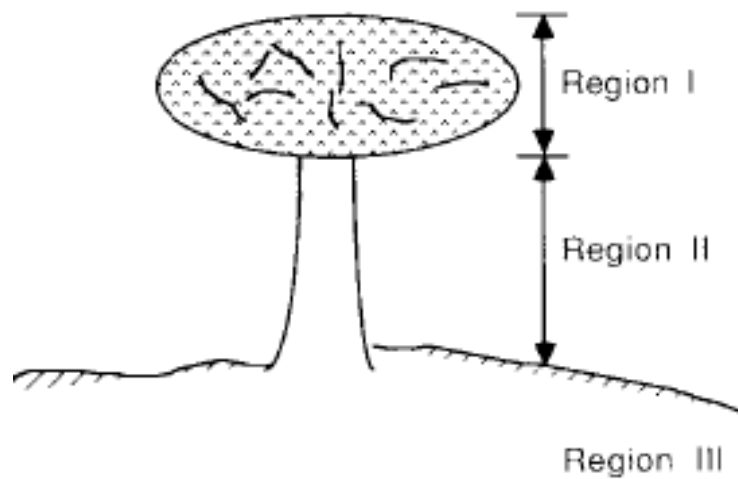


Figure 2.1 MIMICS Canopy Model

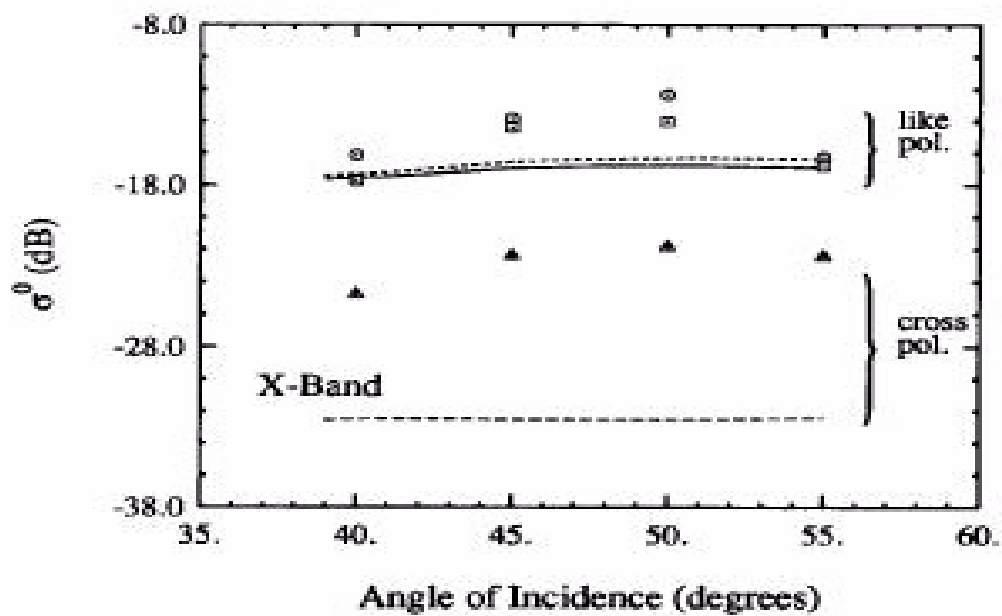


Figure 2.2 Comparison between MIMICS predictions and measurements at X-band for walnut orchard.

## **2.3 Vegetation Model Based on the Distorted Born Approximation**

The distorted born approximation assumes that the field inside a volume layer is the sum of a fluctuating and an average part. The scatterers are replaced by an equivalent medium with a mean and a fluctuating permittivity. The scattering coefficient is obtained by computing the correlation of the fluctuating part of the scattered field and taking its transverse fourier transform. In [4] and [5], the GWU canopy model is based on the distorted born approximation where the canopy is described as a one-layer medium over a rough surface.

## **2.4 Vegetation Model Developed at UTA**

In [6~8], a more generalized canopy model based on the radiative transfer formulation has been developed by including the second-order radiative transfer solution. The following assumptions were made: (1) Expand the radiative transfer formulation to the second-order to account for multiple scattering which is important at high frequencies and for cross polarization in the backscattering direction; (2) Extinction coefficient is computed by the sum of Ohmic and scattering losses, when low frequency approximations are made; (3) In the crown-ground and trunk-ground interaction term, the surface roughness effects are considered; (4) Including cross-polarized scattering from trunk-ground interaction. The weakness of this model is that it assumes that each scatterer scatters independently which may not be valid for the vegetation with compound leaf pattern or the electrically dense vegetation medium, where coherence among adjacent scatterers could be very significant.

## **2.5 Branching Model for Vegetation**

In the branching model a vegetation is modeled as a two-scale vegetation cluster with some smaller cylinders attached to a large cylinder as shown in Figure 2.3. A soybean plant [10] has

been modeled according to the branching model idea as a two-scale branching structure as shown in Figure 2.4 and a pine [9][11] as a two-scale branching structure as shown in Figure 2.5. These branching structures have significant impact on shaping the backscattering angular trends, because the scattering from each element of the structure is added coherently to the other. Here all the branch elements were assumed to be statistically identical, independent of their growth locations and independent of the center trunk. The scattered field of a vegetation component such as a leaf, a branch or a trunk is computed as an independent scatterer. The collective scattering effect of the cluster is accounted for by adding the phase shift due to the relative positions of scatterers in the calculation of the total scattered field. The model does not account for multiple scattering. Its prediction was compared with soybean data at C-band and with the pine forest data at P-band. For the soybean, the model prediction fitted the data very well for leaf fraction greater than 0.2% as shown Figure 2.7. But the model prediction as shown in Figure 2.6 were higher than the measured data at low incident angles for leaf fraction less than 0.2% (which stands for the early days of summer). The model prediction was presented as a function of age for the pine forest. Its predictions were acceptable for both co-polarization and cross-polarization.

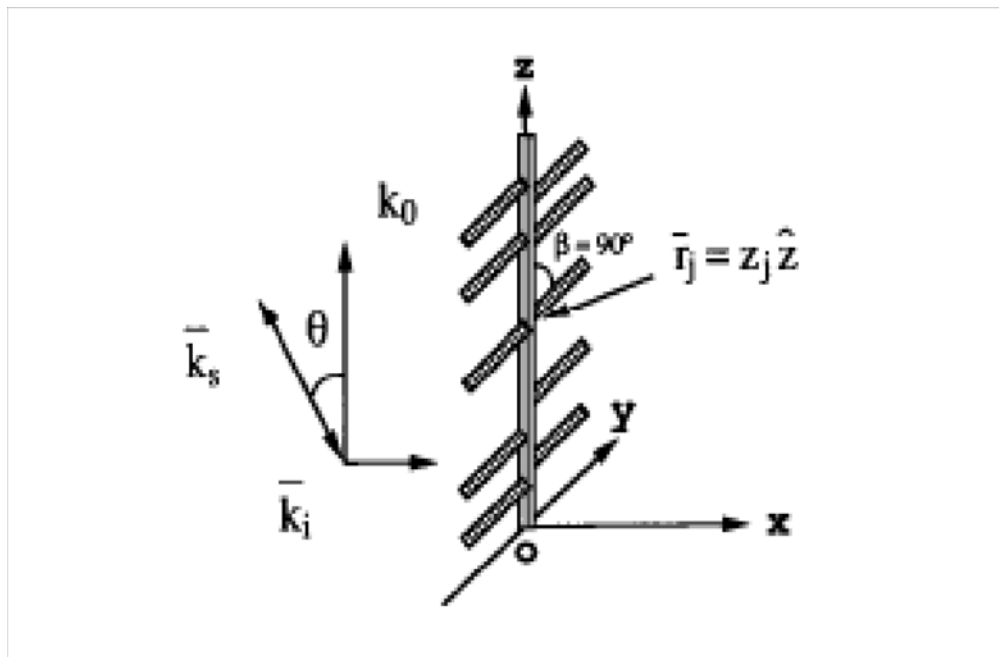


Figure 2.3 A two-scale cluster branching model

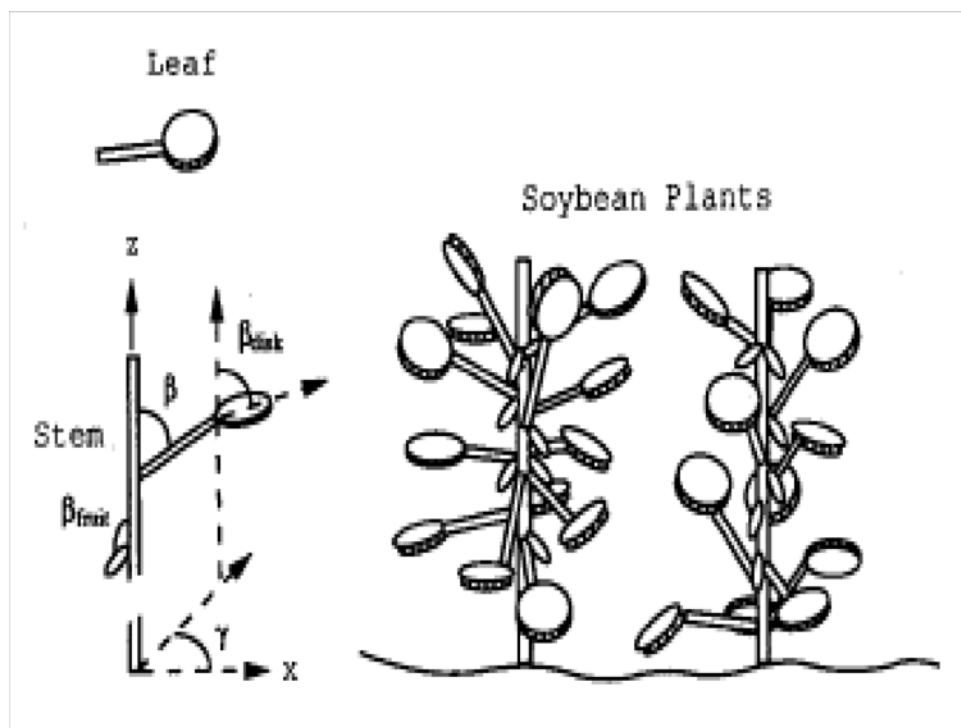


Figure 2.4 Two-scale branching model for soybean

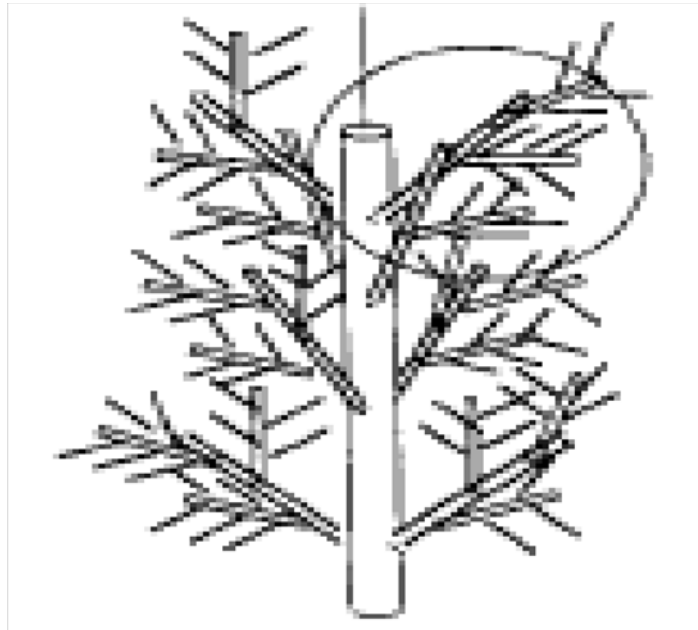


Figure 2.5 Two-scale branching model for pine

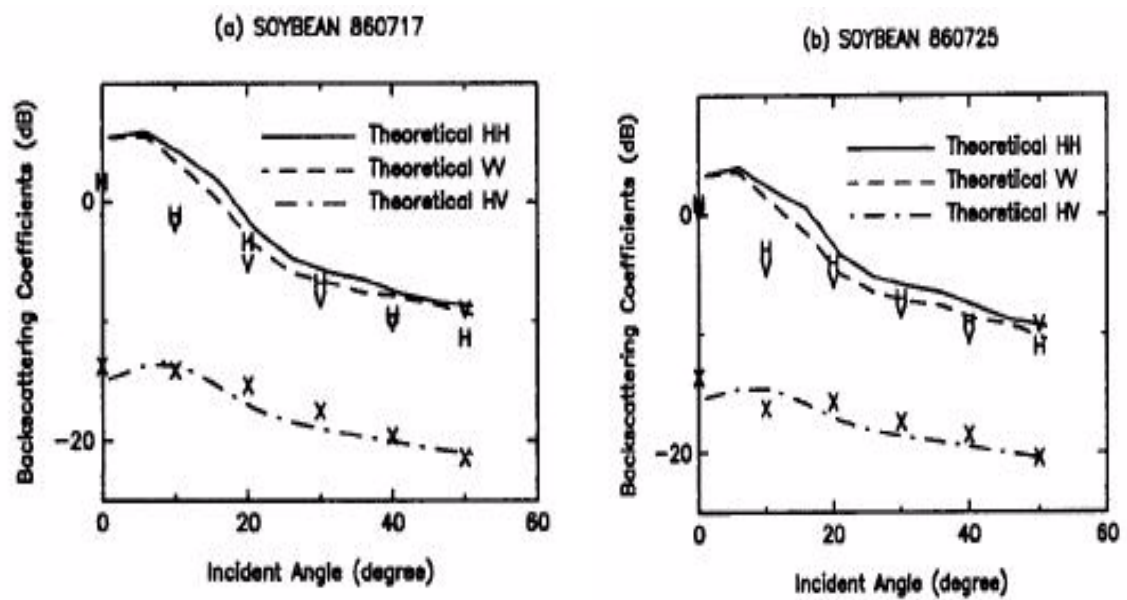


Figure 2.6 Comparison of branching model predictions and measurements for soybean at early days of summer



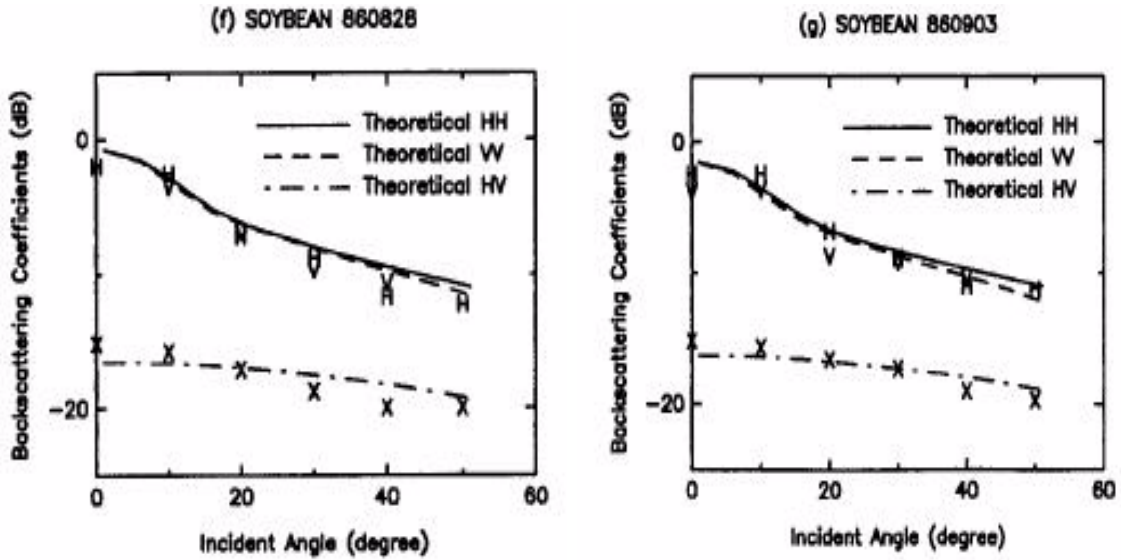


Figure 2.7 Comparison of branching model predications and measurements for soybean at late days of summer

## 2.6 Monte Carlo Coherent Scattering Model

In [12~15], the Monte Carlo scattering model was presented as a simulation tool to account for scattering from a vegetated environment. It contains three major steps as follows:

First, an accurate generation of a tree structure based on a few physical parameters is carried out using fractal-based L-systems incorporating the desired ground truth data. The branches and tree trunks are modeled by dielectric cylinders and leaves are modeled by dielectric disks or needles. Secondly, after the tree generation, individual tree components located above a dielectric plane are illuminated by the mean field and the scattered fields of tree components are computed independently and added coherently. Finally, a Monte Carlo simulation is performed on a large number of fractal-generated trees to establish the statistics of the back-scattered signals. The mean field at a given point within the tree structure, including the phase

change and attenuation due to the scattering and absorption loss of vegetation particles, is computed using Foldy's approximation.

The Monte Carlo scattering model has been applied to compute the scattered field of a typical computer-generated soybean and a maple tree with and without leaves by the L-system as shown in Figure 2.8 and Figure 2.9. The calculated results are compared with measurements for soybean and maple plants using the SIR-C data at L-band and C-band. For L-band in Figure 2.10, VV, HH, and VH polarization agree with the data very well. For C-band as shown in Figure 2.11, VV and HH polarization seem to fit the data well, but there is a clear difference between the model prediction and data, when the incident angle is less than 40 degree in VH polarization. The advantages of this model are: (1) Preserves the effect of the architectural structure of a given tree; (2) Provides complete statistics of the scattered field instead of just its second moment; (3) Simulates the scattering from forest canopies on a titled ground surface. Realistically, it is impossible to gather such detailed information about a vegetated area to obtain computer-generated vegetation by the L-system. The scattering contributions from higher order interactions among scatterers are not included. The assumption that each vegetation component scatters independently is generally not true.



Figure 2.8 A computer-generated soybean plant

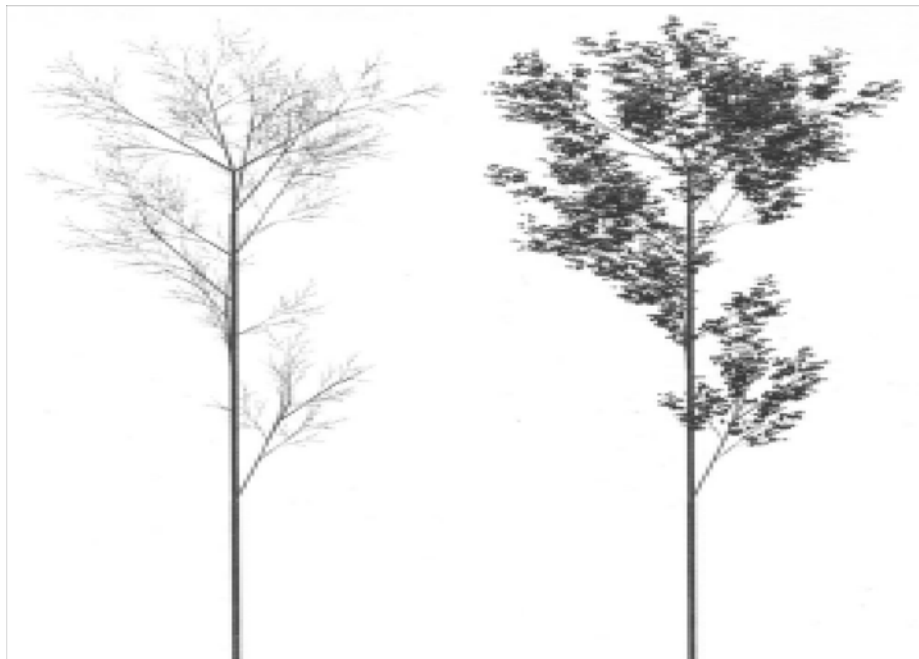


Figure 2.9 The computer-generated maple trees

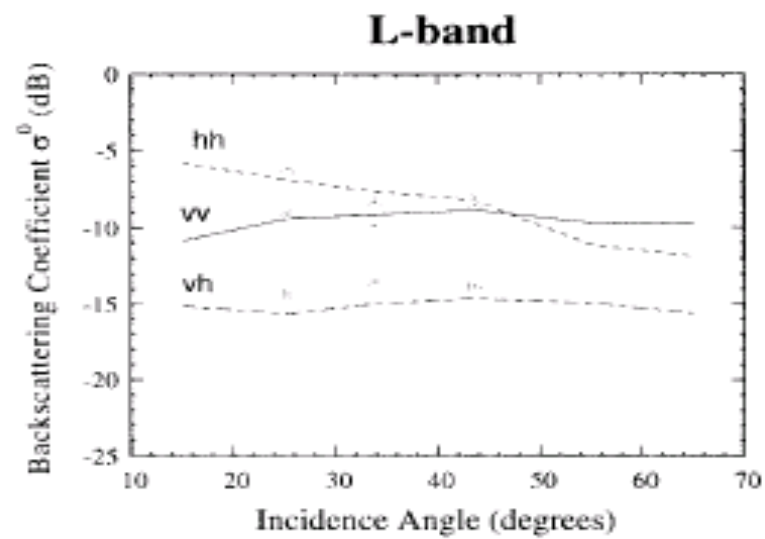


Figure 2.10 Comparison of Monte-Carlo predictions and measurements for soybean at L-band.

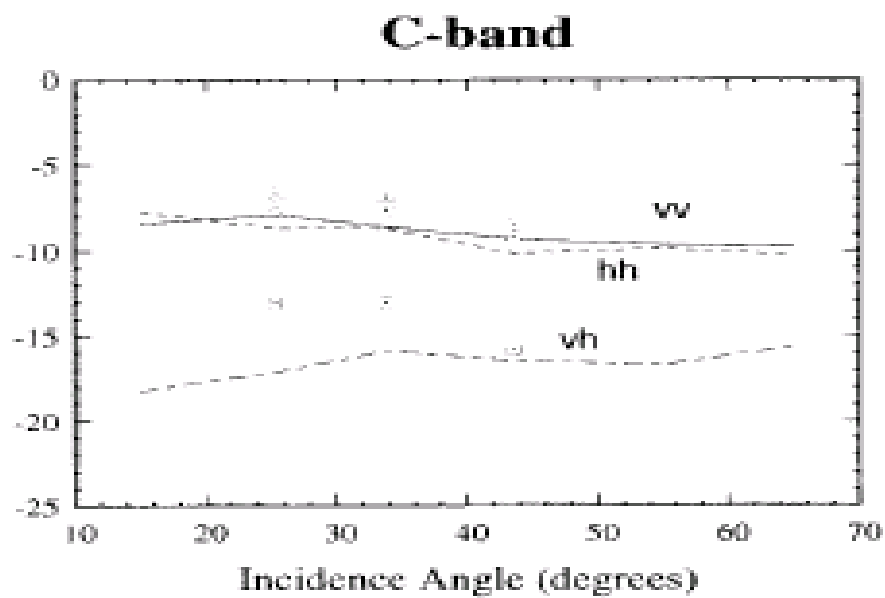


Figure 2.11 Comparison of Monte-Carlo predictions and measurements for soybean at L-band.

## 2.7 Vegetation model for an electrically dense vegetation medium

This scattering model [18~20] has been developed to model the case where the spacing between the scatterers is comparable or smaller than the exploring wavelength where the assumption of independent scattering by individual scatterers is no longer valid. The coherent effect from the various correlated scatterers is calculated by introducing the array phase correction to the phase matrices of the scatterers. The approach of this method is summarized in the next paragraph.

A unit volume as shown in Figure 2.12 has been divided into  $M$ ,  $N$  and  $P$  cells along  $x$ ,  $y$  and  $z$  directions, respectively. The distance between the centers of adjacent cells is  $d$ . A collection of identical ellipsoidal scatterers are randomly placed inside the cells. The scattered field from each scatterer in cell  $[m, n, p]$  from certain incident field can be calculated and the total scattered field is obtained by the vector sum of scattered fields from all the scatterers in a unit volume. For random medium with multiple classes of scatters, the phase matrix of each class of scatterers with array phase correction can be calculated separately and add together to obtain the total phase matrix. The model is based on the second order solution of the radiative transfer theory where multiple scattering has been included.

Comparisons with the measurements of Japanese cypress [21], boreal forest [4], Soybean and Wheat [22], Walnut [2] and Sugi coniferous trees [23] were made. Generally, there is a good agreement in the level but not necessary the angular trends. The contribution due to the coherence among leaves has been accounted for in the model but the specific pattern of leaves was not considered. This may be the reason why its model prediction cannot follow the angular trends observed in some measurements.

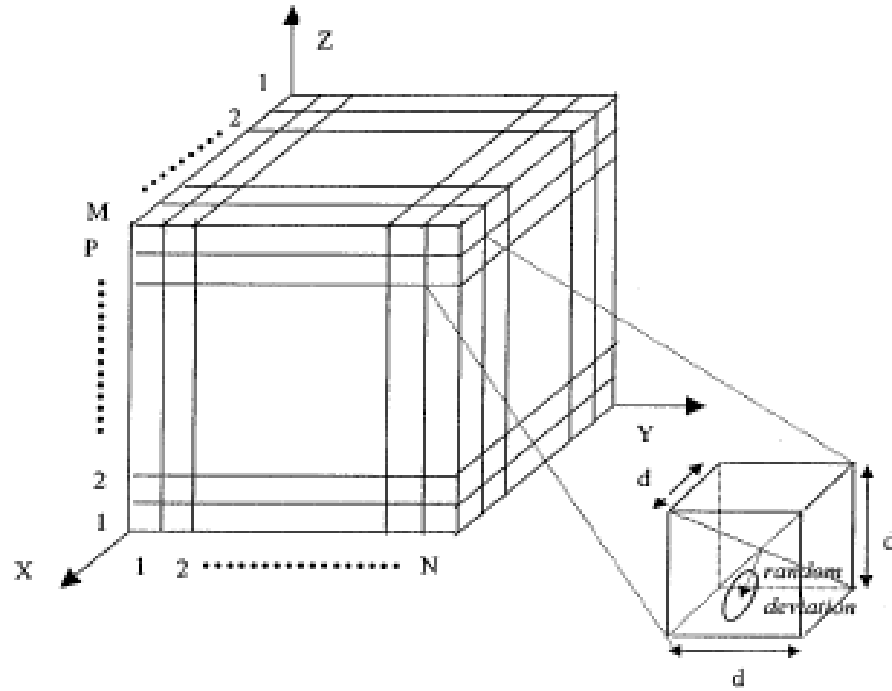


Figure 2.12 Unit volume of cells with the scatterers randomly placed from the centers of the cells

## 2.8 The limitation of currently existing scattering models

In real life, according to [24], leaves of deciduous vegetation are categorized as simple leaves (one main leaf on a stem) as shown in Figure 2.13 and compound leaves (more than one leaves on a stem). The compound leaves are further divided into two categories: palmately compound leaves as shown in Figure 2.16 and pinnately compound leaves. The pinnately compound leaves are composed as odd-pinnately compound leaves and even-pinnately compound leaves. The leaves of coniferous vegetation can be categorized as needles growing in clusters as shown in Figure 2.17 and needles growing singly as shown in Figure 2.18.

For the vegetation with compound leaves and needles growing in clusters, it is generally not valid to assume independent scattering by each single leaf or needle, since the coherence

effect among leaves within a compound or a cluster can be significant. The model of an electrically dense vegetation medium does account for coherence effect in leaves but it does not account for the specific pattern of a compound leaf or a specific cluster of needles. Hence, it is necessary to develop new vegetation scattering model to include these collective coherence effect.



Figure 2.13 A simple leaf

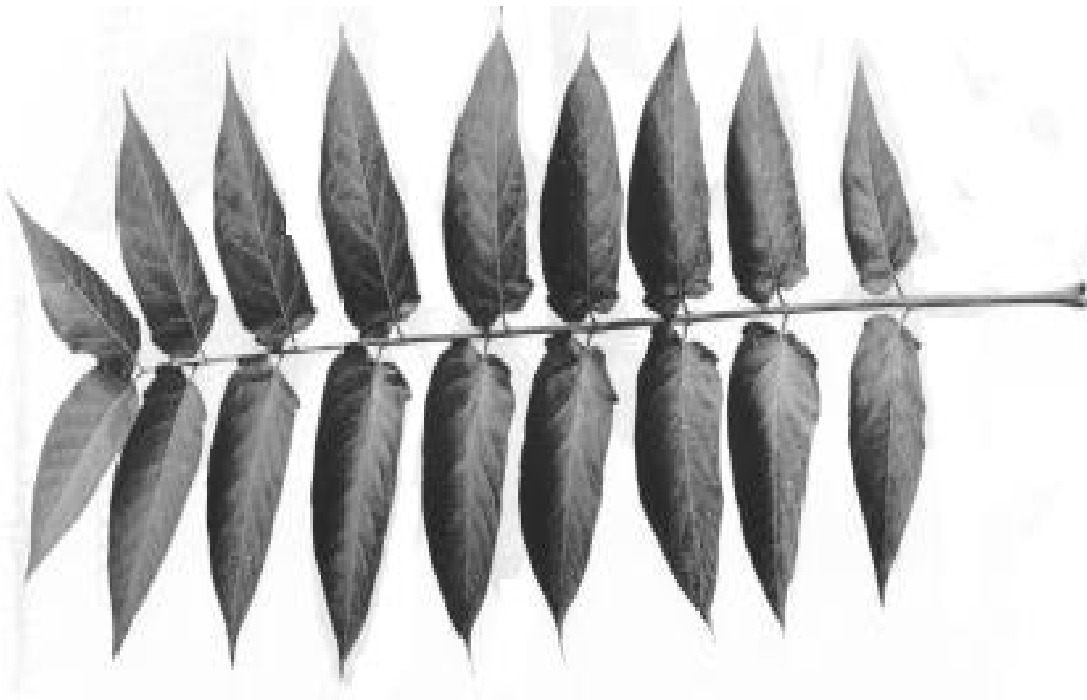


Figure 2.14 Even-pinnately compound leaves



Figure 2.15 Odd-pinnately compound leaves



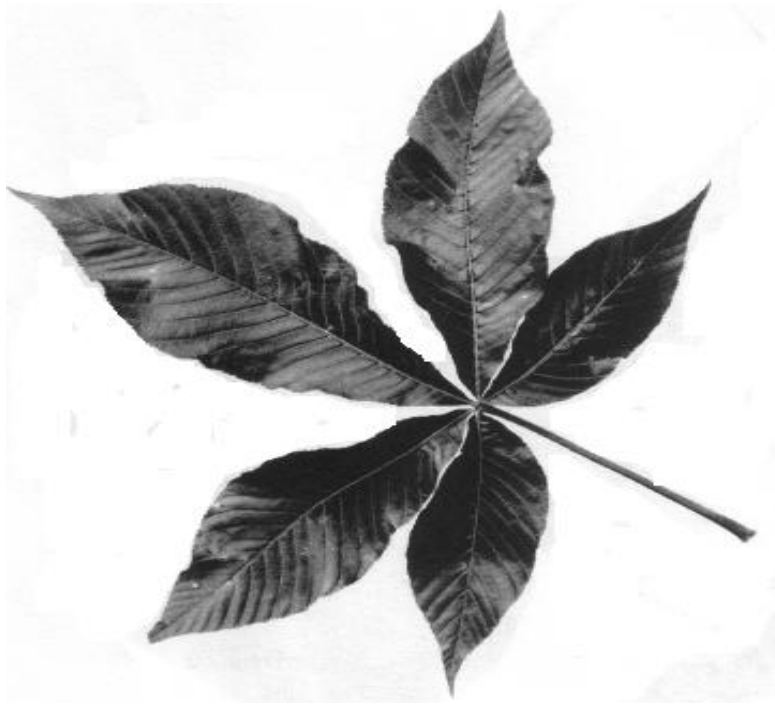


Figure 2.16 Palmately compound leaves



Figure 2.17 Needles Growing in Cluster



Figure 2.18 Needles Growing Singly

# **CHAPTER 3**

## **MICROWAVE MODELING OF VEGETATION COMPONENTS**

### **3.1 Introduction**

It is well known that vegetation cover is an important part of our environment and it has a definite impact on the life of all living beings. In order to monitor it, it is necessary to study its scattering mechanism. The common components of a vegetation are leaf, stems, branch, and trunk. The scattering from a vegetated area may consist of contributions from one or more of its components. In this chapter, we will study the scattering behavior of the model of each component. A formulation of the scattering problem will be presented first. Then, the corresponding scattering patterns of the components will be computed and illustrated. Finally, the relationship between the orientation distribution of each component and the corresponding scattering behavior will be discussed. For a simple deciduous leaf, we will model it with a circular disk. For a coniferous leaf, we shall use a needle to model it. For a compound leaf or a cluster of needles, we shall consider coherent scattering from an array of circular disks or a cone of needles. The branch or trunk of a tree is modeled by a finite-length dielectric cylinder. A size and an orientation distribution may have to be assigned depending on the tree species. For many practical applications, tree trunks may be assumed to be nearly vertical in orientation.

## 3.2 Leaf Shape

### 3.2.1 Formulation

The leaf shape of the deciduous vegetation can be circular or elliptic. The study in [26] has shown that the shape of an individual leaf does not have a significant effect on the overall scattering from a volume of randomly oriented leaves. Hence, we model the leaves of deciduous vegetations by identical circular dielectric discs [25,26]. Each disc has semi-axes  $(a_1 = a_2 \gg a_3)$  aligned through the local-frame axis  $x_i$  as shown Figure 3.1. The scattered field of each disc in the far zone can be written in terms of the Helmholtz integral as [27]

$$\bar{E}_s = \frac{e^{-jkr}}{r} \cdot \frac{k^2}{4\pi} (\bar{I} - \hat{s}\hat{s}) \iiint (\epsilon_r - 1) \cdot \bar{E}_{in}(r') e^{jk(\hat{s} \cdot \bar{r}')} d\bar{r}' \quad (3.1)$$

where  $\bar{I}$  is the unit dyad,  $k$  is the wave number in air,  $\epsilon_r$  is the relative dielectric constant of the leaf to air,  $\hat{s}$  is the scattering direction,  $r$  is the distance from the observation point to the leaf in the reference frame and  $\bar{E}_{in}(r')$  is the field inside the leaf, where  $r'$  is distance from the origin to the leaf.

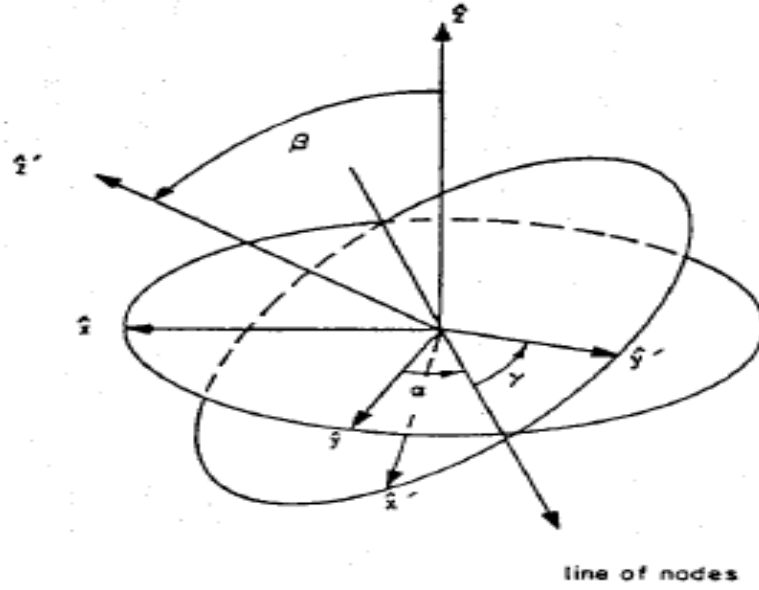


Figure 3.1 The geometry of a Circular or Elliptic Disk

The integration in (3.1) is over the volume of the scatterer (leaf) defined in terms of the prime variables.

Consider a plane wave impinging upon a circular disc located in the origin shown in Figure 3.1. Let the plane wave be [6][27].

$$\bar{E}_i = \hat{q}_i E_0 e^{-jk\hat{i} \cdot \bar{r}}, \quad q = v, h \quad (3.2)$$

where  $E_0$  is the amplitude of the incident field;  $\hat{i}(\theta_i, \phi_i)$  is the incident direction;

$\hat{q} = \hat{v}_i$  or  $\hat{h}_i$  is the unit polarization vector associated with the incident field. These vectors can be expressed in terms of the incident angles  $(\theta_i, \phi_i)$  and unit coordinate vectors as [6][27]

$$\hat{i} = \sin\theta_i(\hat{x}\sin\phi_i + \hat{y}\cos\phi_i) - \hat{z}\cos\theta_i \quad (3.3)$$

$$\hat{h}_i = \hat{y}\cos\phi_i - \hat{x}\sin\phi_i \quad (3.4)$$

$$\hat{v}_i = -\cos\theta_i(\hat{x}\cos\phi_i + \hat{y}\sin\phi_i) - \hat{z}\sin\theta_i \quad (3.5)$$

Similar expressions exist for the scattering direction and associated unit polarization vectors in terms of the scattering angles  $(\theta_s, \phi_s)$  as follows.

$$\hat{s} = \sin\theta_s(\hat{x}\sin\phi_s + \hat{y}\cos\phi_s) - \hat{z}\cos\theta_s \quad (3.6)$$

$$\hat{h}_s = \hat{y}\cos\phi_s - \hat{x}\sin\phi_s \quad (3.7)$$

$$\hat{v}_s = -\cos\theta_s(\hat{x}\cos\phi_s + \hat{y}\sin\phi_s) - \hat{z}\sin\theta_s \quad (3.8)$$

The field  $\bar{E}_{in}(r')$  inside the leaf is approximated by using the generalized Rayleigh-Gans (GRG) approach as [28]

$$\begin{aligned} \bar{E}_{in}(r') &= \bar{\bar{\alpha}} \cdot \bar{E}_i e^{-jk\hat{i} \cdot \bar{r}'} \\ &= \bar{\bar{\alpha}} \cdot \hat{q}_i E_0 e^{-jk\hat{i} \cdot \bar{r}} \end{aligned} \quad (3.9)$$

where  $\bar{\bar{\alpha}}$  represents the polarizability tensor and it can be expressed in terms of two demagnetizing factors  $\alpha_T$  and  $\alpha_N$  as [26]

$$\bar{\bar{\alpha}} = \alpha_T \bar{\bar{I}} + (\alpha_N - \alpha_T) \hat{z}\hat{z} \quad (3.10)$$

where  $\bar{\bar{I}}$  is the identity matrix and

$$\alpha_T = \frac{1}{(\epsilon_r - 1)g_T + 1} \quad (3.11)$$

$$\alpha_N = \frac{1}{(\epsilon_r - 1)g_N + 1} \quad (3.12)$$

where  $g_T$  and  $g_N$  are the demagnetizing factors given as [30]

$$g_T = \frac{1}{2(m^2 - 1)} \cdot \left[ \frac{m^2}{\sqrt{m^2 - 1}} \operatorname{asin} \left( \frac{\sqrt{m^2 - 1}}{m} \right) - 1 \right] \quad (3.13)$$

$$g_N = \frac{m^2}{m^2 - 1} \left[ 1 - \frac{1}{\sqrt{m^2 - 1}} \operatorname{asin} \left( \frac{\sqrt{m^2 - 1}}{m} \right) \right] \quad (3.14)$$

$$\text{where } m = \frac{a_1}{a_3}.$$

Substituting the inner field of a disc (3.2) into (3.1), the far-zone scattered field of a disc can be expressed as

$$\bar{E}_s(\hat{s}, \hat{i}) = \bar{\bar{F}}(\hat{s}, \hat{i}) \cdot \hat{q}' E_0 \frac{e^{-jkr}}{r} \quad (3.15)$$

where  $\hat{q}' = \hat{v}'_i$  or  $\hat{h}'_i$  is the polarization unit vector in the local frame written as

$$\hat{h}'_i = \hat{y}' \cos \phi'_i - \hat{x}' \sin \phi'_i \quad (3.16)$$

$$\hat{v}'_i = -\cos \theta'_i (\hat{x}' \cos \phi'_i + \hat{y}' \sin \phi'_i) - \hat{z}' \sin \theta'_i \quad (3.17)$$

and  $\theta'_i, \phi'_i$  are the local incidence-angle pair related to the incidence-angle pair  $(\theta_i, \phi_i)$  in the reference frame as

$$\cos \theta'_i = \cos \beta \cos \theta_i - \sin \beta \cos(\alpha - \phi_i) \sin \theta_i \quad (3.18)$$

$$\cos \phi'_i = -\hat{i} \cdot \hat{z}'$$

$$= \frac{\sin\theta_i[\cos\gamma\cos\beta\cos(\alpha-\phi_i) - \sin\gamma\sin(\alpha-\phi_i)] + \cos\theta_i\cos\gamma\sin\beta}{\sqrt{1 - (\sin\beta\sin\theta_i\cos(\alpha-\phi_i) - \cos\beta\cos\theta_i)^2}} \quad (3.19)$$

where  $\alpha, \beta, \gamma$  are the leaf-orientation angles in the reference frame. For two dimensional objects such as a disk, we expect only two angle,  $\alpha, \beta$ , are needed to define its orientation.

In the local-frame, the scattering tensor  $\bar{\bar{F}}(\hat{s}, \hat{i})$  is given by

$$\bar{\bar{F}}(\hat{s}, \hat{i}) = \frac{k^2(\epsilon_r - 1)v_0}{4\pi}(\bar{\bar{I}} - \hat{s}\hat{s}) \cdot \bar{\bar{a}} \cdot (\bar{\bar{I}} - \hat{i}\hat{i})\mu(\hat{s}, \hat{i}) \quad (3.20)$$

where  $v_0 = (4\pi/3)a_1a_2a_3$  is the disc volume and the Debye interference function  $\mu(\hat{s}, \hat{i})$  is defined as [31]

$$\mu(s, i) = \frac{1}{v_0} \iiint e^{-jk(\hat{i} - \hat{s}) \cdot \vec{r}} d\vec{r} \quad (3.21)$$

The explicit form of the scattering amplitude tensor elements in the local frame can be obtained by substituting (3.16), (3.17) and (3.3) into (3.20) yielding

$$F_{vv}(\hat{s}, \hat{i}) = -\frac{k^2 v_0}{4\pi}(\epsilon_r - 1) \quad (3.22)$$

$$[a_N \sin\theta'_i \sin\theta'_s - a_T \cos\theta'_i \cos\theta'_s \cos(\phi'_s - \phi'_i)]\mu(\hat{s}, \hat{i})$$

$$F_{hv}(\hat{s}, \hat{i}) = \frac{k^2(\epsilon_r - 1)}{4\pi}v_0 \cos\theta'_i \sin(\phi'_s - \phi'_i) \cdot a_T \mu(\hat{s}, \hat{i}) \quad (3.23)$$

$$F_{vh}(\hat{s}, \hat{i}) = \frac{k^2(\epsilon_r - 1)}{4\pi}v_0 \cos\theta'_s \sin(\phi'_s - \phi'_i) \cdot a_T \mu(\hat{s}, \hat{i}) \quad (3.24)$$

$$F_{hh}(\hat{s}, \hat{i}) = \frac{k^2(\epsilon_r - 1)}{4\pi}v_0 \cos(\phi'_s - \phi'_i) a_T \mu(\hat{s}, \hat{i}) \quad (3.25)$$

where  $(\theta'_s, \phi'_s)$  is the scattering angles in the local frame.



The scattering amplitude in the reference frame  $F_{pq}(\hat{s}, \hat{i})$  is given by

$$F_{pq}(\hat{s}, \hat{i}) = \hat{p} \cdot \bar{\bar{F}}(\hat{s}, \hat{i}) \cdot \hat{q} \quad (3.26)$$

where  $\hat{p} = \hat{v}_s$  or  $\hat{h}_s$  are the polarization unit vectors in the reference frame.

The explicit forms of  $F_{pq}(\hat{s}, \hat{i})$  for horizontal and vertical polarizations are given as

$$F_{vv}(\hat{s}, \hat{i}) = \frac{1}{D(\hat{s}, \hat{i})} \quad (3.27)$$

$$\{t_{vs}[F_{vv}(\hat{s}, \hat{i})t_{vi} - F_{vh}(\hat{s}, \hat{i})t_{hi}] - t_{hs}[F_{hv}(\hat{s}, \hat{i})t_{vi} - F_{hh}(\hat{s}, \hat{i})t_{hi}]\}$$

$$F_{hv}(\hat{s}, \hat{i}) = \frac{1}{D(\hat{s}, \hat{i})} \quad (3.28)$$

$$\{t_{hs}[F_{vv}(\hat{s}, \hat{i})t_{vi} - F_{vh}(\hat{s}, \hat{i})t_{hi}] + t_{vs}[F_{hv}(\hat{s}, \hat{i})t_{vi} - F_{hh}(\hat{s}, \hat{i})t_{hi}]\}$$

$$F_{vh}(\hat{s}, \hat{i}) = \frac{1}{D(\hat{s}, \hat{i})} \quad (3.29)$$

$$\{t_{vs}[F_{vv}(\hat{s}, \hat{i})t_{hi} + F_{vh}(\hat{s}, \hat{i})t_{vi}] - t_{hs}[F_{hv}(\hat{s}, \hat{i})t_{hi} + F_{hh}(\hat{s}, \hat{i})t_{vi}]\}$$

$$F_{hh}(\hat{s}, \hat{i}) = \frac{1}{D(\hat{s}, \hat{i})} \quad (3.30)$$

$$\{t_{hs}[F_{vv}(\hat{s}, \hat{i})t_{hi} + F_{vh}(\hat{s}, \hat{i})t_{vi}] + t_{vs}[F_{hv}(\hat{s}, \hat{i})t_{hi} + F_{hh}(\hat{s}, \hat{i})t_{vi}]\}$$

where

$$D(s, i) = \sqrt{(t_{vs}^2 + t_{hs}^2)(t_{vi}^2 + t_{hi}^2)} \quad (3.31)$$

$$t_{vi} = -[\sin\beta \cos\theta_i \cos((\alpha - \phi_i) + \cos\beta \sin\theta_i)] \quad (3.32)$$

$$t_{hi} = \sin\beta \sin(\alpha - \phi_i) \quad (3.33)$$

$$t_{vs} = -[\sin\beta \cos\theta_s \cos((\alpha - \phi_s) + \cos\beta \sin\theta_s)] \quad (3.34)$$

$$t_{hs} = \sin\beta \sin(\alpha - \phi_s) \quad (3.35)$$

We can write the backscattering coefficient from the vegetated half-space as follows [34] by using the first-order solution of the radiative transfer equations

$$\sigma_{pq}(\hat{-i}, \hat{i}) = 4\pi \cos \theta_i \frac{\langle |F_{pq}(\hat{-i}, \hat{i})|^2 \rangle}{\langle \sigma_p(\hat{-i}) \rangle + \langle \sigma_q(\hat{i}) \rangle} \quad (3.36)$$

In the above equation, the ensemble average  $\langle \rangle$  is taken over the leaf orientation as

$$\langle |F_{pq}(\hat{-i}, \hat{i})|^2 \rangle = \int d\alpha \int d\beta p(\alpha) p(\beta) |F_{pq}(\hat{-i}, \hat{i})|^2 \quad (3.37)$$

where  $p(\alpha), p(\beta)$  are the probability distribution functions of the leaf orientations.

The extinction cross section  $\sigma_p(\hat{i})$  is obtained by the sum of the scattering cross section,  $\sigma_{sp}(\hat{i})$ , and the Ohmic cross section,  $\sigma_{ap}(\hat{i})$ .

$$\sigma_{sp}(\hat{i}) = \int_0^\pi \sin \theta_s d\theta_s \int_0^{2\pi} d\phi_s [ |F_{vp}(\hat{s}, \hat{i})|^2 + |F_{hp}(\hat{s}, \hat{i})|^2 ] \quad (3.38)$$

$$\sigma_{ap}(\hat{i}) = \frac{4\pi}{k} \text{Im}[F_{pp}(\hat{i}, \hat{i})] \quad (3.39)$$

### 3.2.2 Scattering Pattern

In this section, the scattering pattern of the circular disc over the incidence angle is illustrated for three different values, 4cm, 6cm, and 8cm, of the radius

The VV polarization scattering pattern is shown in Figure 3.2. Generally, the scattering amplitude is oscillatory and decreasing with an increase in the incidence angle from  $0^\circ$  to  $90^\circ$ . As expected the trend of the scattering amplitude over the incident angular range,  $90^\circ$  and  $180^\circ$ , is the mirror image of that over  $0^\circ$  and  $90^\circ$ . As the disc's

radius increases, the number of oscillations increases, and so does the amplitude of the scattering pattern.

The HH polarization scattering patterns are illustrated in Figure 3.3. The general trend behaviors in size and angle are similar to those of the VV polarization, except that the total range of variations is smaller. In Figure 3.4 we show similar calculations for the VH polarization. Here again, the general trend behaviors of the scattering patterns are similar to those of the VV polarization but both the range of variation and its absolute level are much smaller.

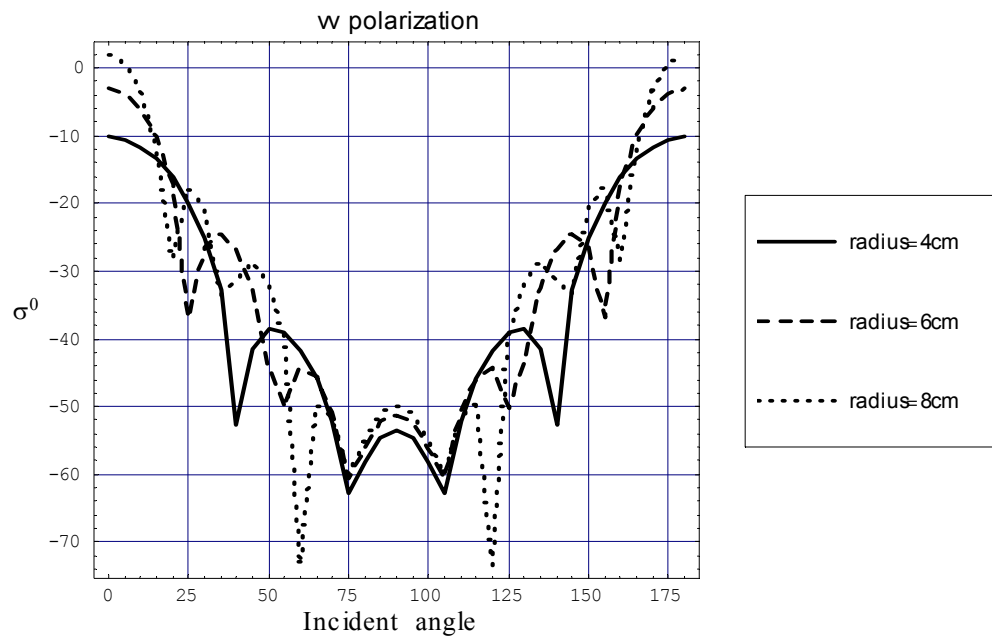


Figure 3.2 VV Scattering Pattern of a circular disc versus the incidence angle

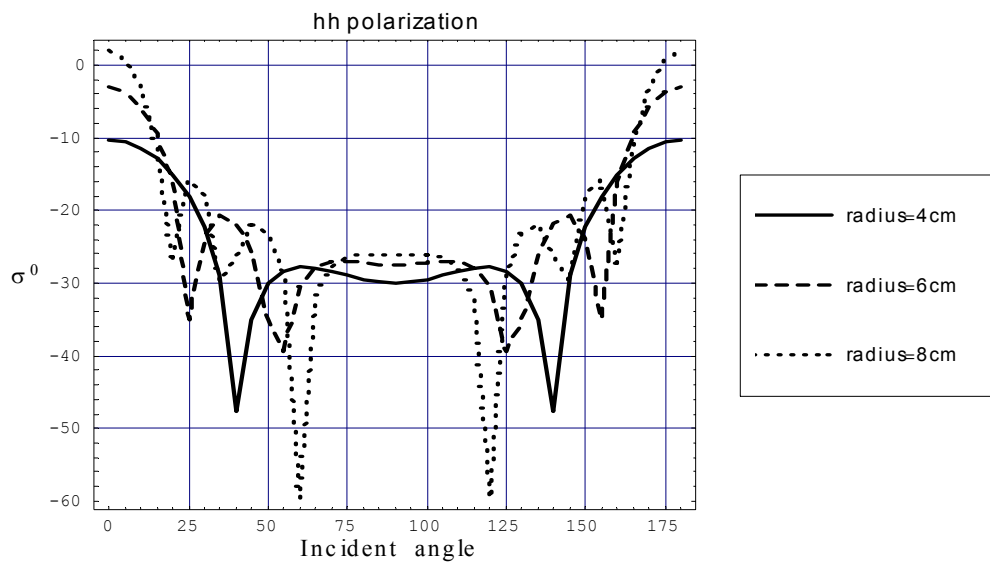


Figure 3.3 HH Scattering Pattern of a circular disc versus the incidence angle

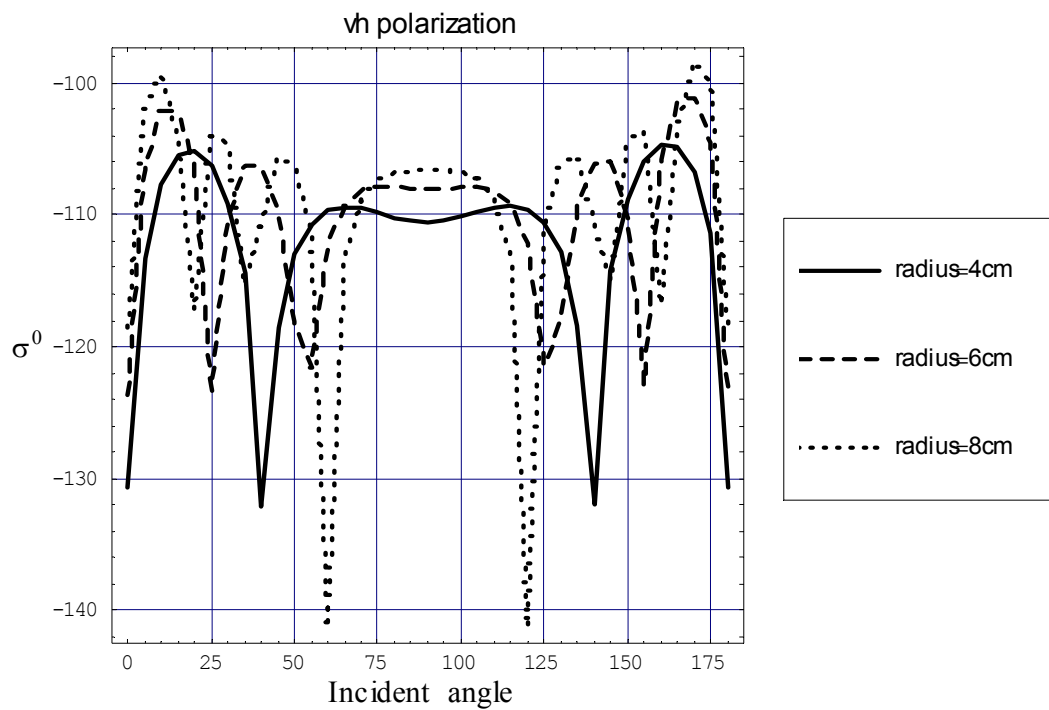


Figure 3.4 VH Scattering Pattern of a circular disc versus the incidence angle

### 3.2.3 Orientation Distribution Effects

In the previous section, we have demonstrated the behavior of the scattering pattern of a circular disc versus the incidence angle for three different sizes of the radius. In this section, based on the results of the previous section, we will study the effects of the orientation distribution. The variation of VV and VH backscattering coefficients for a half-space of circular leaves as a function of the incidence angle for different distributions of the tilt angle  $\beta$  with  $0^\circ < \beta < 90^\circ$ ,  $0^\circ < \beta < 60^\circ$ ,  $0^\circ < \beta < 45^\circ$  and  $0^\circ < \beta < 30^\circ$  are displayed in Figure 3.5 and Figure 3.6 respectively. Comparing with the behaviors of the scattering pattern of a circular disc shown in the previous section, the trend of the backscattering coefficient resulted from averaging the scattering pattern over the tilt angle  $\beta$  is to decrease smoothly with the incidence angle. Most of the oscillations have been averaged out. The VV and VH polarization behaviors with respect to different distributions of the azimuth angle  $\alpha$  are illustrated in Figure 3.7 and Figure 3.8. Different ranges for  $\alpha$  are indicated on the figures. As expected, the distributions of  $\alpha$  do have impact on the behavior of the backscattering coefficient and the magnitude of backscattering coefficient become strong around the range of azimuth direction where circular disks distributed and weak around the range of azimuth direction where circular disks do not exist.

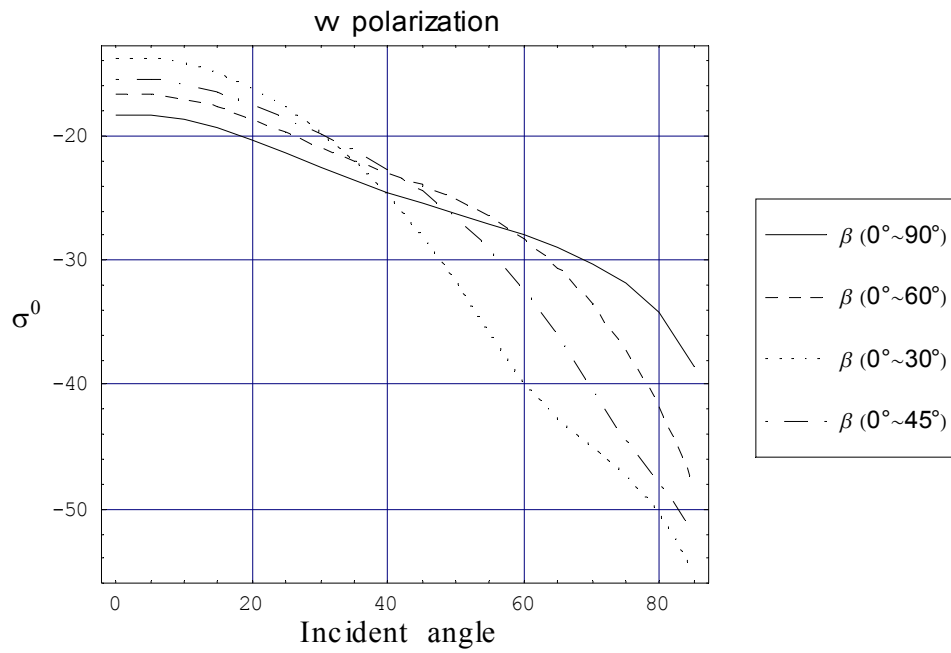


Figure 3.5 VV backscattering coefficient versus the incidence angle with different distribution of the tilt angle  $\beta$  at  $0^\circ < \alpha < 360^\circ$

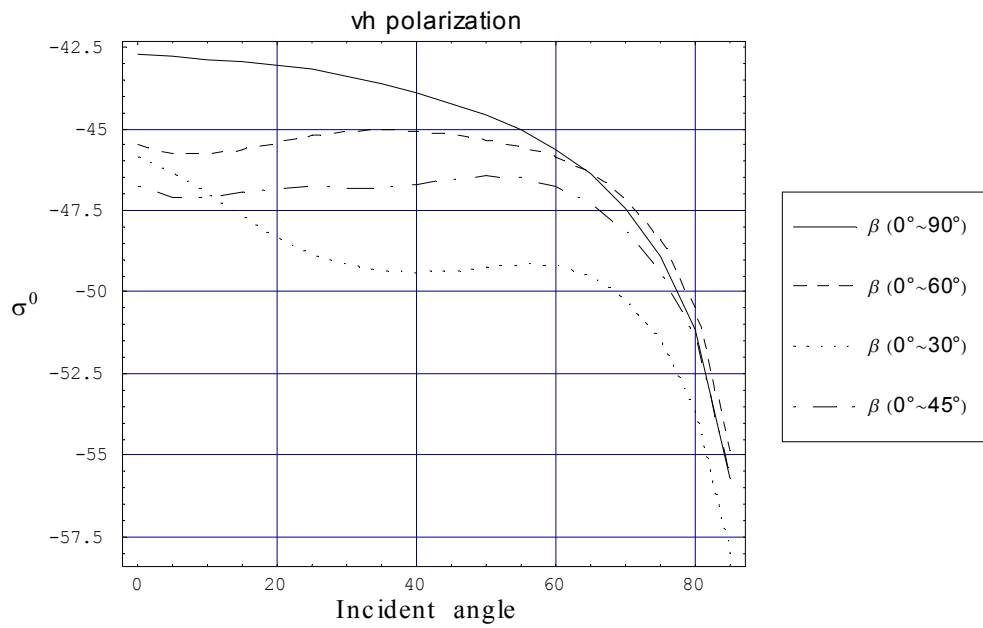


Figure 3.6 VH backscattering coefficient versus the incidence angle with different distribution of the tilt angle  $\beta$  at  $0^\circ < \alpha < 360^\circ$

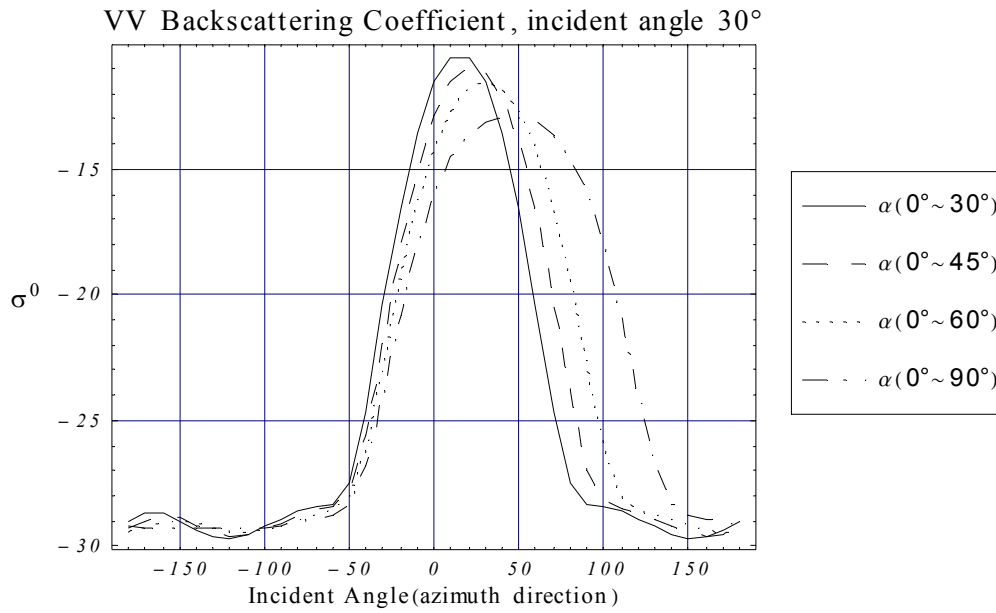


Figure 3.7 VV backscattering coefficient versus the incidence angle (azimuth direction) with different distribution of the azimuth angle  $\alpha$  at  $0^\circ < \beta < 90^\circ$ .

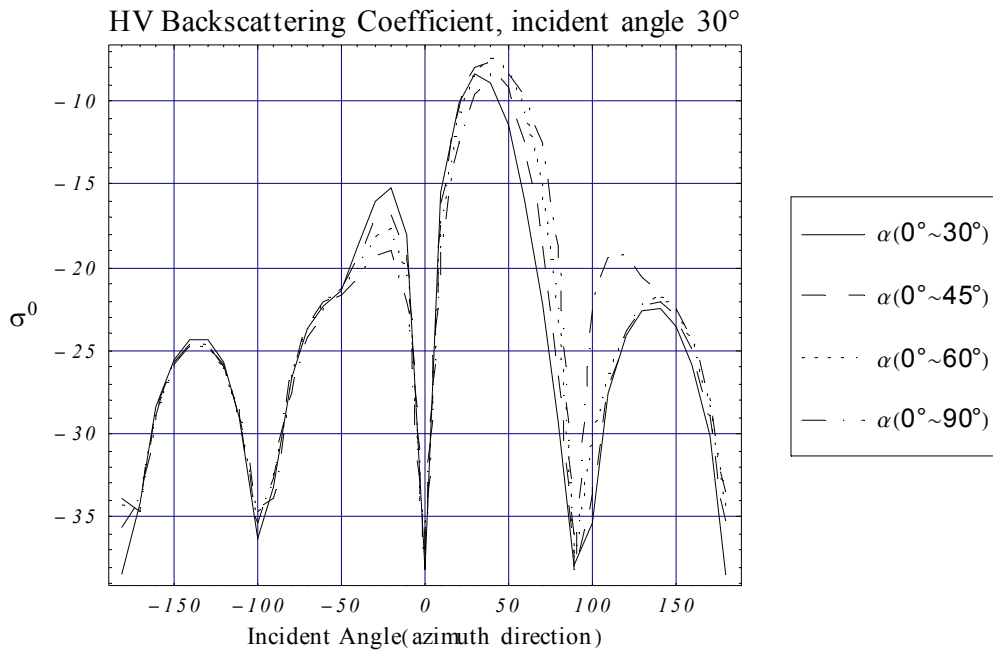


Figure 3.8 HV backscattering coefficient versus the incidence angle (azimuth direction) with different distribution of the azimuth angle  $\alpha$  at  $0^\circ < \beta < 90^\circ$

### 3.3 Needle

#### 3.3.1 Formulation

The leaves of coniferous vegetations are modelled as randomly oriented needles. Each needle is modelled as an ellipsoid with radius  $a$  and length  $L$  with  $a \ll L$  as shown in Figure 3.9.

Following a similar procedure as shown in the previous section, the scattering amplitude tensor of the needle can be written as [27]

$$F_{pq}(\hat{s}, \hat{i}) = \frac{k^2 v_0}{4\pi} (\epsilon_r - 1) [a_T(\hat{p}_s \cdot \hat{q}_i) + (\hat{p}_s \cdot \hat{z})(\hat{z} \cdot \hat{q}_i)(a_N - a_T)] \mu(\hat{s}, \hat{i}) \quad (3.40)$$

where  $\hat{i}$ ,  $\hat{s}$  are the incident and scattering directions and  $\hat{p}_i$ ,  $\hat{q}_s$  are the polarization unit vectors defined as follows,

$$\begin{aligned} \hat{i} &= \sin \theta_i (\hat{x} \cos \phi_i + \hat{y} \sin \phi_i) - \hat{z} \cos \theta_i \\ \hat{h}_i &= \hat{y} \cos \phi_i - \hat{x} \sin \phi_i \\ \hat{v}_i &= -\cos \theta_i (\hat{x} \cos \phi_i + \hat{y} \sin \phi_i) - \hat{z} \sin \theta_i \end{aligned} \quad (3.41)$$

and

$$\begin{aligned} \hat{s} &= \sin \theta_s (\hat{x} \cos \phi_s + \hat{y} \sin \phi_s) - \hat{z} \cos \theta_s \\ \hat{h}_s &= \hat{y} \cos \phi_s - \hat{x} \sin \phi_s \\ \hat{v}_s &= -\cos \theta_s (\hat{x} \cos \phi_s + \hat{y} \sin \phi_s) - \hat{z} \sin \theta_s \end{aligned} \quad (3.42)$$



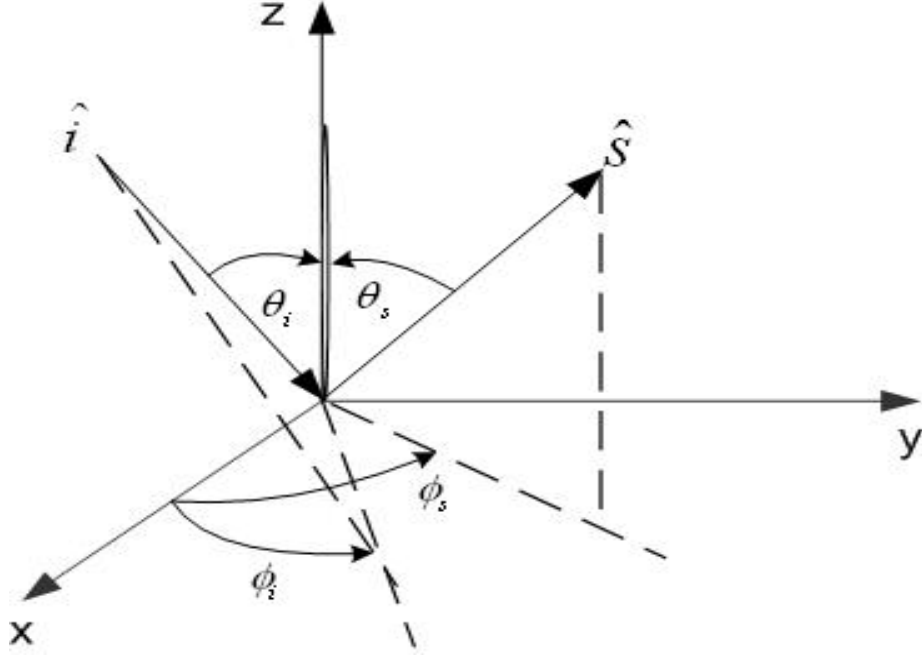


Figure 3.9 Geometry of the needle problem

The explicit form of the scattering amplitude tensor of the needle can be found by calculating the vector dot products in (3.40) using (3.41) and (3.42) as

$$F_{vv}(\hat{s}, \hat{i}) = \frac{k^2(\epsilon_r - 1)v_0}{4\pi} \quad (3.43)$$

$$[a_N \sin \theta_i \sin \theta_s - a_T \cos \theta_i \cos \theta_s \cos(\phi_s - \phi_i)] \mu(\hat{s}, \hat{i})$$

$$F_{vh}(\hat{s}, \hat{i}) = \frac{k^2(\epsilon_r - 1)v_0}{4\pi} \cos \theta_s \sin(\phi_s - \phi_i) a_T \mu(\hat{s}, \hat{i})$$

$$F_{hv}(\hat{s}, \hat{i}) = \frac{k^2(\epsilon_r - 1)v_0}{4\pi} \cos \theta_i \sin(\phi_s - \phi_i) a_T \mu(\hat{s}, \hat{i})$$

$$F_{hh}(\hat{s}, \hat{i}) = \frac{k^2(\epsilon_r - 1)v_0}{4\pi} \cos(\phi_s - \phi_i) a_T \mu(\hat{s}, \hat{i})$$

where  $a_N, a_T$  are defined by the demagnetizing factors  $g_T, g_N$  as

$$\begin{aligned}
a_T &= \frac{1}{(\varepsilon_r - 1)g_T + 1} \\
a_N &= \frac{1}{(\varepsilon_r - 1)g_N + 1}
\end{aligned} \tag{3.44}$$

For the needle  $(a, L)$ , the demagnetizing factors can be expressed as [27] [30]

$$\begin{aligned}
g_T &= \frac{b(b^2 - 1)}{2} \left[ \frac{b}{b^2 - 1} + \frac{1}{2} \log \left( \frac{b-1}{b+1} \right) \right] \\
g_N &= -(b^2 - 1) \left[ \frac{1}{2} b \log \left( \frac{b-1}{b+1} \right) + 1 \right] \\
b &= \sqrt{1 - \left( \frac{2a}{L} \right)^2}
\end{aligned} \tag{3.45}$$

and the modifying function  $\mu(\hat{s}, \hat{i})$  in (3.40) and (3.43) can be approximated using the GRG approximation [32] as

$$\mu(s, i) = \frac{\sin[0.5kL(\cos\theta_i + \cos\theta_s)]}{0.5kL(\cos\theta_i + \cos\theta_s)} = \text{sinc}[0.5kL(\cos\theta_i + \cos\theta_s)] \tag{3.46}$$

### 3.3.2 Scattering Pattern

In this section, the radar cross section of the needle with radius of 0.17cm and a dielectric constant of 8.36-j3.12 is computed at 9.9GHz for different lengths of the needle.

In the figures 3.10, 3.11, and 3.12, VV, HH and VH scattering patterns are illustrated over incidence angle between  $0^\circ$  and  $180^\circ$  for four different lengths of the needle. The results are symmetric with respect to the angle,  $90^\circ$ . The amplitude of the scattering pattern is generally increasing with the incident angle increasing from  $0^\circ$  to  $90^\circ$  for VV and HH polarization. With length of the needle increasing, the number of oscillations increases while the average angular trend remains upward towards  $90^\circ$ . A similar oscillatory scattering behavior exists in

VH polarization as shown in Figure 3.12 except the general trend of the scattering pattern is not always increasing towards  $90^\circ$ .

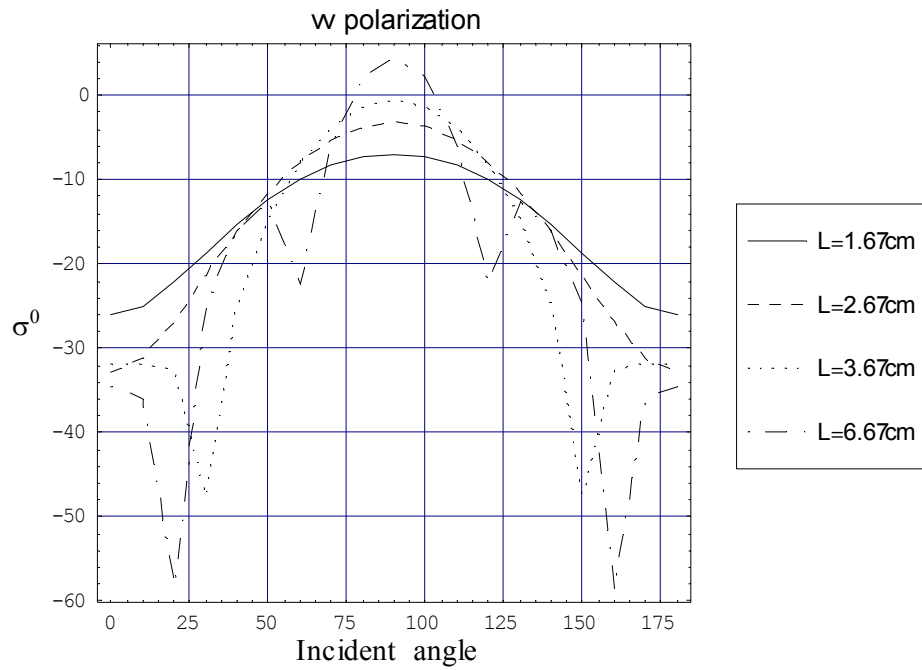


Figure 3.10 The VV scattering patterns versus the incidence angle for four different needle lengths.

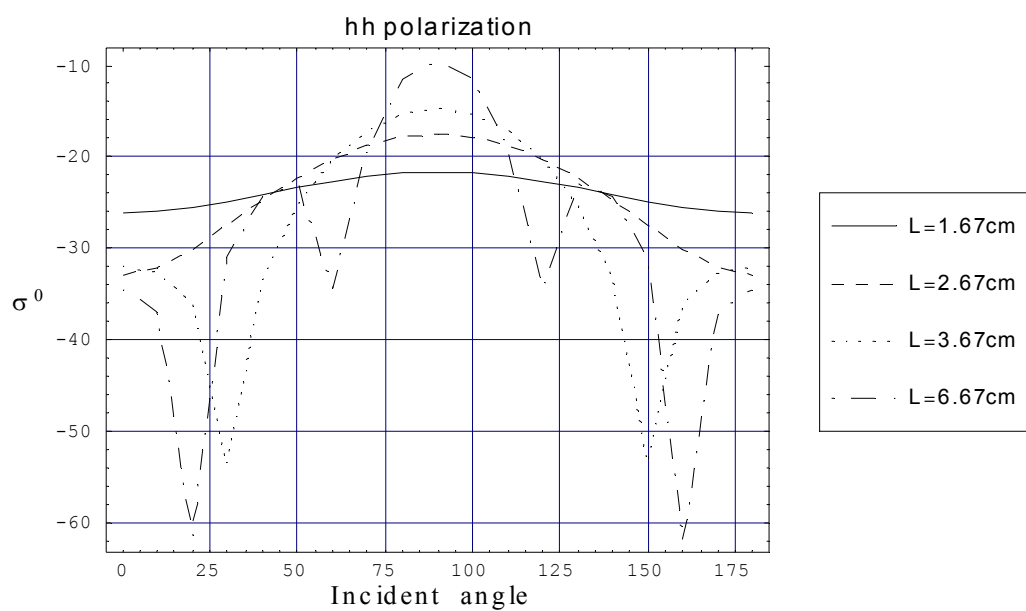


Figure 3.11 The HH scattering patterns versus the incidence angle for four different needle lengths.

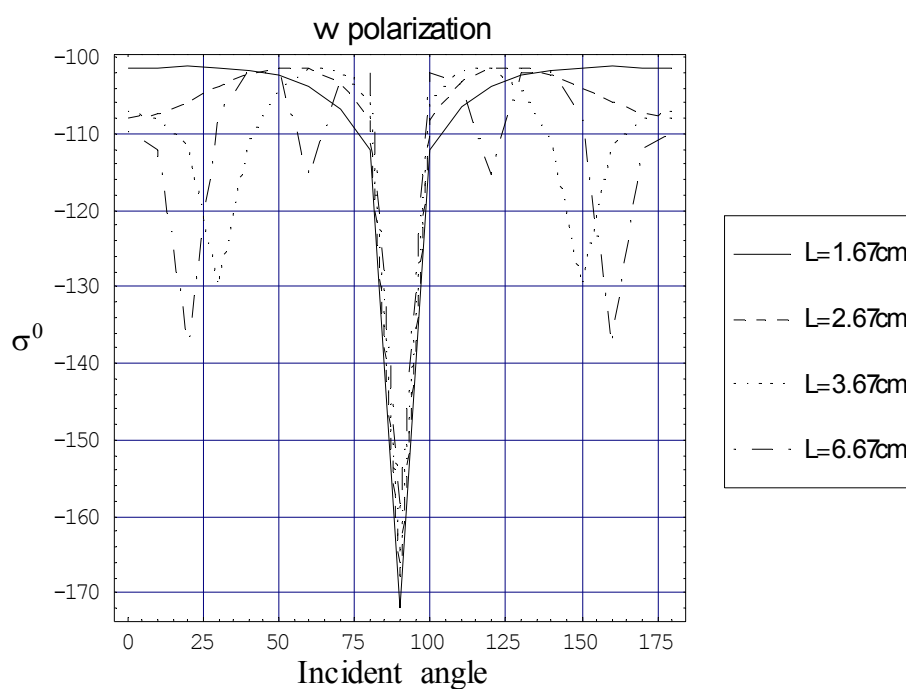


Figure 3.12 The VH scattering patterns versus the incidence angle for four different needle lengths.

### 3.3.3 Orientation Distribution Effects

In this section, we investigate the scattering properties of the needle with length 3.07cm, radius 0.17cm, and a dielectric constant  $8.36-j\ 3.12$  at 9.9 GHz, when the orientation distribution changes.

In figures 3.13, 3.14, and 3.15, the behaviors of VV, HH, and VH backscattering coefficients versus the incidence angle are shown for different distributions of the tilt angle indicated on these figures. The scattering properties of the near vertically oriented needles ( $0^\circ < \beta < 30^\circ$ ) are seen to be quite different from the near horizontally oriented needles ( $30^\circ < \beta < 90^\circ$ ), and randomly oriented needles ( $0^\circ < \beta < 90^\circ$ ) especially in the angular range,  $0 \leq \theta < 55^\circ$ . This is because near vertically oriented needles do not contribute appreciably near normal incidence and hence has a rising angular trend, whereas the other two distributions have a decreasing angular trend over the same angular region,  $0 \leq \theta < 55^\circ$ .

Next, we consider changing the distribution in the azimuth angle,  $\alpha$ . The backscattering characteristics of VV, HH and VH versus the incidence angle for the four distributions,  $0^\circ < \alpha < 90^\circ$ ,  $0^\circ < \alpha < 180^\circ$ ,  $0^\circ < \alpha < 270^\circ$  and  $0^\circ < \alpha < 360^\circ$  are plotted in figures, 3.16, 3.17 and 3.18 respectively. The illustrations show that the general angular trends of the backscattering coefficients for different distributions of the azimuth angle are similar except for some differences in amplitude.

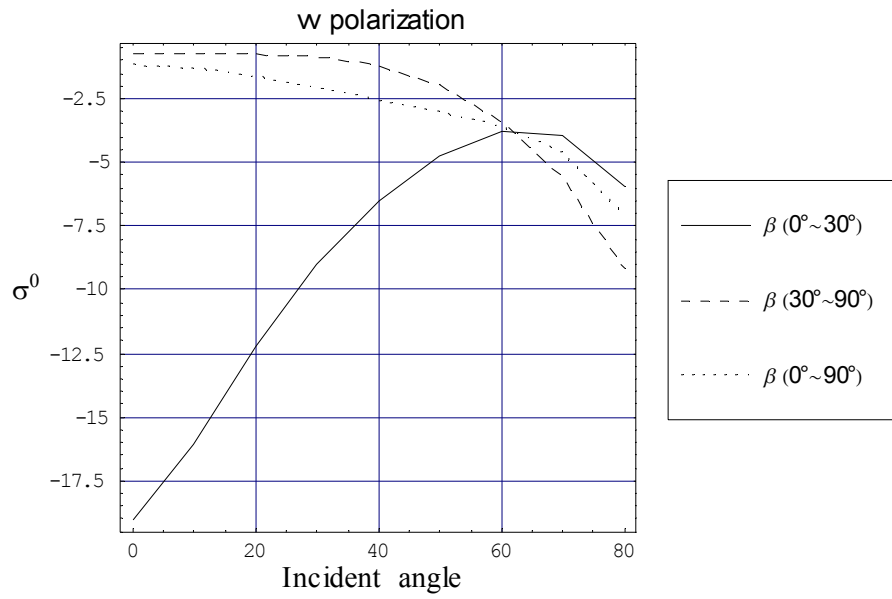


Figure 3.13 The VV backscattering coefficients versus the incidence angle for different distributions of the tilt angle  $\beta$ , when  $0^\circ < \alpha < 360^\circ$

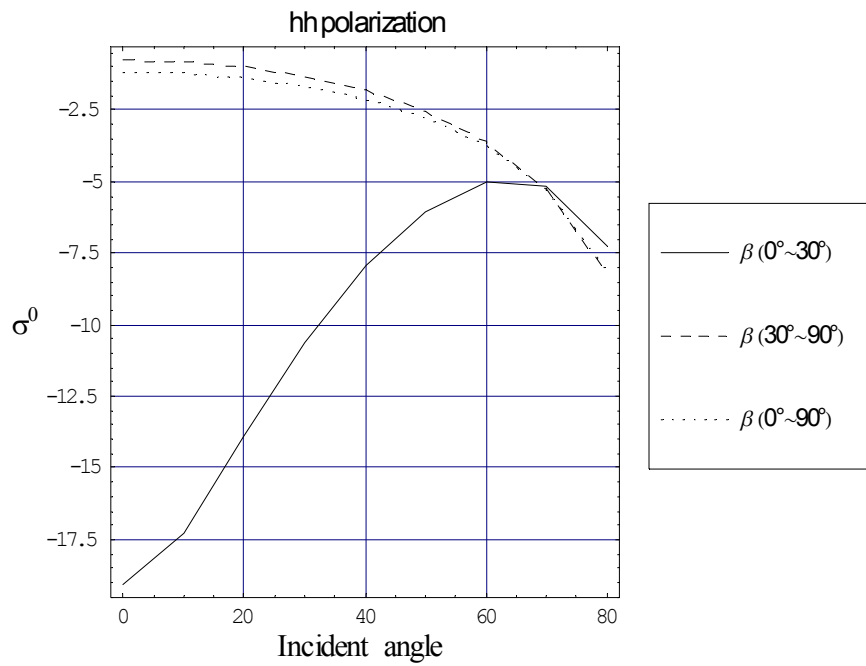


Figure 3.14 The HH backscattering coefficient versus the incidence angle for different distributions of the tilt angle  $\beta$ , when  $0^\circ < \alpha < 360^\circ$ .

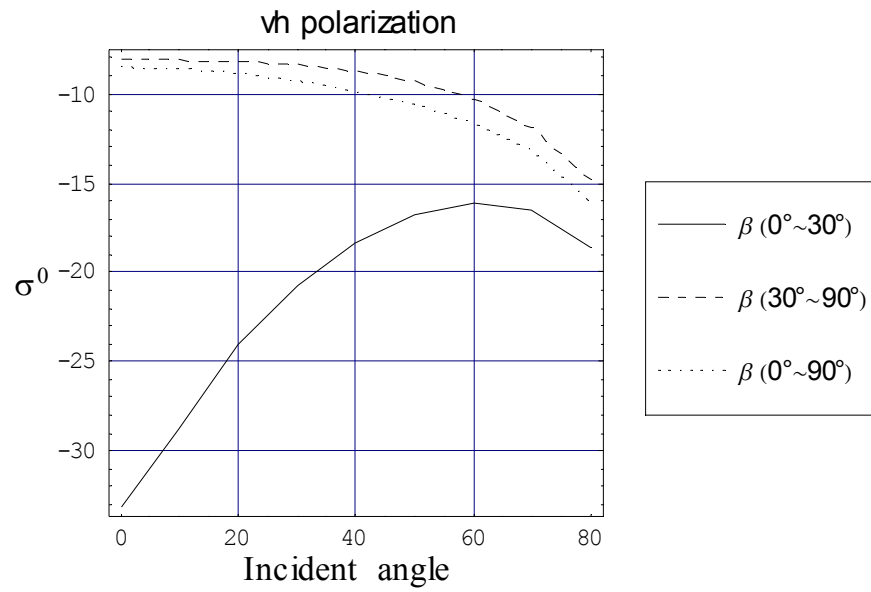


Figure 3.15 The VH backscattering coefficient versus the incidence angle for different distributions of the tilt angle  $\beta$ , when  $0^\circ < \alpha < 360^\circ$

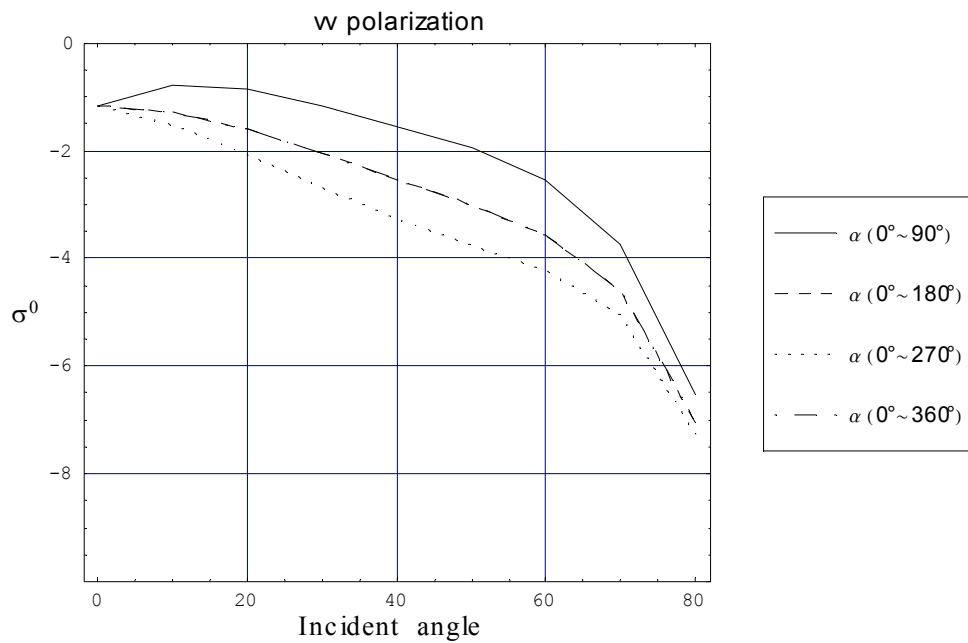


Figure 3.16 The VV backscattering coefficient versus the incidence angle for different distributions of the azimuth angle  $\alpha$ , when  $0^\circ < \beta < 90^\circ$

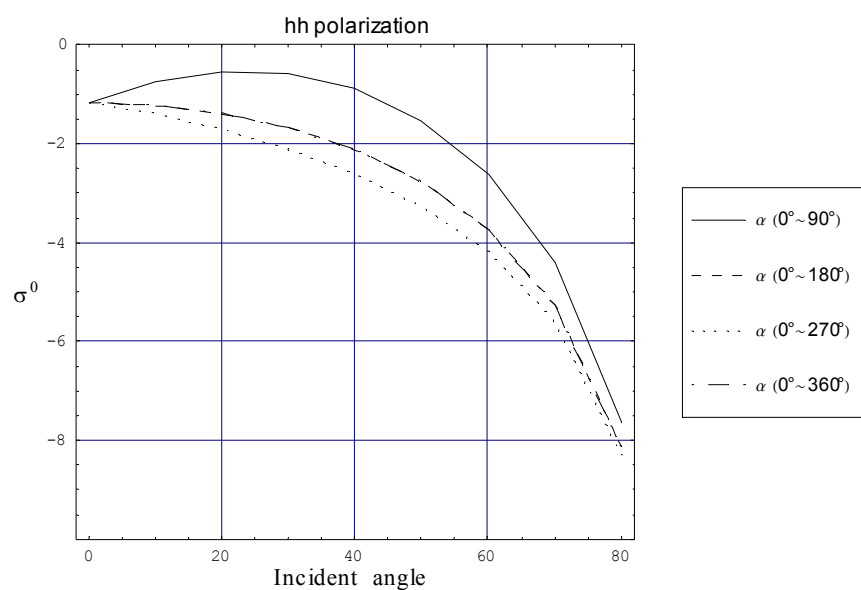


Figure 3.17 The HH backscattering coefficient versus the incidence angle for different distributions of the azimuth angle  $\alpha$ , when  $0^\circ < \beta < 90^\circ$ .

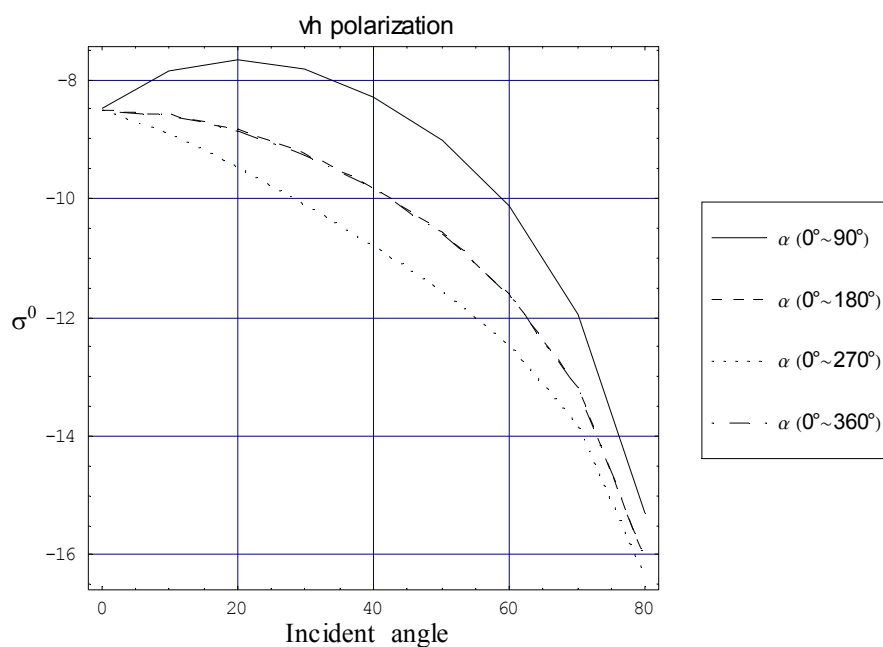


Figure 3.18 The VH backscattering coefficient versus the incidence angle for different distributions of the azimuth angle  $\alpha$ , when  $0^\circ < \beta < 90^\circ$ .



### 3.4 Pinnately compound leaf pattern

A pinnately compound leaf is shown in Figure 3.19. Due to the specific arrangement of the individual leaves needed to form this compound leaf, for this type of vegetation, the individual leaf will not scatter independently. Thus, it is necessary to treat the compound leaf as one scatterer and we need to compute the coherent sum of the scattered fields from each individual component of this compound leaf.

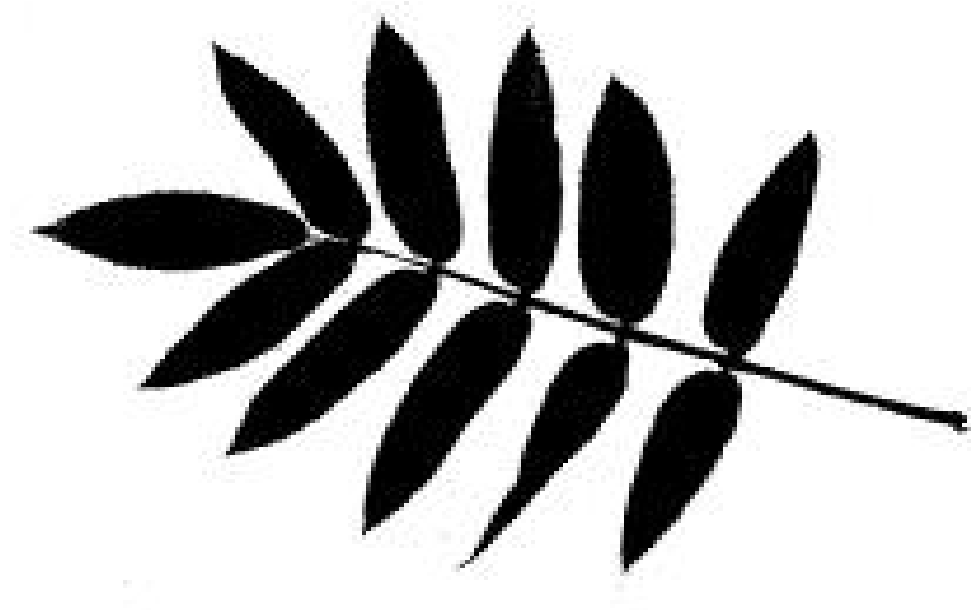


Figure 3.19 A Pinnately compound leaf

#### 3.4.1 Formulation

For the deciduous vegetation with a compound-leaf pattern such as the one in Figure 3.19, we will use the developed group leaf pattern [41] to model its group scattering pattern and the backscattering coefficient. The development of a scattering model for the compound-leaf pattern is described in the rest of this section.

Consider a plane wave impinging upon a circular disc located at the origin as shown in Figure 3.20. Use a dyadic representation for the incident plane wave [6][27] as (3.2).

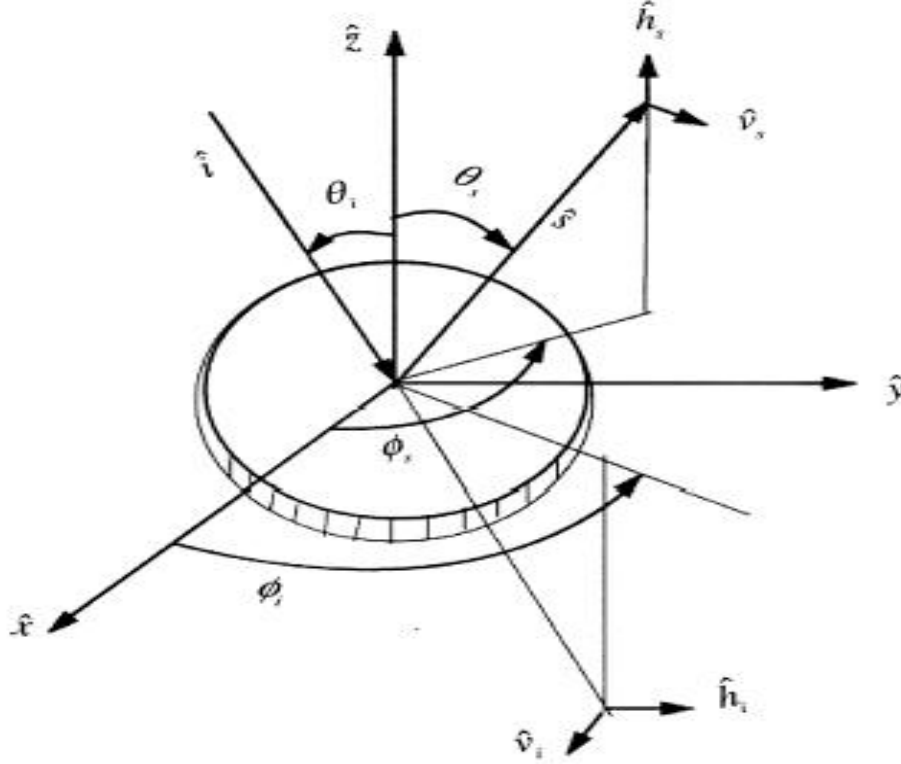


Figure 3.20 Geometry of the scattering problem

Following a similar procedure as shown in Section 3.2 Leaf Shape (Leaf Shape section), the scattered field of the circular disc can be written as

$$\begin{aligned}
 \bar{E}_s &= \frac{e^{-jkr}}{r} \cdot \frac{k^2}{4\pi} (\bar{I} - \hat{s}\hat{s}) \iiint (\epsilon_r - 1) \cdot \bar{E}_{in}(r') e^{jk(\hat{s} \cdot \bar{r}')} d\bar{r}' \\
 &= \frac{e^{-jkr}}{r} \frac{k^2}{4\pi} (\epsilon_r - 1) (\hat{I} - \hat{s}\hat{s}) \cdot \bar{\alpha} \cdot \hat{q}_i E_0 \int e^{-jk\bar{r} \cdot (\hat{i} - \hat{s})} d\bar{r}' \\
 &= \bar{\bar{F}}(\hat{s}, \hat{i}) \cdot \bar{E}_0 \frac{e^{-jkr}}{r}
 \end{aligned} \tag{3.47}$$

where the scattering amplitude tensor  $\bar{\bar{F}}(\hat{s}, \hat{i})$  is given by

$$\bar{\bar{F}} = \frac{k^2}{4\pi}(\epsilon_r - 1)(\hat{I} - \hat{s}\hat{s}) \cdot \bar{\alpha} \cdot \hat{q}_i E_0 \int e^{-jk\bar{r}} \cdot (\hat{i} - \hat{s}) d\bar{r} \quad (3.48)$$

For the odd-pinnately compound leaf given in Figure 3.19, we model it as shown in Figure 3.21. We assume the center of the leaf, which is not in pair with any other leaves, is located at

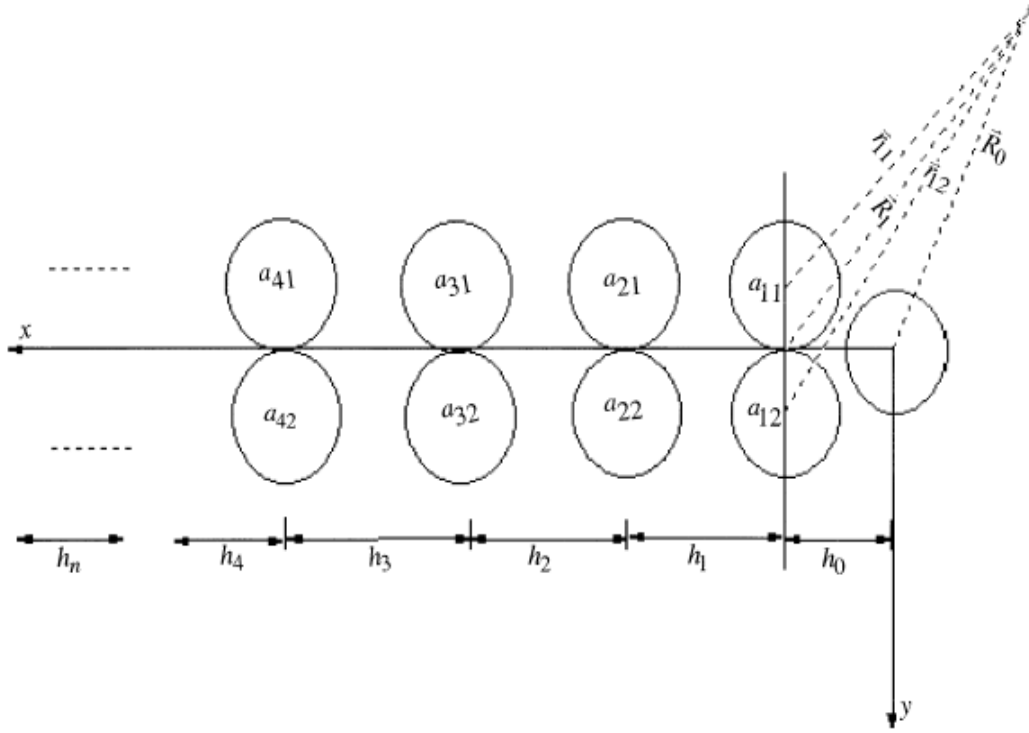


Figure 3.21 Theoretical model for an odd-pinnately compound leaf

the origin. The direction of the stem is along the  $x$ -axis and the leaves are lying in the  $xy$  plane. The diameter of a leaf in the  $n^{\text{th}}$  pair is  $a_{ni}$ , and the spacing between the centers of adjacent leaves is  $h_n$ . The distances  $R_0$ ,  $R_n$ , and  $r_{ni}$  are from the observation point to the origin, to the joining point of a leaf-pair along the stem and to the center of a leaf in pair with another leaf respectively.

$$\bar{R}_0 = R_0 \hat{r} \quad (3.49)$$

$$\bar{R}_n = \bar{R}_0 + \sum_{i=1}^{n-1} \bar{h}_i \text{ and } \bar{h}_i = \hat{x}h_i \quad (3.50)$$

$$\bar{r}_{n1} = \bar{R}_n - \frac{a_{n1}}{2}\hat{y} \quad (3.51)$$

$$\bar{r}_{n2} = \bar{R}_n + \frac{a_{n2}}{2}\hat{y} \quad (3.52)$$

For the pair of leaves linked to  $\bar{r}_{n1}$  and  $\bar{r}_{n2}$ , the total scattered field is the sum,

$$\bar{E}_{tn}^s = \bar{E}_{n1}^s + \bar{E}_{n2}^s \quad (3.53)$$

where

$$\bar{E}_{ni}^s = \bar{F}(\hat{s}, \hat{i}) \cdot \bar{E}_0 \frac{e^{-jkr_{ni}}}{r_{ni}} ; \bar{r}_{ni} = \bar{R}_n + \bar{d}_{ni}, \text{ and } \bar{d}_{ni} = \pm \hat{y}a_{ni}/2 \quad (\text{"-" for } i=1, \text{ "+" for } i=2)$$

The scattered field of a group of N-leaves with odd-pinnately pattern can be expressed as

$$\begin{aligned} \bar{E}_t^s &= \bar{E}_0^s + \sum_{m=1}^{\frac{N-1}{2}} \bar{E}_{tm}^s \\ &= \bar{F}(\hat{s}, \hat{i}) \cdot \bar{E}_0 \frac{e^{-jkR_0}}{R_0} + \sum_{m=1}^{\frac{N-1}{2}} \sum_{l=1}^2 \bar{F}(\hat{s}, \hat{i}) \cdot \bar{E}_0 \frac{e^{-jkr_{ml}}}{r_{ml}} \end{aligned} \quad (3.54)$$

In the far-zone, we approximate  $r_{ml}$  in the amplitude by  $R_0$  and in the phase by,

$$r_{ml} \approx R_0 + \bar{d}_{ml} \cdot \hat{r} + \sum_{j=0}^{m-1} \bar{h}_j \cdot \hat{r} \quad (3.55)$$

The far-zone scattered field for a group of N-leaves becomes

$$\begin{aligned} \bar{E}_t^s &\approx \bar{\bar{F}}(\hat{s}, \hat{i}) \left( 1 + \sum_{m=1}^{\frac{N-1}{2}} \sum_{l=1}^2 e^{-jk \left( \bar{d}_{ml} \cdot \hat{r} + \sum_{j=0}^{m-1} \bar{h}_j \cdot \hat{r} \right)} \right) \cdot \bar{E}_0 \frac{e^{-jkR_0}}{R_0} \\ &\equiv \bar{\bar{F}}_g(\hat{s}, \hat{i}) \cdot \hat{q} E_0 \frac{e^{-jkR_0}}{R_0} \end{aligned} \quad (3.56)$$

where  $\hat{q}$  is the unit polarization vector for the incident field.

From the (3.56), the scattering amplitude  $\bar{F}_g = \bar{\bar{F}}_g(\hat{s}, \hat{i}) \cdot \hat{q}$  of a group of N-leaves can be expressed as the product of the scattering amplitude  $\bar{\bar{F}}(\hat{s}, \hat{i}) \cdot \hat{q}$  of a single leaf and the array function  $\Phi$  given by

$$\Phi = 1 + \sum_{m=1}^{\frac{N-1}{2}} \sum_{l=1}^2 e^{-jk \left( \bar{d}_{ml} \cdot \hat{r} + \sum_{j=0}^{m-1} \bar{h}_j \cdot \hat{r} \right)} \quad (3.57)$$

If the leaves are of the same size and the spacing between the pairs of leaves are equal, i.e.,

$d_{ml} = d$  and  $h_i = h$ , then (3.57) simplifies to

$$\Phi = 1 + 2 \cos(kd \sin \theta_i \sin \phi_i) \sum_{m=1}^{\frac{N-1}{2}} e^{-jkmh \sin \theta_i \cos \phi_i} \quad (3.58)$$

For a receiving antenna with  $p$ -polarization the backscattering coefficient of a half-space of leaves can be written as [6]

$$\sigma_{gpq}(-\hat{i}, \hat{i}) = 4\pi \cos\theta_i \frac{\langle |\overline{F}_{gpq}(-i, i)|^2 \rangle}{\langle \kappa_p(-\hat{i}) \rangle + \langle \kappa_q(\hat{i}) \rangle} \quad (3.59)$$

where the ensemble average,  $\langle |\overline{F}_{gpq}(-i, i)|^2 \rangle = \int d\alpha \int p(\alpha) p(\beta) |\overline{F}_{gpq}(-i, i)|^2 d\beta$ , is over the leaf orientation;  $p(\alpha)$  and  $p(\beta)$  are the probability distribution functions of the leaf orientations and  $\kappa_p(\hat{i})$  is the extinction cross section for the group of scatterers given by

$$\kappa = -\frac{4\pi}{k} \text{Im}[\overline{F}_{gpp}(-i, i)] \quad (3.60)$$

### 3.4.2 Scattering Pattern

In this section, we will focus on studying the effects of variations of the leaf radius, the spacing of adjacent leaves, and the number of leaves in a group on backscattering, when the dielectric constant is taken to be 14.9-j4.9 and the incident electromagnetic wave is at 3.5 GHz.

First, we consider the effect of changing the leaf size on the scattering behaviors of VV, HH, and VH polarization. The illustrations are shown in figures 3.22, 3.23, and 3.24 where spacing between adjacent leaves is taken as 10cm and number of leaves in a group is 5. With the increasing of the radius of the circular disc, the amplitude of scattering pattern is increasing. Secondly, the spacing between adjacent leaves impact on scattering properties of VV, HH, and HV polarization scattering pattern over incident angle have been displayed at Figure 3.25, 3.26, and 3.27 where the radius of the circular leaf is taken as 2cm, number of leaves in a group is 5. As the spacing between adjacent leaves is increasing, width of main lobe is

decreasing. In Figure 3.28, 3.29, and 3.30 where the radius of the circular leaf is taken as 4cm and spacing between adjacent leaves is 10cm, the scattering properties of VV, HH, and VH polarization scattering pattern over incident angle with respect to different number of leaves in a group have been demonstrated finally. The number of oscillations and dips in scattering pattern are increasing with the number of leaves in a group, the width of main lobe is decreasing and amplitude of mainlobe is leveled up and that of sidelobe is suppressed.

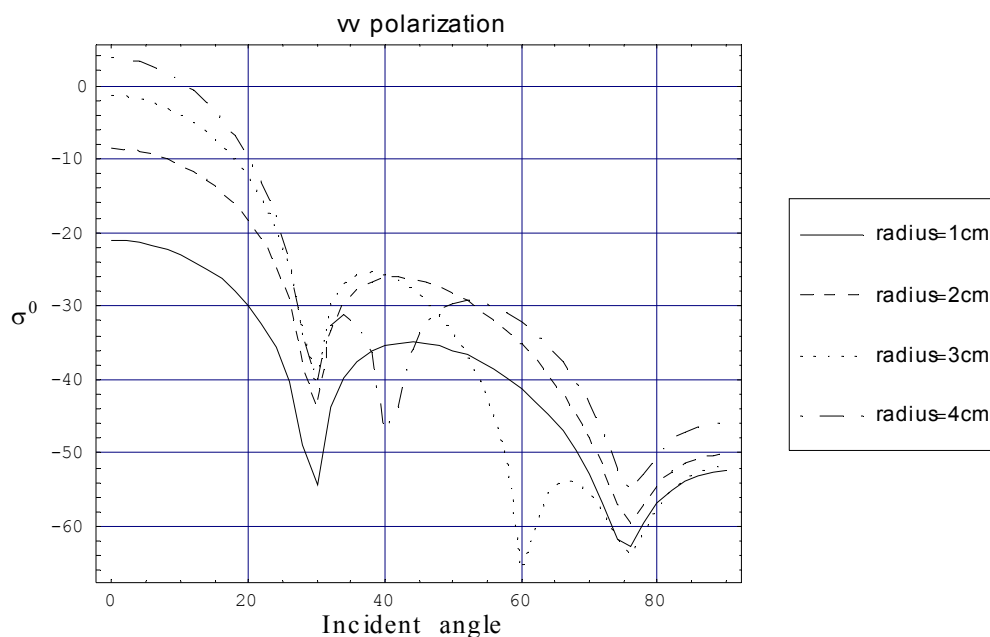


Figure 3.22 VV Scattering Pattern of a group leaves versus the incidence angle with different radius of each circular disc

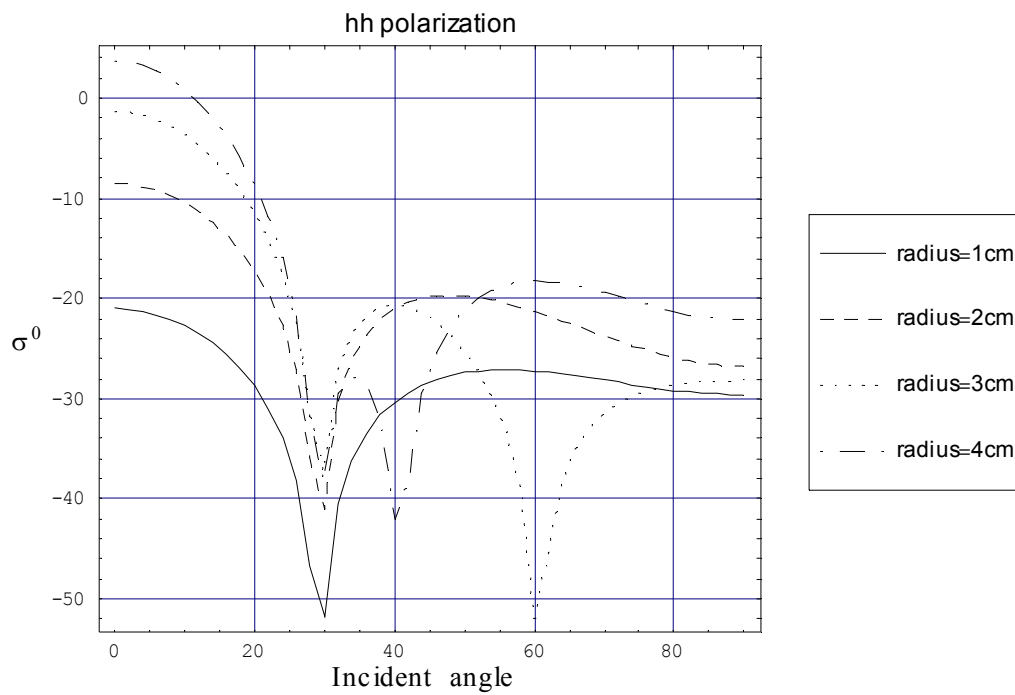


Figure 3.23 HH Scattering Pattern of a group leaves versus the incidence angle with different radius of each circular disc.

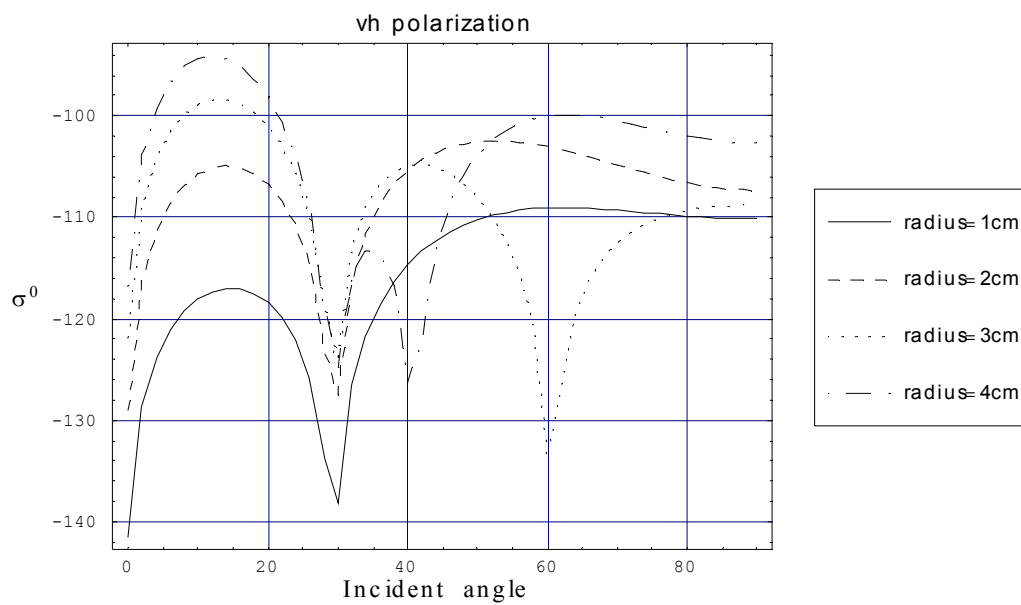


Figure 3.24 VH Scattering Pattern of a group leaves versus the incidence angle with respective to different radius of each circular disc



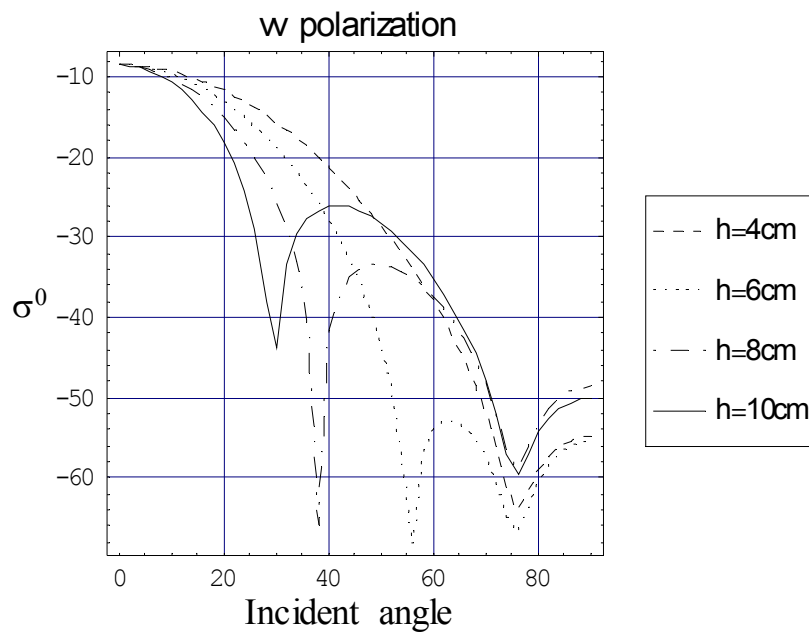


Figure 3.25 VV Scattering Pattern of a group leaves versus the incidence angle with respective to different spacing between adjacent leaves

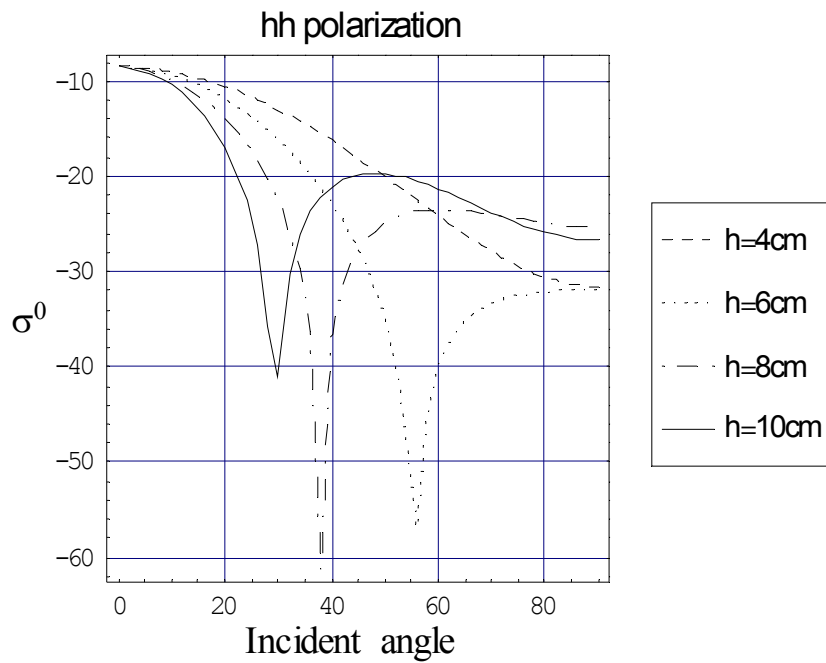


Figure 3.26 HH Scattering Pattern of a group leaves versus the incidence angle with respective to different spacing between adjacent leaves

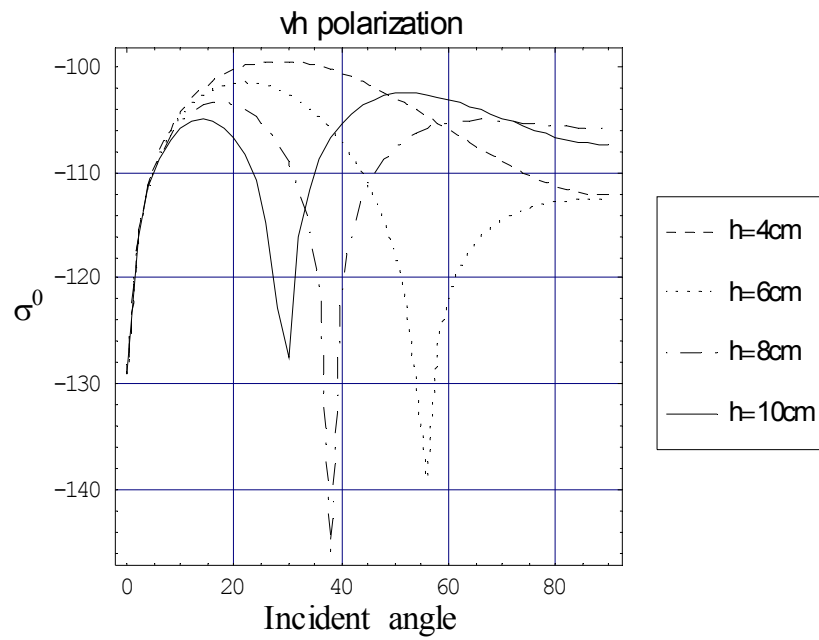


Figure 3.27 VH Scattering Pattern of a group leaves versus the incidence angle with respect to different spacing between adjacent leaves

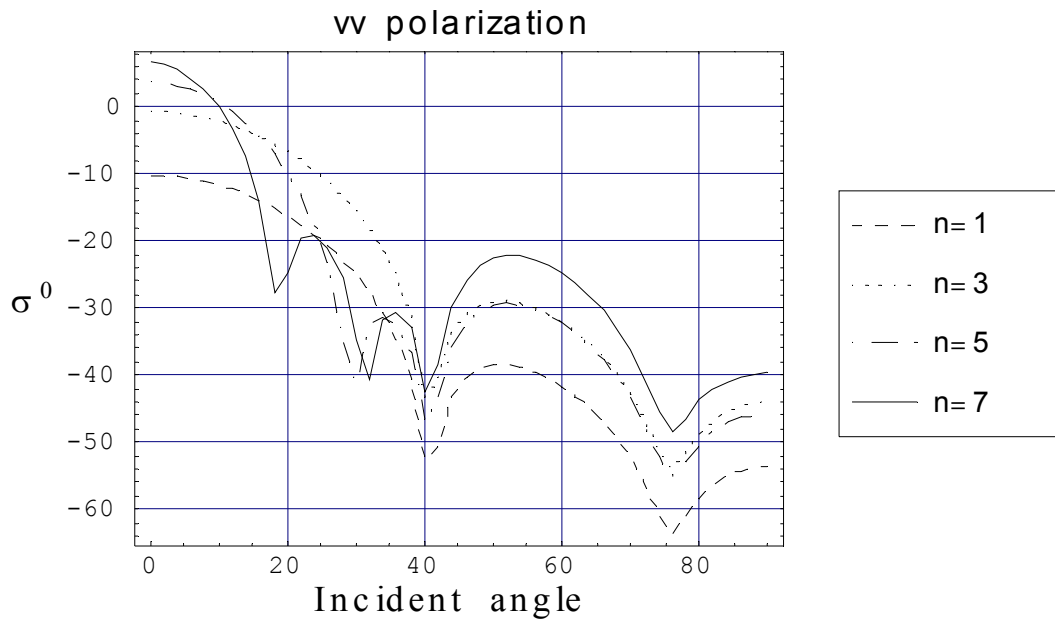


Figure 3.28 VV Scattering Pattern of a group leaves versus the incidence angle with respect to different number of leaves in a group

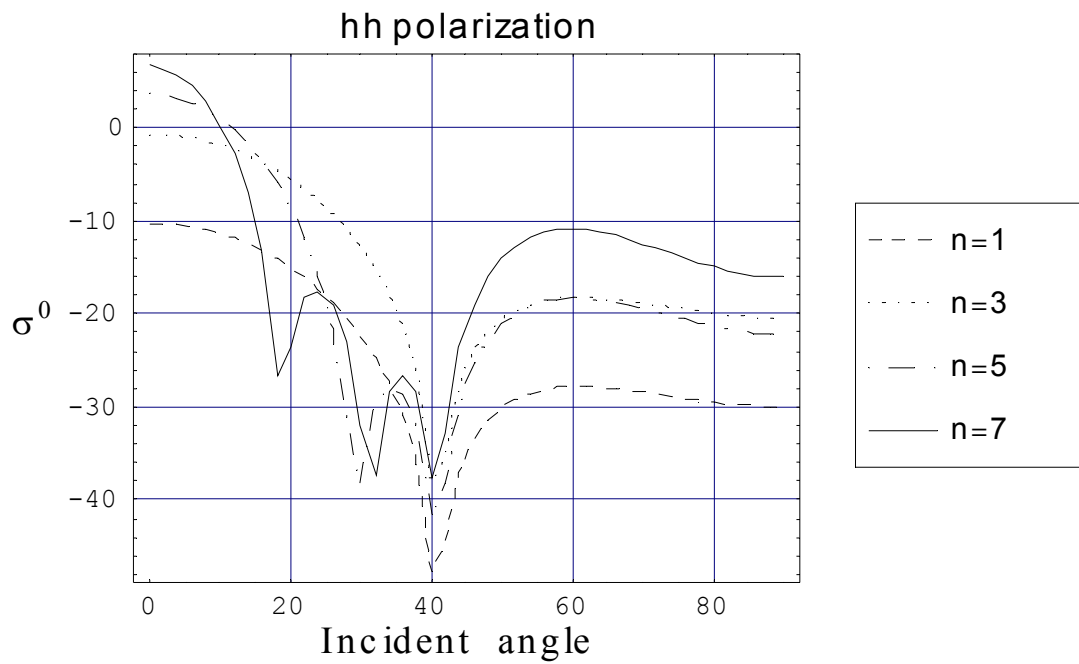


Figure 3.29 HH Scattering Pattern of a group leaves versus the incidence angle with respect to different number of leaves in a group

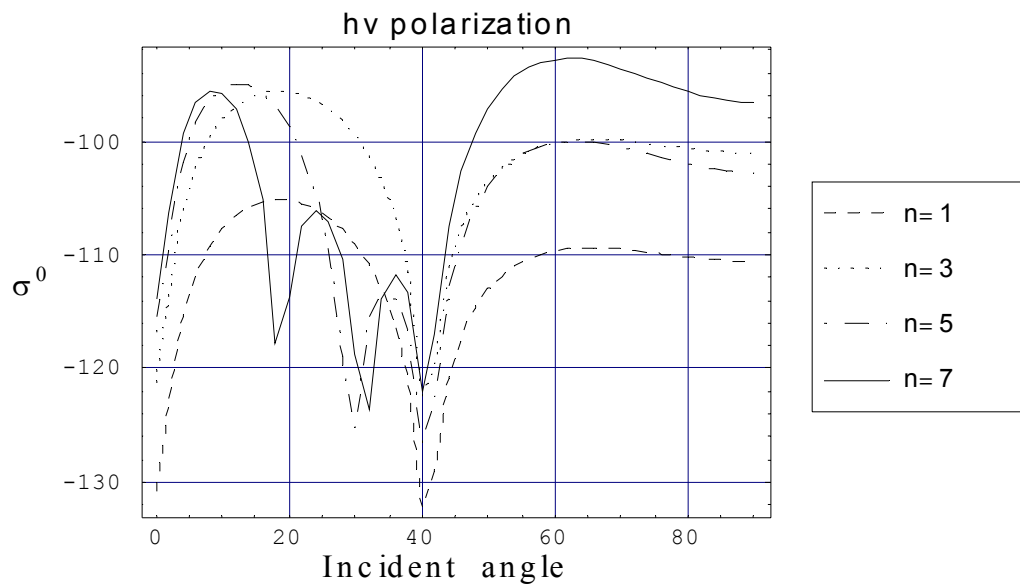


Figure 3.30 HV Scattering Pattern of a group leaves versus the incidence angle with respect to different number of leaves in a group

### 3.4.3 Orientation Distribution Effects

In this section, the backscattering coefficients relative to orientational distribution has been studied where the radius of leaf is taken as 4cm, spacing between adjacent leaves is 10cm, and number of leaves in a group is 13. The scattering properties of VV and VH polarization over the incident angle with respect to different range of  $\beta$  have been shown in the Figure 3.31 and 3.32 respectively. Variation of orientation distribution of the tilt angle  $\beta$  has been selected increasing as  $0^\circ < \beta < 30^\circ$ ,  $0^\circ < \beta < 45^\circ$ ,  $0^\circ < \beta < 60^\circ$  and  $0^\circ < \beta < 90^\circ$ . The tail of angular curve of backscattering coefficient level up gradually with range of  $\beta$  increasing. Due to coherence induced by scattering of group leaves, the oscillations appear in the curve of backscattering coefficient over the incident angles which is impossible for scattering from single leaves.

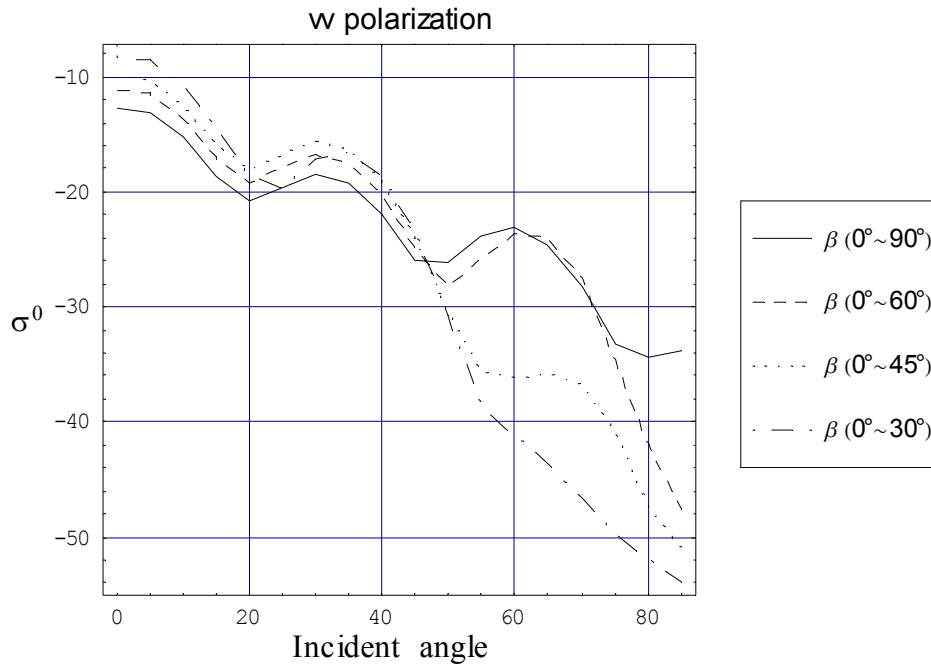


Figure 3.31 VV backscattering coefficient of a group leaves versus the incidence angle with respect to different distribution of the tilt angle  $\beta$  for  $0^\circ < \alpha < 360^\circ$

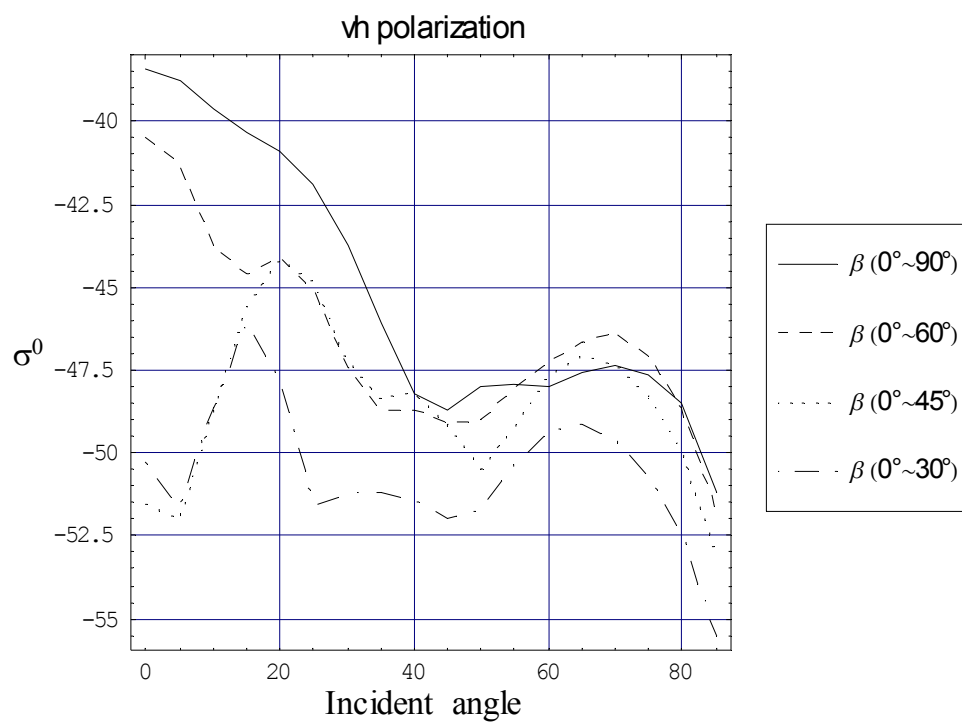


Figure 3.32 VH backscattering coefficient of a group levees versus the incidence angle with repsective to different orientation distribution of the tilt angle  $\beta$  for  $0^\circ < \alpha < 360^\circ$

### 3.5 A cone-like needle cluster pattern



Figure 3.33 Needles Growing in Clusters

#### 3.5.1 Formulation

The needles of some coniferous vegetation are growing together and will scatter together. The scattering of needles in a cluster will be modelled as discussed in the following paragraphs.

An example of a coniferous vegetation with needles growing in clusters is shown in Figure 3.33. An idealized model for a cluster of needles is shown in Figure 3.34. The cluster of needles is assumed to take on a cone-shape centered at the origin of a spherical coordinate system. The cone is divided into  $n$  rings along the radial directions in the  $\theta$ -plane, such that the spacing between the adjacent needles is  $\Delta\theta$ . Similarly, there are  $m$  needles along the azimuthal plane and the spacing between the adjacent needles is  $\Delta\phi$ . It is required that  $m\Delta\phi = 2\pi$  and  $n\Delta\theta$  is equal to the specified width of the cone.

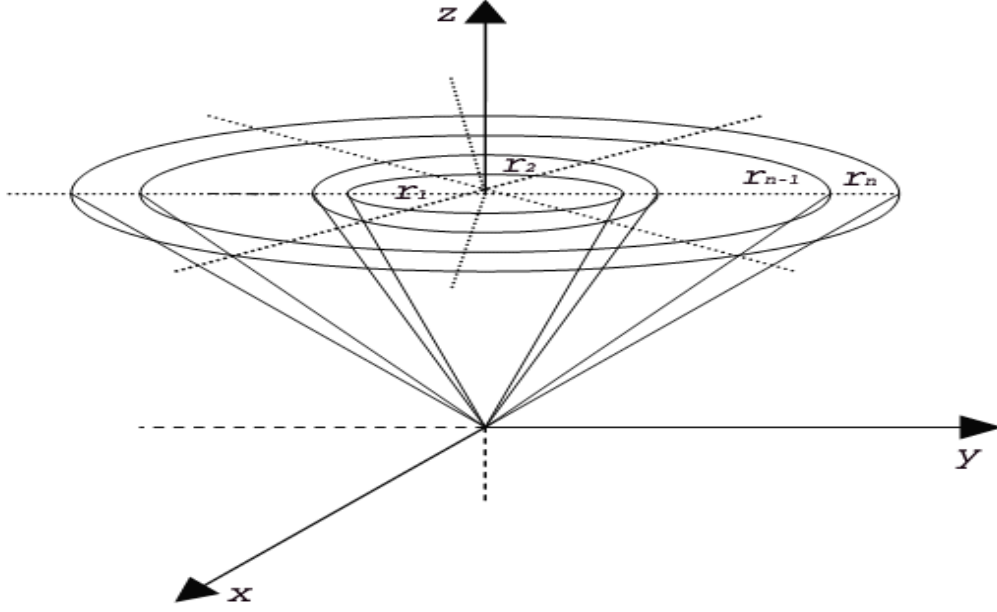


Figure 3.34 Theoretical model for a cluster of needles

Each needle is modelled as an ellipsoid with radius  $r_0 = a_{mn}$ , length  $L = l_{mn}$  and  $a_{mn} \ll l_{mn}$ . The scattered field for a needle sitting at the origin can be written as

$$\vec{E}^s = \bar{\bar{F}}(\hat{s}, \hat{i}) \cdot \vec{E}_0 \frac{\exp(-j\vec{k} \cdot \vec{r})}{r} \quad (3.61)$$

where  $\bar{\bar{F}}(\hat{s}, \hat{i})$  is the scattering amplitude matrix for a needle,  $\hat{s} = \hat{s}(\theta_s, \phi_s)$  and  $\hat{i} = \hat{i}(\theta_i, \phi_i)$  are the scattering and incident unit propagation vectors respectively.

The total scattered field of a cluster of needles shown in Figure 3.34 can be written in terms of the scattered field of a needle sitting along the z-axis denoted as  $\vec{E}_{00}^s$  by redefining the incident and the scattering direction for each needle in the reference frame as follows

$$\begin{aligned}
\vec{E}_t^s &= \vec{E}_{00}^s + \sum_{n=1}^N \sum_{m=1}^M \vec{E}_{nm}^s \\
&= \bar{\bar{F}}(\hat{s}, \hat{i}) \cdot \vec{E}_0 \frac{\exp(-j\vec{k} \cdot \vec{r})}{r} + \sum_{n=1}^N \sum_{m=1}^M \bar{\bar{F}}(\hat{s}_{nm}, \hat{i}_{nm}) \cdot \vec{E}_0 \frac{\exp(-j\vec{k} \cdot \vec{r})}{r} \\
&= \bar{\bar{F}}_{cgpq}(\hat{s}, \hat{i}) \cdot \vec{E}_0 \frac{\exp(-j\vec{k} \cdot \vec{r})}{r}
\end{aligned} \tag{3.62}$$

where

$$\hat{s}_{nm} = \hat{s} \left( \theta_s + \sum_{l=1}^n l \Delta \theta, \phi_s + \sum_{p=1}^m p \Delta \phi \right) \tag{3.63}$$

$$\hat{i}_{nm} = \hat{i} \left( \theta_i + \sum_{l=1}^n l \Delta \theta, \phi_i + \sum_{p=1}^m p \Delta \phi \right) \tag{3.64}$$

and

$$\bar{\bar{F}}_{cgpq}(\hat{s}, \hat{i}) = \bar{\bar{F}}(\hat{s}, \hat{i}) + \sum_{n=1}^N \sum_{m=1}^M \bar{\bar{F}}(\hat{s}_{nm}, \hat{i}_{nm}) \tag{3.65}$$

### 3.5.2 Scattering Pattern

The scattering pattern of a cluster of needles is expected to change with the length of the needles, the number of needles  $m$  in a ring as defined  $\Delta \phi$  and the number of rings  $n$ , after  $\Delta \theta$  is given. As shown in figures 3.35, 3.36 and 3.37 for VV, HH and HV polarizations, an increase in the length of the needles causes the magnitude of the main lobe to go up and its width to narrow. Due to coherent calculation, there are oscillations in all polarizations except for the shortest needle length in HH and HV polarization. Next, we consider the change in the number of needles along the  $\phi$ -plane, while the width of the cone is fixed. This study is shown in figures 3.38, 3.39, and 3.40. It is seen that there is a gradual increase on the average level and a



reduction in the width of the mainlobe as the number of needles increases. The maximum value for like polarization occurs at 90 degrees incidence, while for cross polarization, it is around 65 degrees. Finally, we consider in figures 3.41, 3.42, and 3.43, a change in the number of needles on the  $\theta$ -plane. It turns out that the trend behaviors are quite similar to those when the number of needles is increased in the  $\theta$ -plane, i.e., there is a gradual increase in the magnitude of the mainlobe around 90 degrees accompanied by a reduction in the width of the mainlobe. Again, the maximum for cross polarization is around 70 degree, while for like polarization it is at 90 degrees.

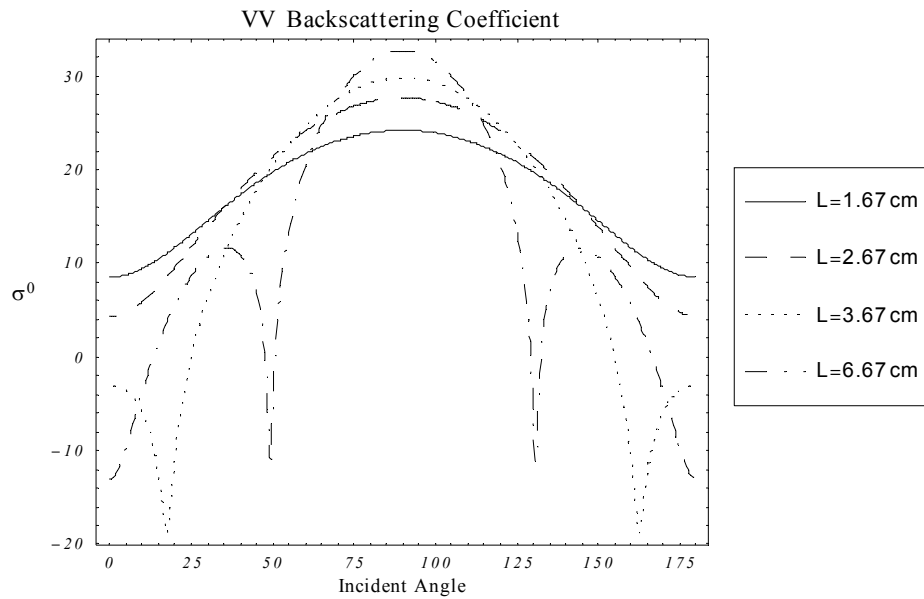


Figure 3.35 VV Scattering Pattern of a cluster of needles versus the incidence angle for four different needle lengths (width of the cone is  $\pi/3$ ,  $\Delta\theta = \pi/24$  and  $\Delta\phi = \pi/5$ ; dimension of each needle: radius 0.17cm).

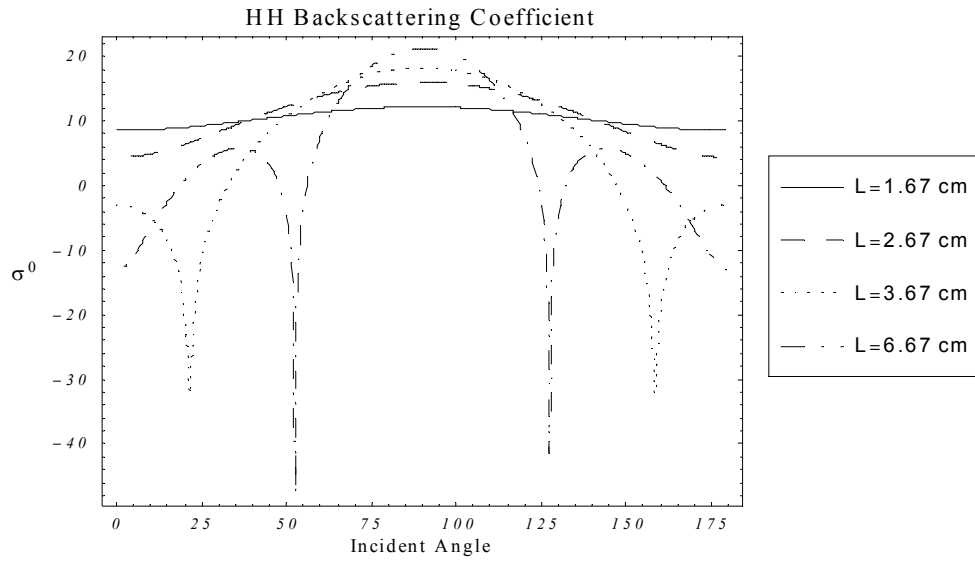


Figure 3.36 HH Scattering Pattern of a cluster of needles versus the incidence angle for four different needle lengths (width of the cone is  $\pi/3$ ,  $\Delta\theta = \pi/24$  and  $\Delta\phi = \pi/5$ ; dimension of each needle: radius 0.17cm).

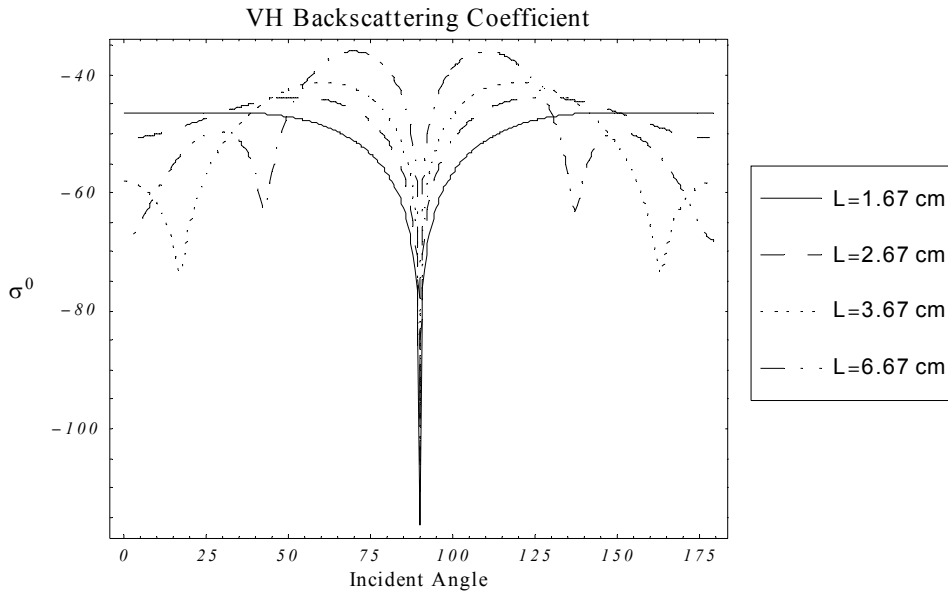


Figure 3.37 HV Scattering Pattern of a cluster of needles versus the incidence angle for four different needle lengths (width of the cone is  $\pi/3$ ,  $\Delta\theta = \pi/24$  and  $\Delta\phi = \pi/5$ ; dimension of each needle: radius 0.17cm).

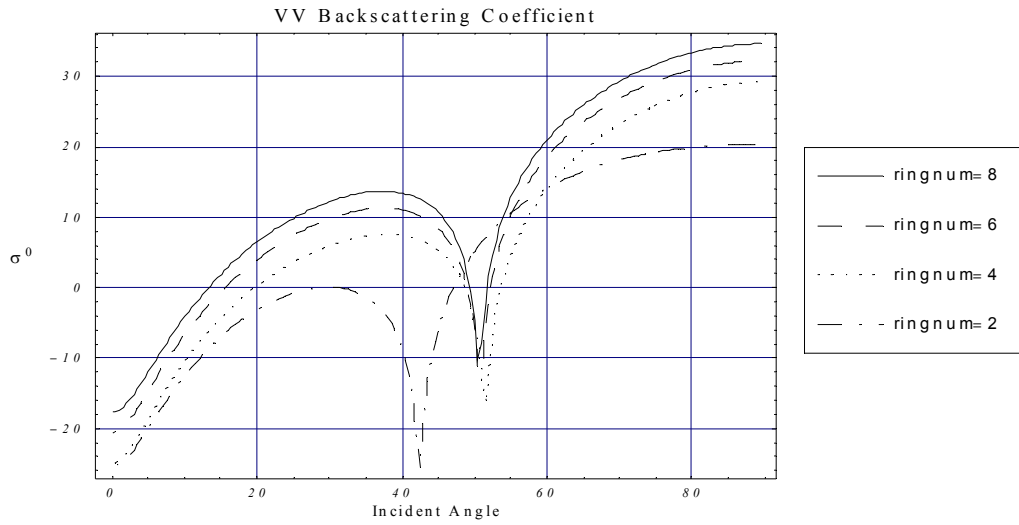


Figure 3.38 VV Scattering Pattern of a cluster of needles versus the incidence angle when the number of needles in the  $\phi$ -plane changes (width of the cone is  $\pi/3$ ,  $\Delta\theta = \pi/(36)$  and  $\Delta\phi = (2\pi)/ringnum$ ; dimension of each needle: length 6.67 cm and radius 0.17cm).

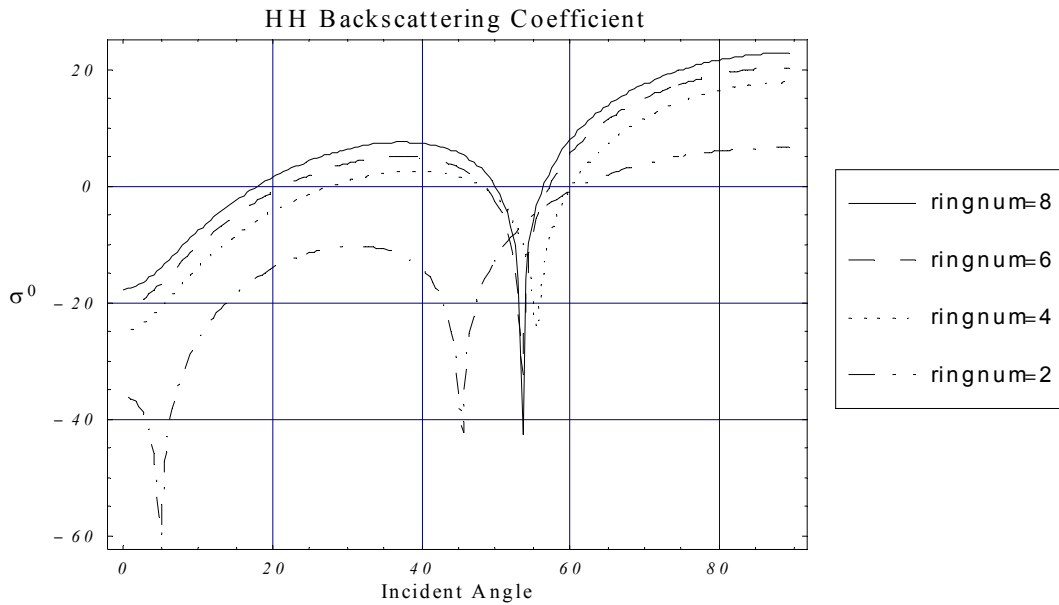


Figure 3.39 HH Scattering Pattern of a cluster of needles versus the incidence angle when the number of needles in the  $\phi$ -plane changes (width of the cone is  $\pi/3$ ,  $\Delta\theta = \pi/(36)$  and  $\Delta\phi = (2\pi)/ringnum$ ; dimension of each needle: length 6.67 cm and radius 0.17cm).

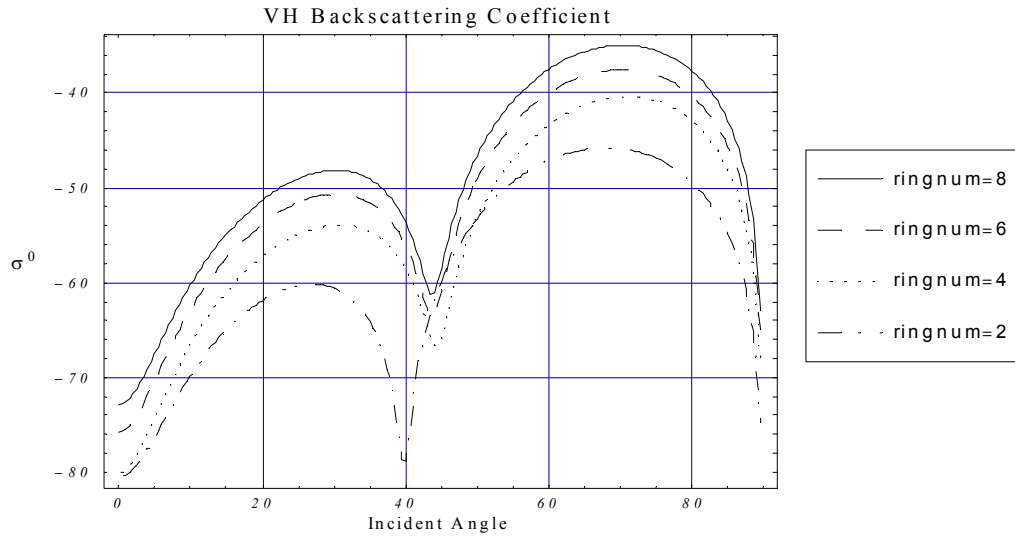


Figure 3.40 VH Scattering Pattern of a cluster of needles versus the incidence angle when the number of needles in the  $\phi$ -plane changes (width of the cone is  $\pi/3$ ,  $\Delta\theta = \pi/(36)$  and  $\Delta\phi = (2\pi)/ringnum$ ; dimension of each needle: length 6.67 cm and radius 0.17cm).

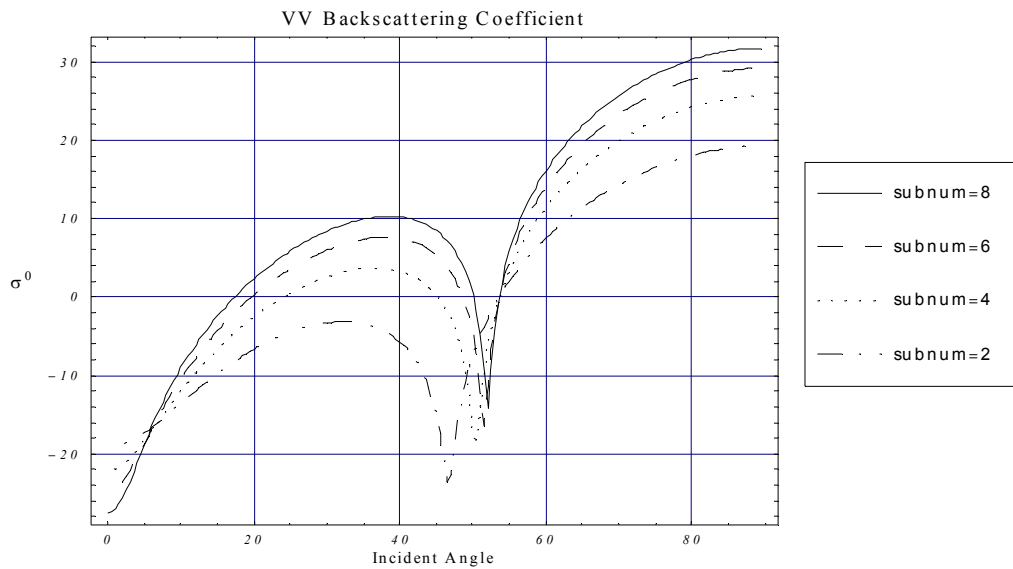


Figure 3.41 VV Scattering Pattern of a cluster of needles versus the incidence angle when the number of needles in the  $\theta$ -plane changes (width of the cone  $=\pi/3$ ,  $\Delta\theta = \frac{\pi/6}{subnum}$ ,

$\Delta\phi = \frac{\pi}{2}$ , Dimension of each needle: length 6.67 cm and radius 0.17cm).

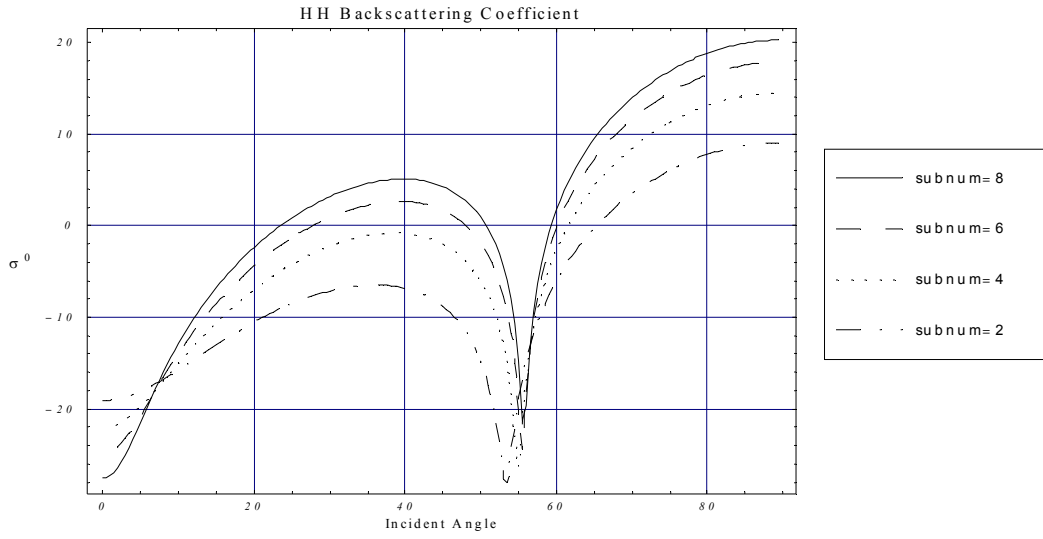


Figure 3.42 HH Scattering Pattern of a cluster of needles versus the incidence angle when the number of needles in the  $\theta$ -plane changes (width of the cone  $=\pi/3$ ,  $\Delta\theta = \frac{\pi/6}{subnum}$ ,

$\Delta\phi = \frac{\pi}{2}$ , Dimension of each needle: length 6.67 cm and radius 0.17cm)

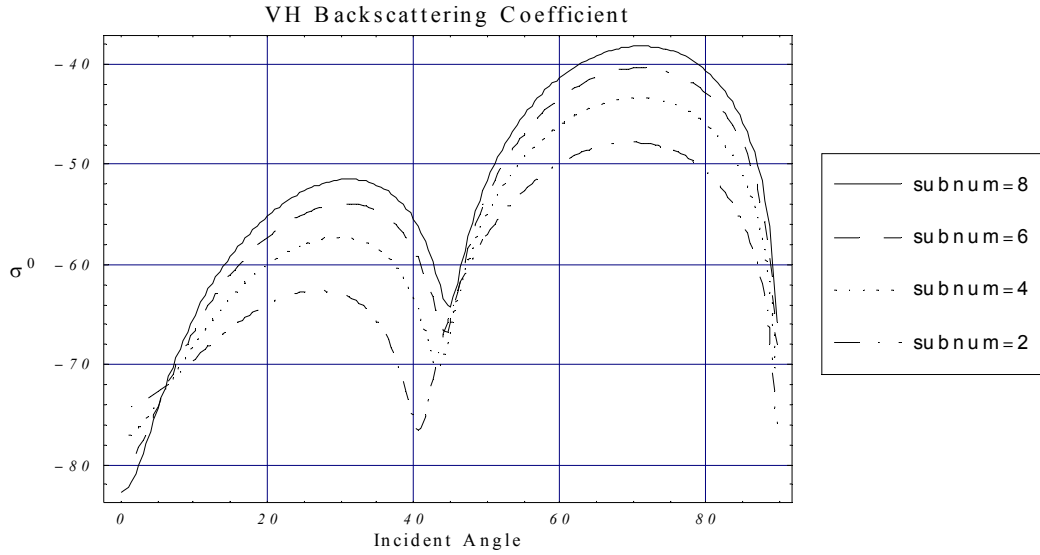


Figure 3.43 VH Scattering Pattern of a cluster of needles versus the incidence angle when the number of needles in the  $\theta$ -plane changes (width of the cone  $=\pi/3$ ,  $\Delta\theta = \frac{\pi/6}{subnum}$ ,

$\Delta\phi = \frac{\pi}{2}$ , Dimension of each needle: length 6.67 cm and radius 0.17cm)

### 3.5.3 Orientation Distribution effects

In this section, we will study the impact of the orientation distribution on the backscattering coefficient of a cluster of needles. Let the clusters of needles be nearly vertically distributed with ( $0^\circ < \beta < 30^\circ$ ). The results are shown in the figures 3.46 (VV), 3.45 (HH), and 3.46 (VH). For short needles, the backscattering coefficients are decreasing with the incidence angle. As the needle length increases, the angular trends change into a rise with the incidence angle. This change occurs for two reasons: (1) a short needle has a much more isotropic scattering pattern than the long needle, and (2) the illumination function decreases like a cosine function with angle. Next, we consider a nearly horizontal distribution, ( $30^\circ < \beta < 90^\circ$ ). For this case the backscattering coefficients are all decreasing with the incidence angle. Results are shown in figures 3.49 (VV), 3.48 (HH), and 3.49 (VH).

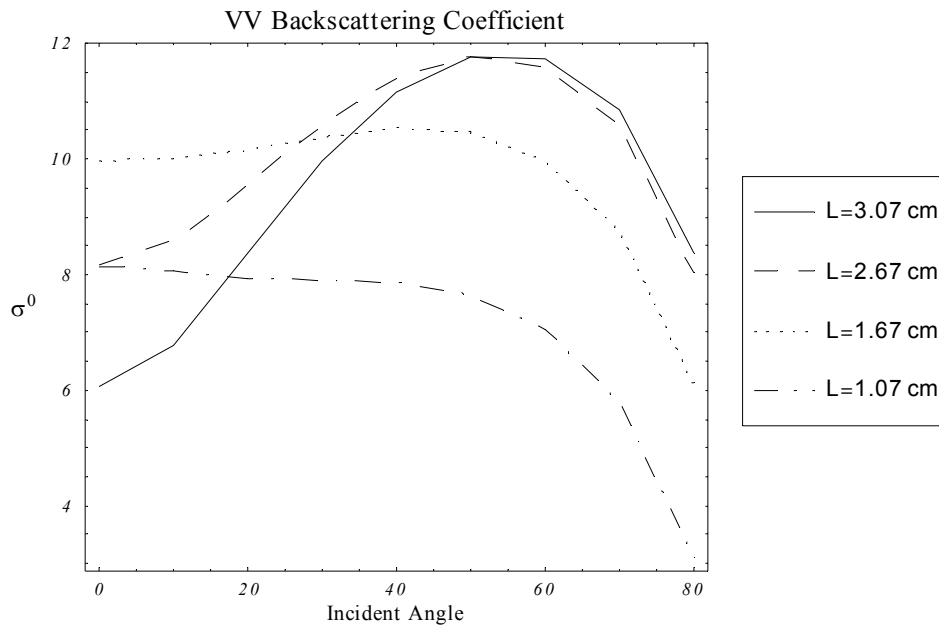


Figure 3.44 VV backscattering coefficient for randomly oriented cluster of needles versus the incidence angle with respective to different length of needles ( $0 < \beta < 30^\circ$ ,  $0^\circ < \alpha < 360^\circ$ , width of the cone is  $\pi/3$ ,  $\Delta\theta = \pi/24$  and  $\Delta\phi = \pi/5$ ; dimension of each needle: radius 0.17cm)

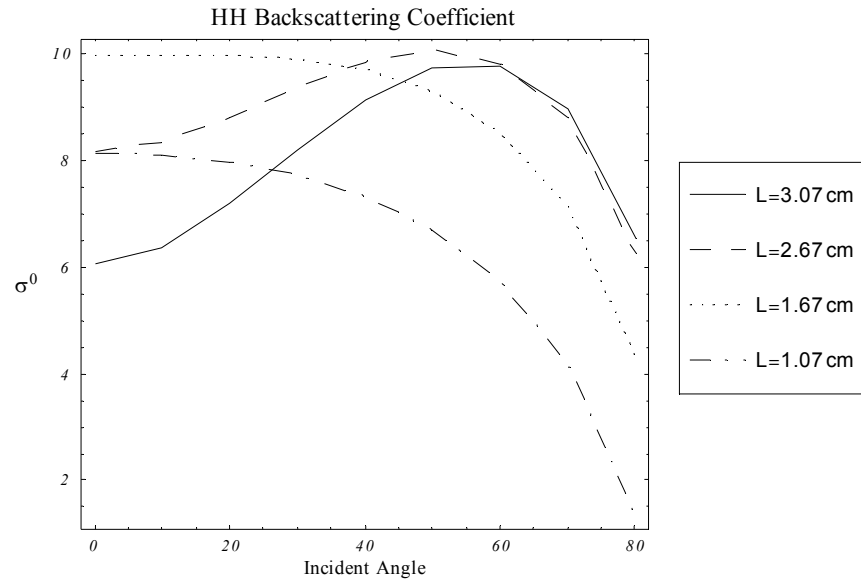


Figure 3.45 HH backscattering coefficient for randomly oriented cluster of needles versus the incidence angle with respective to different length of needles ( $0 < \beta < 30^\circ$ ,  $0^\circ < \alpha < 360^\circ$ , width of the cone is  $\pi/3$ ,  $\Delta\theta = \pi/24$  and  $\Delta\phi = \pi/5$ ; dimension of each needle: radius 0.17cm)

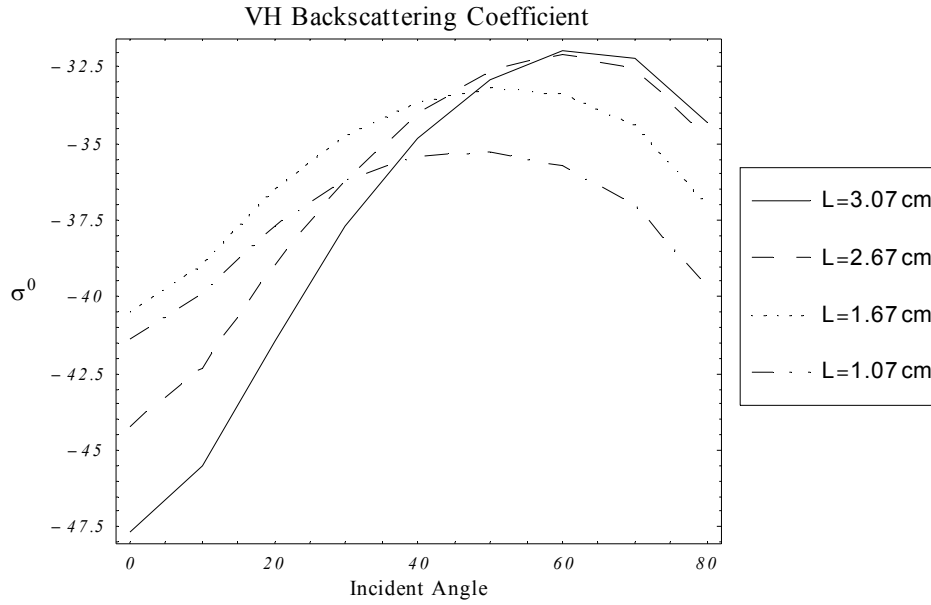


Figure 3.46 VH backscattering coefficient for randomly oriented cluster of needles versus the incidence angle with respect to different length of needles ( $0 < \beta < 30^\circ$ ,  $0^\circ < \alpha < 360^\circ$ , width of the cone is  $\pi/3$ ,  $\Delta\theta = \pi/24$  and  $\Delta\phi = \pi/5$ ; dimension of each needle: radius 0.17cm)

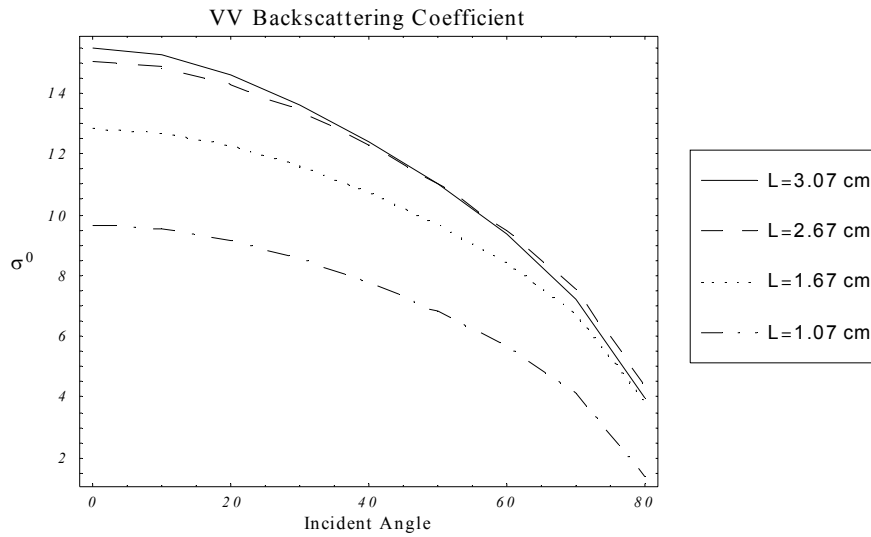


Figure 3.47 VV backscattering coefficient for randomly oriented cluster of needles versus the incident angle with respect to different length of needles ( $30^\circ < \beta < 90^\circ$ ,  $0^\circ < \alpha < 360^\circ$ , width of the cone is  $\pi/3$ ,  $\Delta\theta = \pi/24$  and  $\Delta\phi = \pi/5$ ; dimension of each needle: radius 0.17cm)



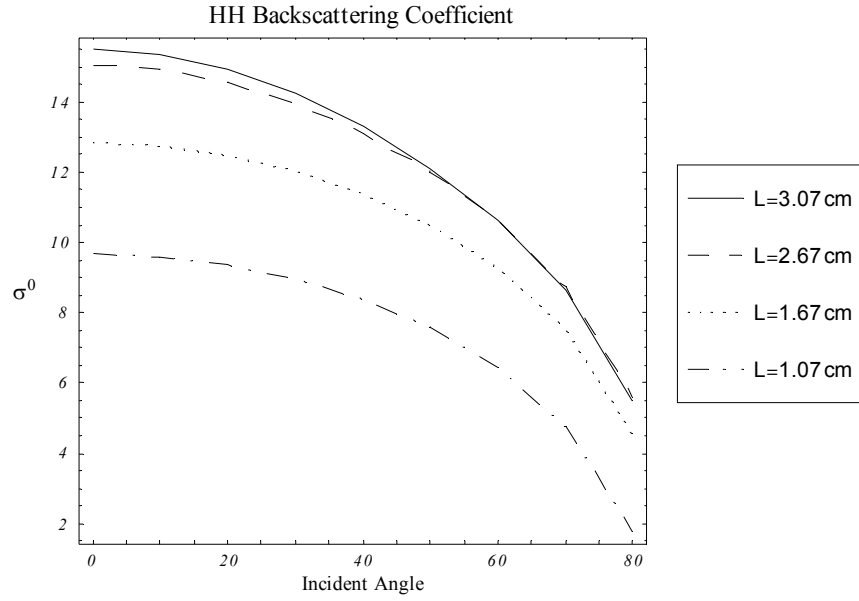


Figure 3.48 HH backscattering coefficient for randomly oriented cluster of needles versus the incidence angle with respect to different length of needles ( $30^\circ < \beta < 90^\circ$ ,  $0^\circ < \alpha < 360^\circ$ , width of the cone is  $\pi/3$ ,  $\Delta\theta = \pi/24$  and  $\Delta\phi = \pi/5$ ; dimension of each needle: radius 0.17cm)

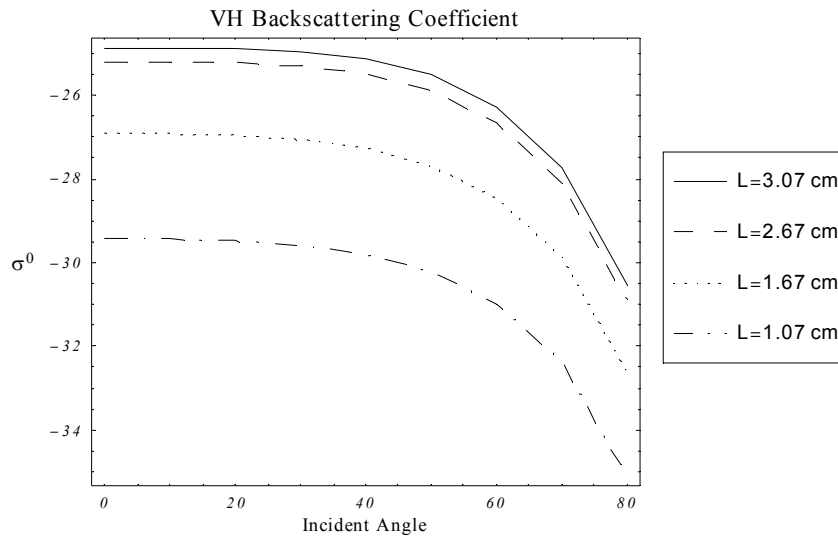


Figure 3.49 VH backscattering coefficient for randomly oriented cluster of needles versus the incidence angle with respect to different length of needles ( $30^\circ < \beta < 90^\circ$ ,  $0^\circ < \alpha < 360^\circ$ , width of the cone is  $\pi/3$ ,  $\Delta\theta = \pi/24$  and  $\Delta\phi = \pi/5$ ; dimension of each needle: radius 0.17cm)

## 3.6 Cylinder

### 3.6.1 Formulation

The trunks and branches are modelled as finite-length lossy dielectric circular cylinders [27] [33]. Consider a finite-length cylinder with radius  $a$ , length  $L$  and relative dielectric constant  $\epsilon_r$  illuminated by a plane wave as shown Figure 3.50.

Let the plane wave be written as

$$\vec{E}_i = \hat{q}_i E_0 e^{-jk(\hat{i} \cdot \vec{r})} \quad (3.66)$$

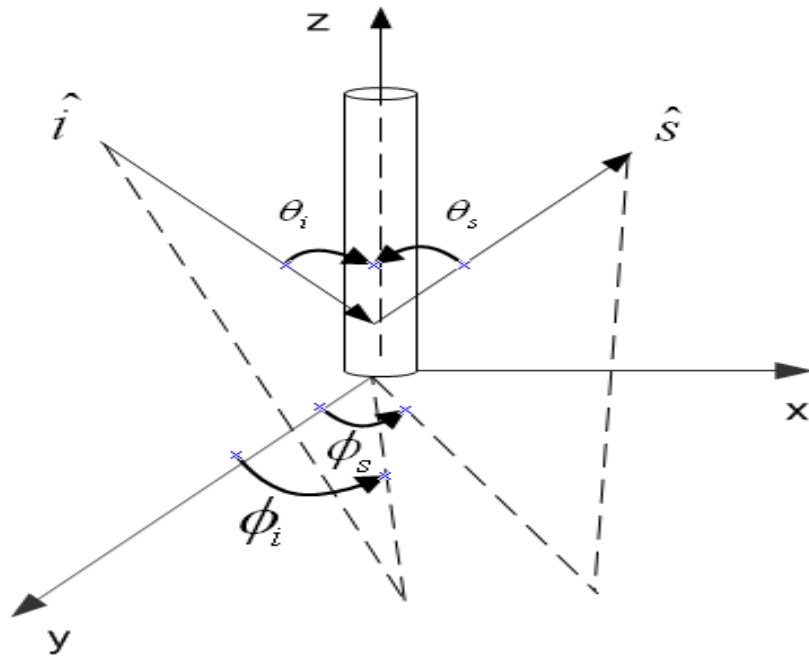


Figure 3.50 The geometry of the cylinder

where  $\hat{q}_i = \hat{v}_i$  or  $\hat{h}_i$  is the polarization vector and  $\hat{i}(\theta_i, \phi_i)$  is the incident unit vector. The field inside the cylinder is estimated by using the field inside a similar cylinder but of infinite length as

$$\bar{E}_{in}(r) = \sum_{q=v,h} E_{\rho q} \hat{\rho}' + E_{\phi q} \hat{\phi}' + E_{zq} \hat{z}' \quad (3.67)$$

where

$$\begin{aligned} E_{\rho q} &= \frac{k}{\lambda_i} \sum_{n=-\infty}^{\infty} \left\{ j \cos \theta_i e_{nq} J_n'(\lambda_i \rho') + n \frac{J_n(\lambda_i \rho')}{\lambda_i \rho'} \eta h_{nq} \right\} F_n \\ E_{\phi q} &= \frac{k}{\lambda_i} \sum_{n=-\infty}^{\infty} \left\{ -n \cos \theta_i e_{nq} \frac{J_n(\lambda_i \rho')}{\lambda_i \rho'} + j J_n'(\lambda_i \rho) \eta h_{nq} \right\} F_n \\ E &= \sum e_{nq} J_n(\lambda_i \rho') F_n \end{aligned} \quad (3.68)$$

where

$$F_n = E_0 j^{-n} \exp[jn(\phi' - \phi) + jkz' \cos \theta_i] \quad (3.69)$$

$$\begin{aligned} e_{nv} &= \frac{j \sin \theta_i}{R_n J_n(u)} \left\{ \frac{H_n^{(2)}(v_i)}{v_i H_n^{(2)}(v_i)} - \frac{J_n'(u)}{u J_n(u)} \right\} \\ \eta h_{nv} &= \frac{\sin \theta_i}{R_n J_n(u)} \left( \frac{1}{v_i^2 - u^2} \right) n \cos \theta_i \\ e_{nh} &= \frac{-\sin \theta_i}{R_n J_n(u)} \left( \frac{1}{v_i^2 - u^2} \right) n \cos \theta_i \\ \eta h_{nh} &= \frac{j \sin \theta_i}{R_n J_n(u)} \left( \frac{H_n^{(2)}(v_i)}{v_i H_n^{(2)}(v_i)} - \frac{\varepsilon_r J_n'(u)}{u J_n(u)} \right) \\ R_n &= \frac{\pi v_i^2 H_n^{(2)}(v_i)}{2} \left\{ \left( \frac{H_n^{(2)}(v_i)}{v_i H_n^{(2)}(v_i)} - \frac{J_n'(u)}{u J_n(u)} \right) \cdot \left( \frac{H_n^{(2)}(v_i)}{v_i H_n^{(2)}(v_i)} - \frac{\varepsilon_r J_n'(u)}{u J_n(u)} \right) \right. \\ &\quad \left. - \left( \frac{1}{u^2} - \frac{1}{v_i^2} \right)^2 n^2 \cos^2 \theta_i \right\} \\ u &= \lambda_i a = ka \sqrt{\varepsilon_r - \cos^2 \theta_i} \\ v &= ak \sin \theta_i \end{aligned}$$

and  $J_n(x)$  is the bessel function of the first kind and  $H_n^{(2)}(x)$  is the Hankel function of the second kind.

According to the Helmholtz integral equation, the scattering amplitude tensor element can be derived using (3.67) (3.68) and (3.69) as

$$F_{pq}(s, i) = k^2 L \mu(s, i) (\epsilon_r - 1) \quad (3.70)$$

$$\sum_{n=-\infty}^{\infty} e^{jn(\phi_s - \phi_i)} \left\{ \frac{k}{2\lambda_i} [(\eta h_{nq} - j e_{nq} \cos \theta_i)(\hat{p}_s \cdot \hat{x} + \hat{p}_s \cdot \hat{y}) z_{n+1} \right. \\ \left. e^{j\phi_s} - (\eta h_{nq} + j e_{nq} \cos \theta_i)(\hat{p}_s \cdot \hat{x} - \hat{p}_s \cdot \hat{y}) z_{n-1} e^{-j\phi_s}] + e_{nq} z_n (\hat{p}_s \cdot \hat{z}) \right\}$$

where

$$\mu(s, i) = \frac{\sin[0.5kL(\cos \theta_i + \cos \theta_s)]}{0.5kL(\cos \theta_i + \cos \theta_s)} \quad (3.71)$$

$$z_n = \frac{a^2}{u^2 - v_s^2} [u J_n(v_s) J_{n+1}(u) - v_s J_n(u) J_{n+1}(v_s)] \quad (3.72)$$

$$v_s = ak \sin \theta_s \quad (3.73)$$

Substituting the results of the vector dot products in (3.70), the explicit form of the scattering amplitude tensor elements can be expressed as

$$F_{vv}(\hat{s}, \hat{i}) = k^2 h(\epsilon_r - 1) \mu(\hat{s}, \hat{i}) \left\{ e_{0v} (B_0 \cos \theta_s \cos \theta_i - \sin \theta_s z_0) + \right. \\ \left. 2 \sum_{n=1}^{\infty} [(e_{nv} \cos \theta_i B_n - j \eta h_{nv} A_n) \cos \theta_s - \sin \theta_s e_{nv} z_n] \cos [n(\phi_s - \phi_i)] \right\} \quad (3.74)$$

$$F_{vh}(\hat{s}, \hat{i}) = jk^2 L(\epsilon_r - 1) \mu(\hat{s}, \hat{i}) \sum_{n=1}^{\infty} [(e_{nh} \cos \theta_i B_n - j \eta h_{nh} A_n) \cos \theta_s - \sin \theta_s e_{nh} z_n] \sin[n(\phi_s - \phi_i)] \quad (3.75)$$

$$F_{hv}(\hat{s}, \hat{i}) = jk^2 L(\epsilon_r - 1) \mu(\hat{s}, \hat{i}) \sum_{n=1}^{\infty} (\eta h_{nv} B_n + j \eta e_{nv} \cos \theta_i A_n) \sin[n(\phi_s - \phi_i)] \quad (3.76)$$

$$F_{hh}(s, i) = 0.5k^2 L(\epsilon_r - 1) \mu(s, i) \left\{ B_0 \eta h_{0h} + 2 \sum_{n=1}^{\infty} (\eta h_{nh} B_n + j e_{nh} \cos \theta_i A_n) \right\} \quad (3.77)$$

where

$$\begin{aligned} A_n &= \frac{k}{2\lambda_i} (z_{n-1} - z_{n+1}) \\ B_n &= \frac{k}{2\lambda_i} (z_{n-1} + z_{n+1}) \end{aligned} \quad (3.78)$$

### 3.6.2 Scattering Pattern

In this section, we shall study the behaviors of the radar cross section of a cylinder with respective to variations in its length and radius.

First, we consider in figures 3.51 (VV), 3.52 (HH) and 3.53 (VH) the backscattering coefficients for two different length of the cylinder,  $L = 5$  cm and  $L = 10$  cm. Similar to our study of the needle, a longer cylinder shows more oscillations than the short one and possesses a narrower and stronger mainlobe in like polarization. For cross polarization the peak values occurs 90 degrees away from those in like polarizations. Except for this difference, the backscattering pattern look similar to those of the like polarization but at much lower level.

Next, we study the effects of a change in the radius of the cylinder on backscattering. The results for three different choices of radius are shown in figures 3.54 (VV), 3.55 (HH) and

3.56 (VH). In this case an increase in the radius of the cylinder simply raises the level of scattering without changing the number of oscillations in the backscattering signal. This true for all polarizations.

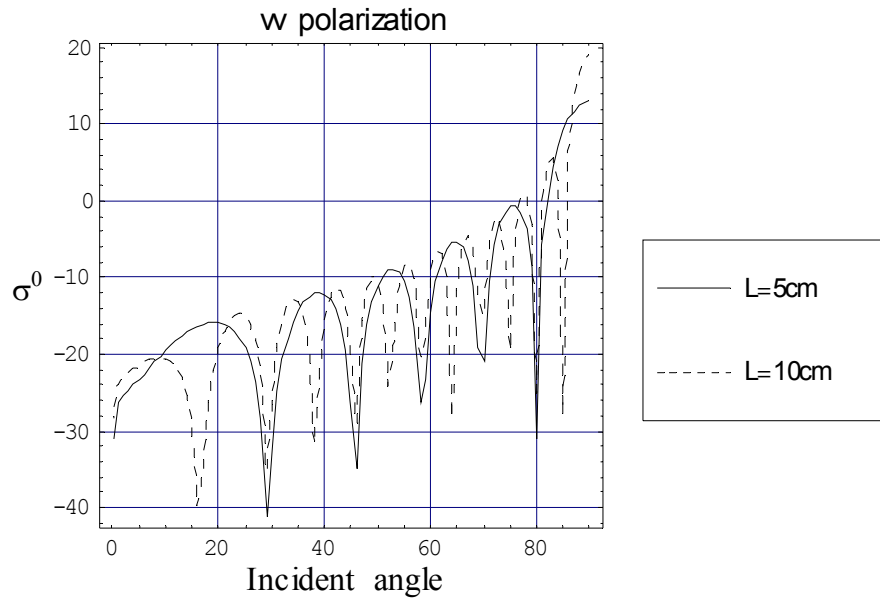


Figure 3.51 The VV scattering pattern of a cylinder versus the incidence angle for two different lengths of the cylinder ( $\epsilon_r = 29.6 - j7.1$ ).

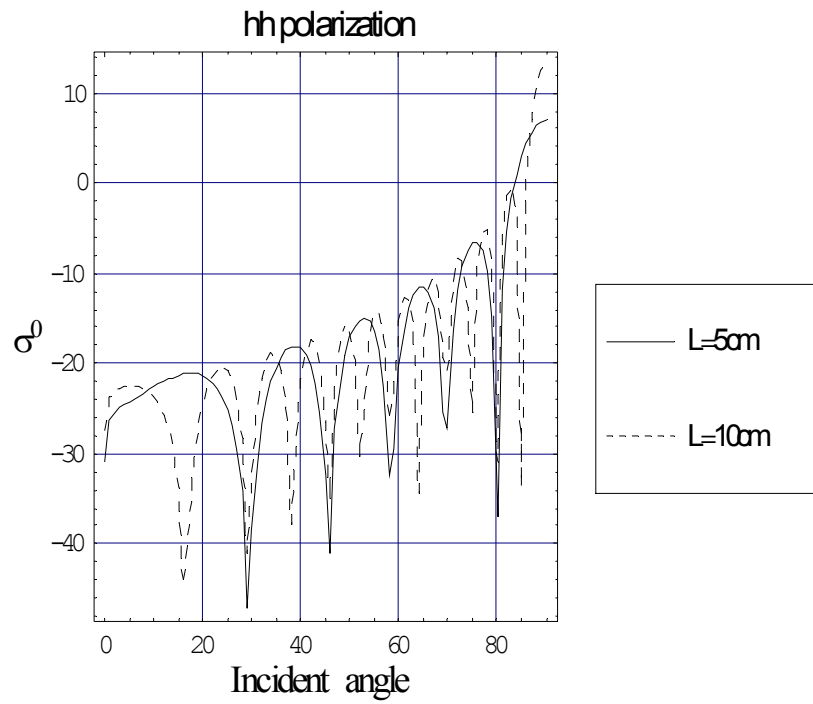


Figure 3.52 The HH scattering pattern of a cylinder versus the incidence angle for two different lengths of the cylinder ( $\epsilon_r = 29.6 - j7.1$ ).

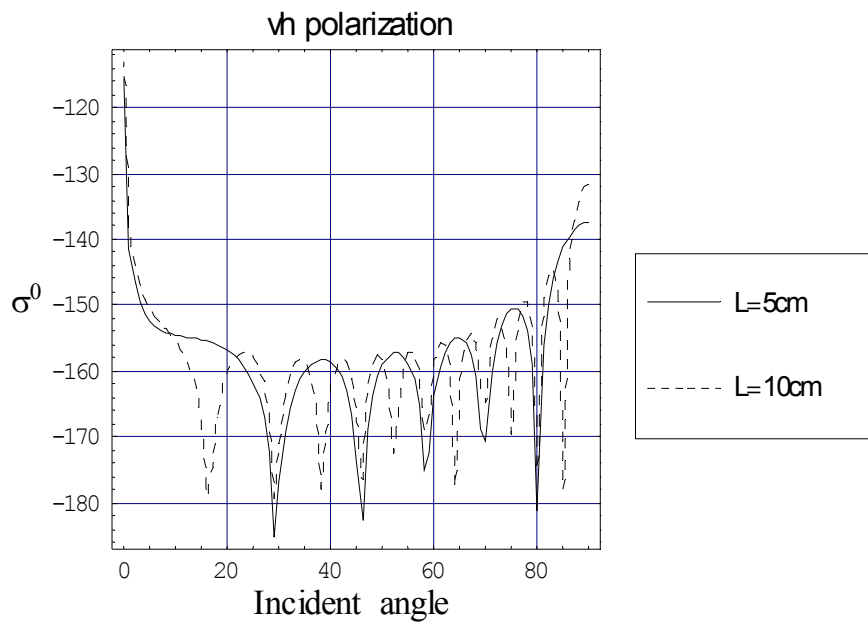


Figure 3.53 The VH scattering pattern of a cylinder versus the incidence angle for two different lengths of the cylinder ( $\epsilon_r = 29.6 - j7.1$ ).

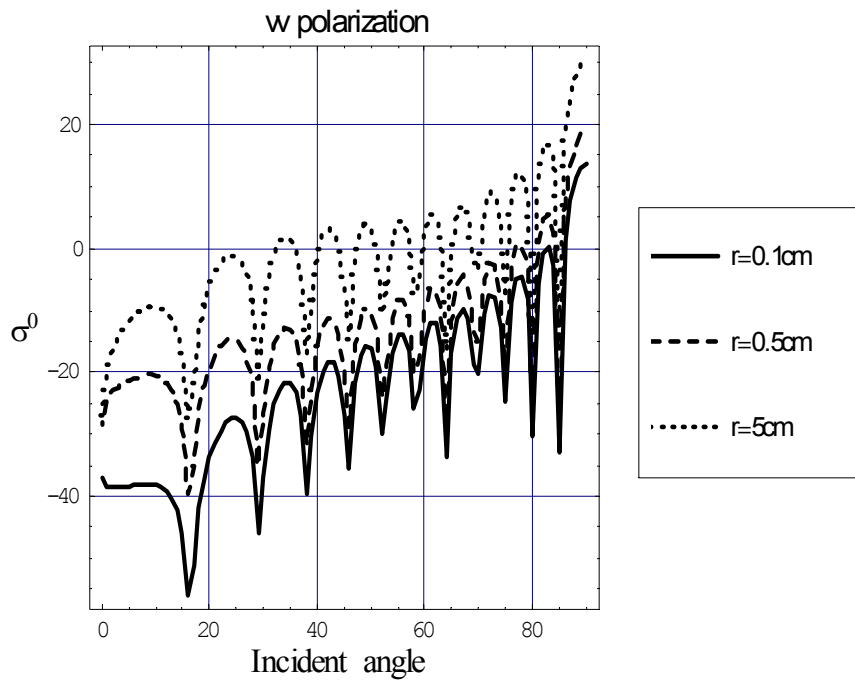


Figure 3.54 The VV scattering pattern of a cylinder versus the incidence angle for different radii of the cylinder ( $\epsilon_r = 29.6 - j7.1$ ).

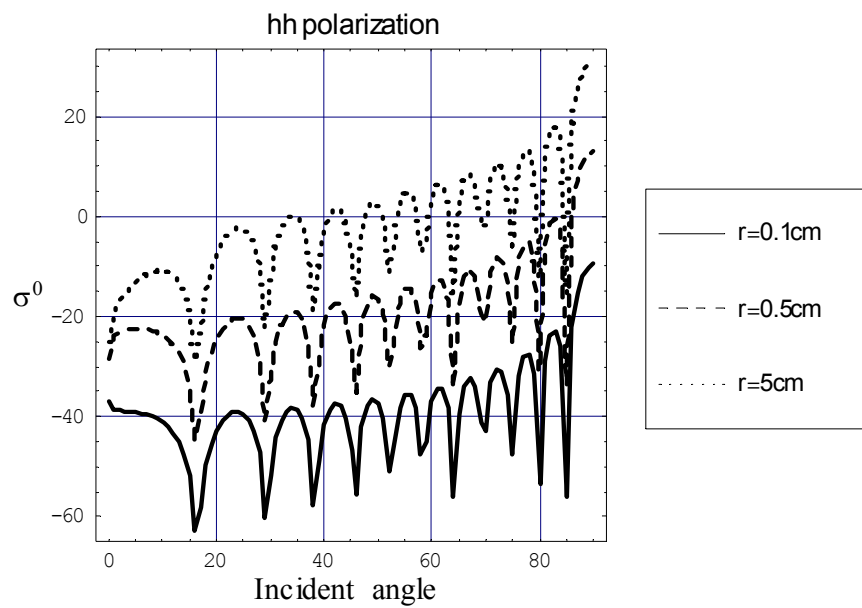


Figure 3.55 The HH scattering pattern of a cylinder versus the incidence angle for different radii of the cylinder ( $\epsilon_r = 29.6 - j7.1$ ).



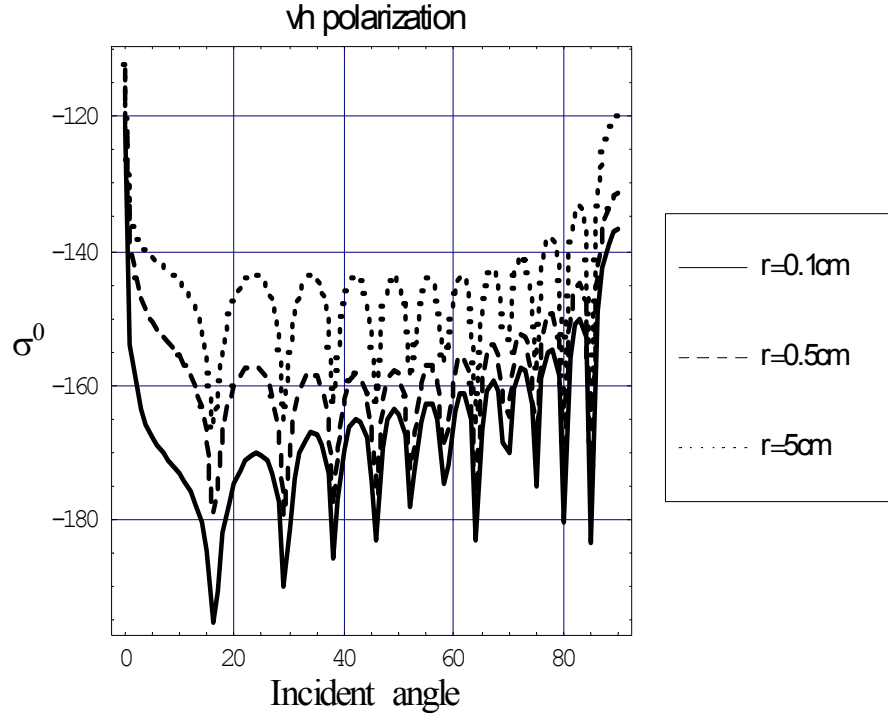


Figure 3.56 The VH scattering pattern of a cylinder versus the incidence angle for different radii of the cylinder ( $\epsilon_r = 29.6 - j7.1$ ).

### 3.6.3 Orientation Distribution Effects

In the previous section, we have demonstrated the behavior of the backscattering patterns of a cylinder versus the incidence angle for different radii and cylinder length. In this section, we will study the effects of orientation distribution on backscattering. In all cases, we let the orientation distribution be uniform in both the tilt angle,  $\beta$ , and the azimuth angle,  $\alpha$ . The ranges of these angles are indicated on the figures.

First, we show the backscattering properties of VV, HH and VH polarization over the incident angle in figures 3.57, 3.58 and 3.59 respectively for four different lengths of the cylinder. Results indicate that all oscillations are averaged out and all scattering curves are smooth. An increase in the length of the cylinder simply raises the level of backscattering. Next, we con-

sider similar backscattering properties for cylinders with different radii. Results are shown in figures 3.60 (VV), 3.61 (HH) and 3.62 (VH). Here again, all oscillations are averaged out and all backscattering curves are smooth. An increase in the radius generally raises the level of backscattering except the amount of change decreases with a decrease in the incident angle.

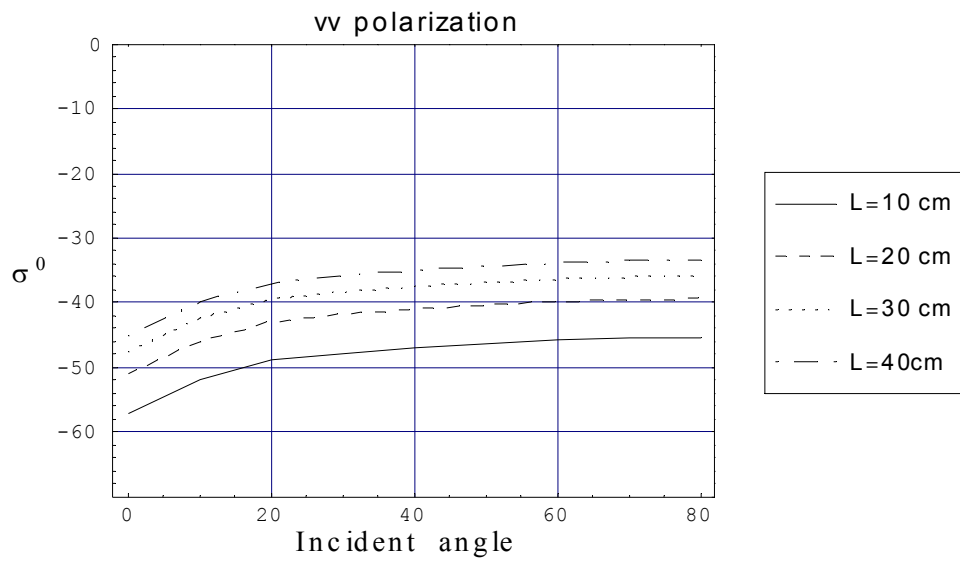


Figure 3.57 VV Backscattering Coefficient from half space of randomly oriented clinders versus the incidence angle with repective to different length of cylinders( $0^\circ < \alpha < 360^\circ$ ,  $0^\circ < \beta < 90^\circ$ ,  $\epsilon_r = 29.6 - j7.1$ ).

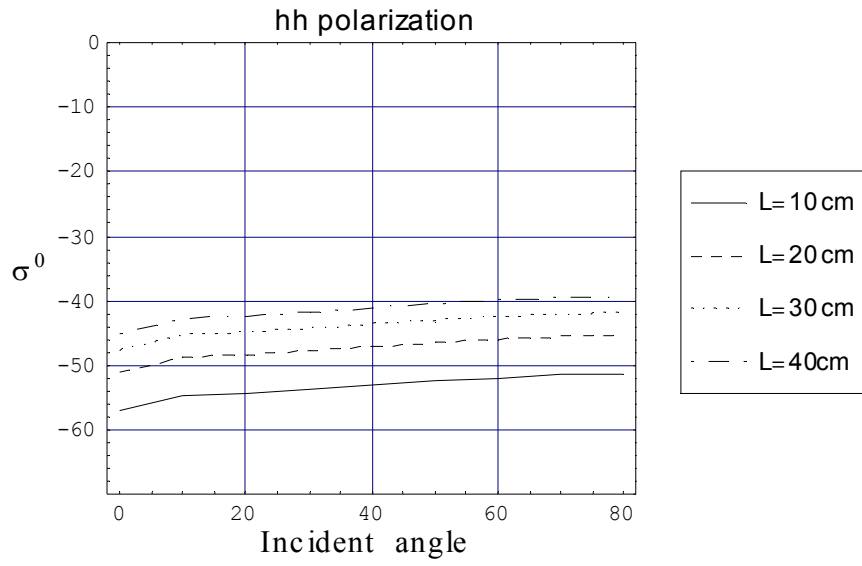


Figure 3.58 HH Backscattering Coefficient from half space of randomly oriented clinders versus the incidence angle with repective to different length of cylinders( $0^\circ < \alpha < 360^\circ$ ,  $0^\circ < \beta < 90^\circ$ ,  $\epsilon_r = 29.6 - j7.1$ ).

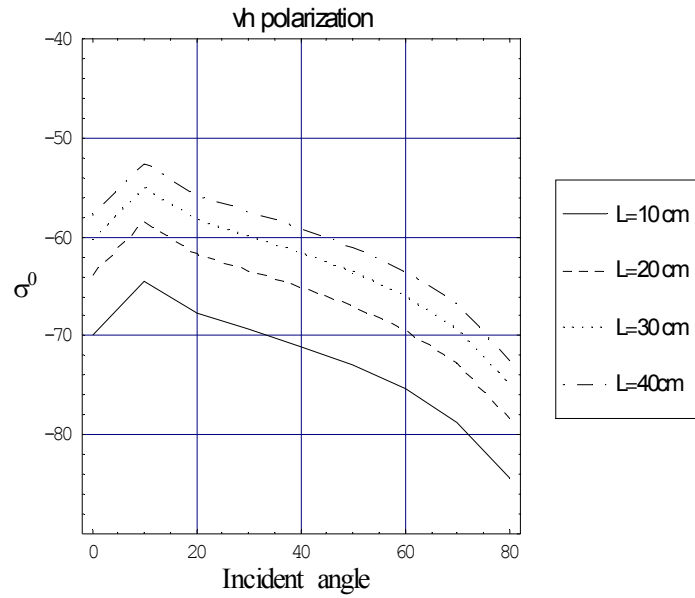


Figure 3.59 VH Backscattering Coefficient from half space of randomly oriented clinders versus the incident angle with repective to different length of cylinders( $0^\circ < \alpha < 360^\circ$ ,  $0^\circ < \beta < 90^\circ$ ,  $\epsilon_r = 29.6 - j7.1$  )

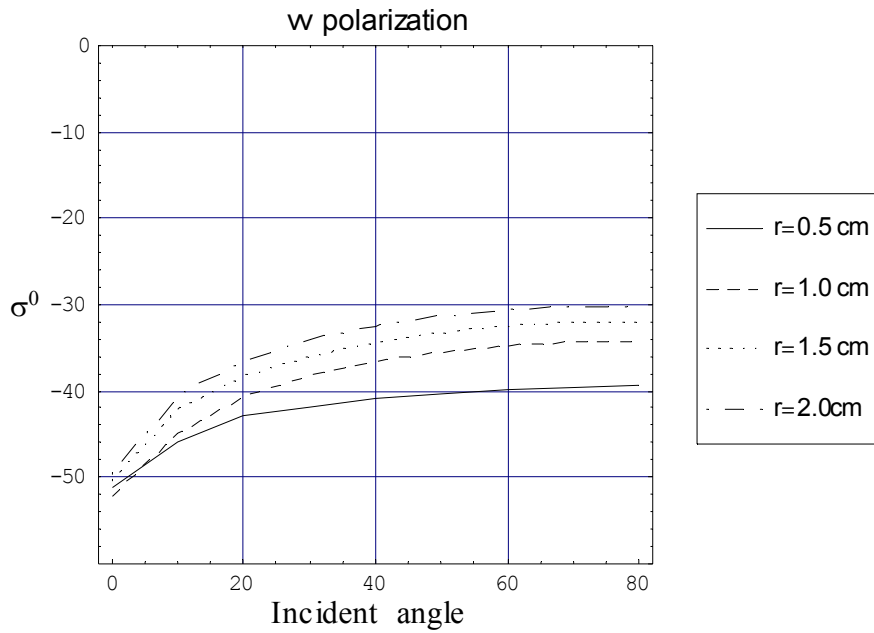


Figure 3.60 VV Backscattering Coefficient from half space of randomly oriented clinders versus the incidence angle with repective to different radius of cylinders( $0^\circ < \alpha < 360^\circ$ ,  $0^\circ < \beta < 90^\circ$ ,  $\epsilon_r = 29.6 - j7.1$ ).

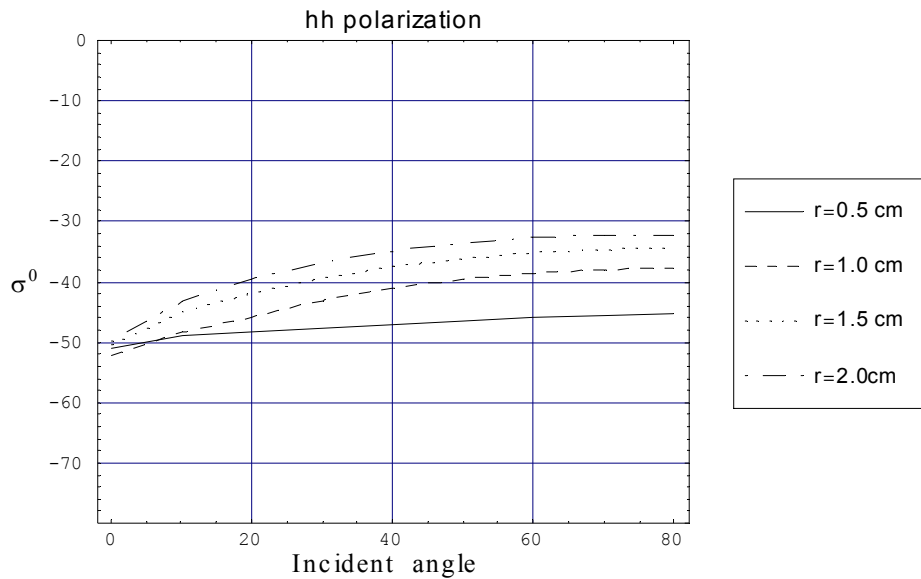


Figure 3.61 HH Backscattering Coefficient from half space of randomly oriented clinders versus the incidence angle with repective to different radius of cylinders( $0^\circ < \alpha < 360^\circ$ ,  $0^\circ < \beta < 90^\circ$ ,  $\epsilon_r = 29.6 - j7.1$ ).

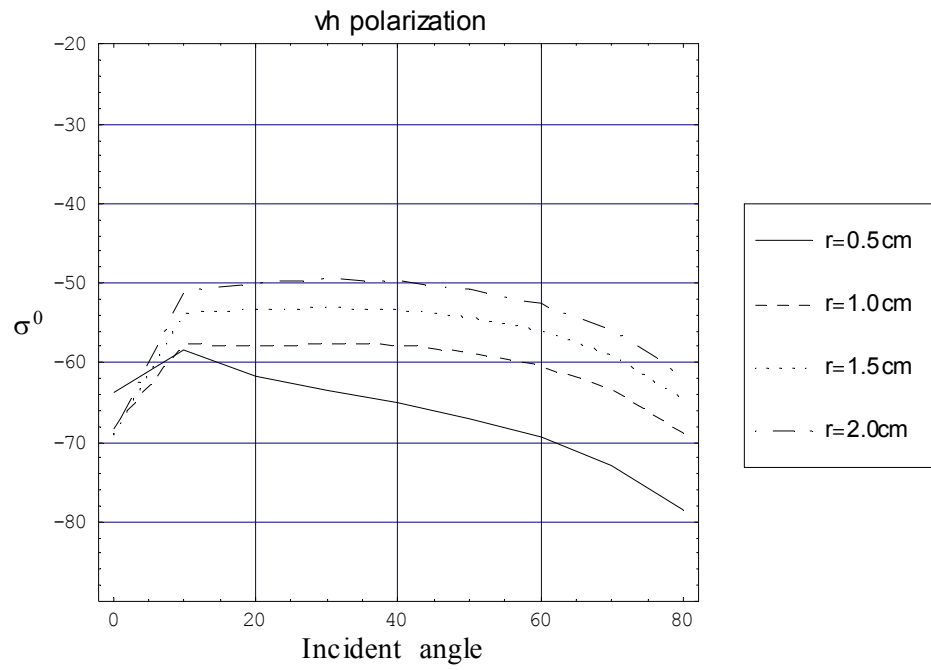


Figure 3.62 VH Backscattering Coefficient from half space of randomly oriented clinders versus the incidence angle with repective to different radius of cylinders( $0^\circ < \alpha < 360^\circ$ ,  $0^\circ < \beta < 90^\circ$ ,  $\epsilon_r = 29.6 - j7.1$ ).

## CHAPTER 4

### Scattering from Leafy Vegetation and Its Applications

#### 4.1 Introduction

The term “leafy vegetation” here means vegetations consisting mostly of leaves such as soybean, corn, and milo etc. or more generally it means that scattering from a vegetation cover can be attributed entirely to leaves. For example, in a deciduous forested area in the spring time, radar measurements are conducted at above 15 GHz away from the nadir direction. Here, we may encounter a situation where scattering from leaves is so dominating that scattering from branches, trunks and the land surface below can be safely ignored.

The leafy vegetation layer can be modeled as a collection of randomly oriented circular discs or needles over a half space and the backscattering coefficient from such a layer can be calculated using the radiative transfer method. In the following sections, the scattering model description for a leafy vegetation layer will be given and comparisons between model predictions and measurements are presented.

#### 4.2 Scattering Model Description for a Leafy Vegetation

Consider a collection of identical, randomly oriented, dielectric circular discs or needles lying in a half space illuminated by a plane wave,

$$\vec{E}_i(\vec{r}) = \hat{q}E_0e^{-jk\hat{i}\cdot\vec{r}} \quad (4.1)$$

where  $k$  is the background medium wave number,  $\hat{i}$  is the unit vector in the incident direction, and  $\hat{q}$  is the polarization unit vectors. The backscattering coefficient from the leafy vegetated

half space can be expressed as shown in (4.2) based on the first-order solution of the radiative transfer formulation.

$$\sigma_{pq} = 4\pi \cos\theta_i \cdot \frac{\langle |F_{pq}(-\hat{i}, \hat{i})|^2 \rangle}{\langle \sigma_p(-\hat{i}) \rangle + \langle \sigma_q(\hat{i}) \rangle} \quad (4.2)$$

where  $F_{pq}(\ )$  is the scattering amplitude for the scatterer given in Chapter 3, and  $\sigma_p(\hat{i})$  is the extinction cross section for the scatterer.

In (4.2) the ensemble average is taken over the scatterer orientation as

$$\langle |F_{pq}(-\hat{i}, \hat{i})|^2 \rangle = \int d\alpha \int d\beta p(\alpha) p(\beta) |F_{pq}(-\hat{i}, \hat{i})|^2 \quad (4.3)$$

where  $(\alpha, \beta)$  are the scatterer-orientation angles in the reference frame, and  $p(\alpha), p(\beta)$  are the probability distribution functions of the scatterer orientation.

The extinction cross section of the scatterer is given by

$$\sigma_p(i) = \frac{4\pi}{k} \text{Im}[F_{pp}(\hat{i}, \hat{i})] \quad (4.4)$$

where  $\text{Im}(\ )$  is the imaginary part operator. The extinction coefficient of the medium is

$$k_p = n_0 \sigma_p(i) \quad (4.5)$$

found by multiplying (4.4) by the number density,  $n_0$ .

### 4.3 Comparison with measurements

In order to verify the validity of the theoretical model given in the previous section for leafy vegetation, we carry out comparisons between model predictions and the measurements in this section. The sets of measurement data acquired by Dobson et al. (1977) from a soybean field are compared with the theoretical predictions at 1.1 GHz (L band), 4.25 GHz (C band)

and 8.6 GHz (X band). All the scatterers are assumed to be uniformly oriented in the azimuthal direction and the model parameters used for the soybean are listed in Table 4.1. from vegetation data record of experiments.

**Table 4.1. Soybean parameters used in the model for comparison with measurement**

Soybean	Parameters used in model
Thickness	1.0 m
Leaf dimension	a = 1.5 cm, c = 0.2 mm
Leaf volume fraction	0.3%
Leaf orientation	Uniformly oriented (0°, 90°)
Leaf dielectric constant	L band: 30.6-j1.7 C band: 29.1-j6.1 X band: 14.9-j4.9

Figure 4.1 and Figure 4.2 show the comparisons between the field data for soybean and the model predictions at 1.1 GHz for VV and VH polarization respectively. In Figure 1, the disagreement in the angular range, 0 - 20 degrees is due to scattering from the soil surface. This is expected for like polarization at such a low frequency. Similar disagreement does not occur for cross polarization, because surface depolarization is much weaker than the depolarization due to volume scattering.

Figure 4.3 and Figure 4.4 show the comparisons between model predictions and measurements of soybean for VV and VH polarizations respectively at 4.25 GHz. As expected there is much less penetration at this frequency. Thus, contributions from the soil surface is negligible except at normal incidence. Agreements for like polarization are generally good at all other angles. For cross polarization there is a rising trend in data for incidence angles larger than 20 degrees. The prediction from model is a decreasing trend with the incidence angle. Hence,



there is a clear disagreement in both level and trend in cross polarization. From a soybean field there is no known depolarization mechanism that can account for this difference in the angular trend.

Finally, we show comparisons between the model predications and measurements of soybean at 8.6 GHz in Figure 4.5. At this high frequency we expect no contributions from the ground surface. Thus, scattering is due purely to the soybean volume. In this case, the difference between VV and HH polarizations is negligible and there should be a slowly decreasing trend with the incidence angle. These observations are confirmed by the data in Figure 4.5.

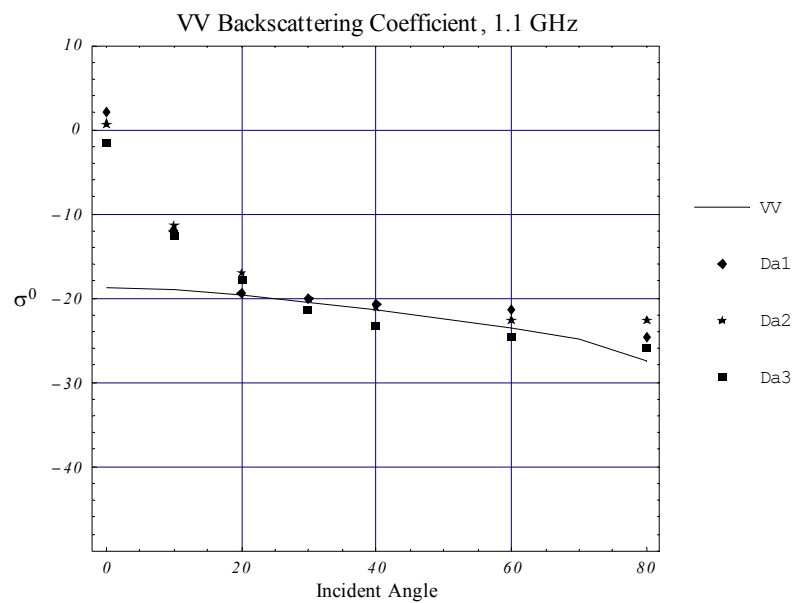


Figure 4.1 Comparison of model calculations for VV backscattering coefficient with measurements from soybean at 1.1 GHz.

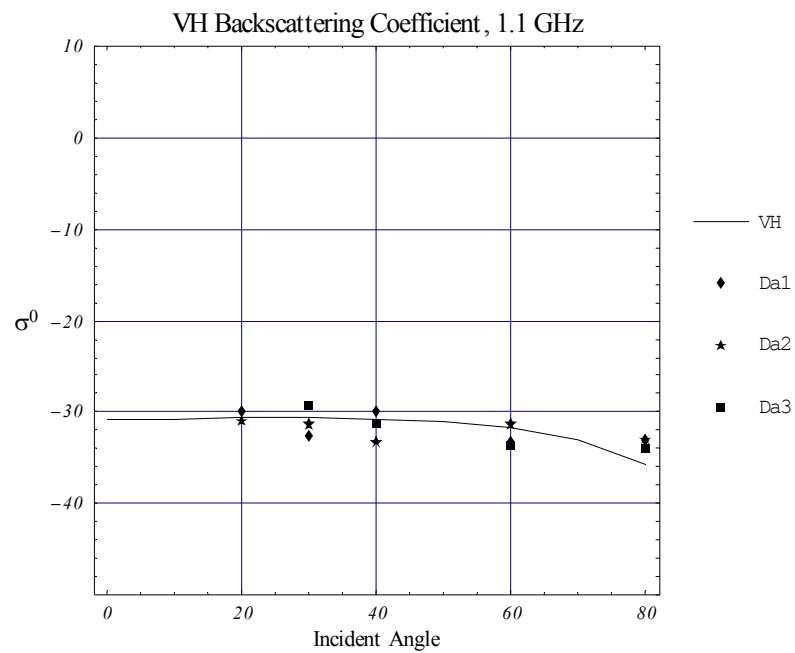


Figure 4.2 . Comparison of model calculations for VH backscattering coefficient with measurements from soybean at 1.1 GHz..

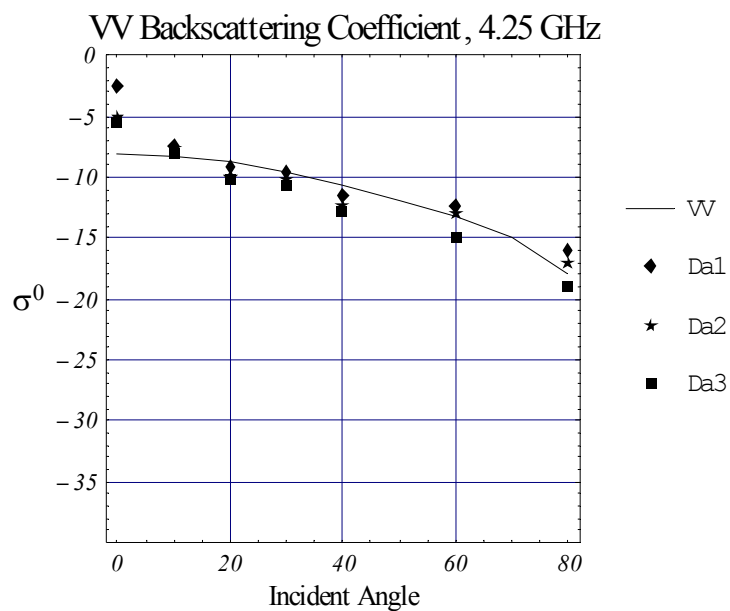


Figure 4.3 . Comparison of model calculations for VV backscattering coefficient with measurements from soybean at 4.25 GHz.

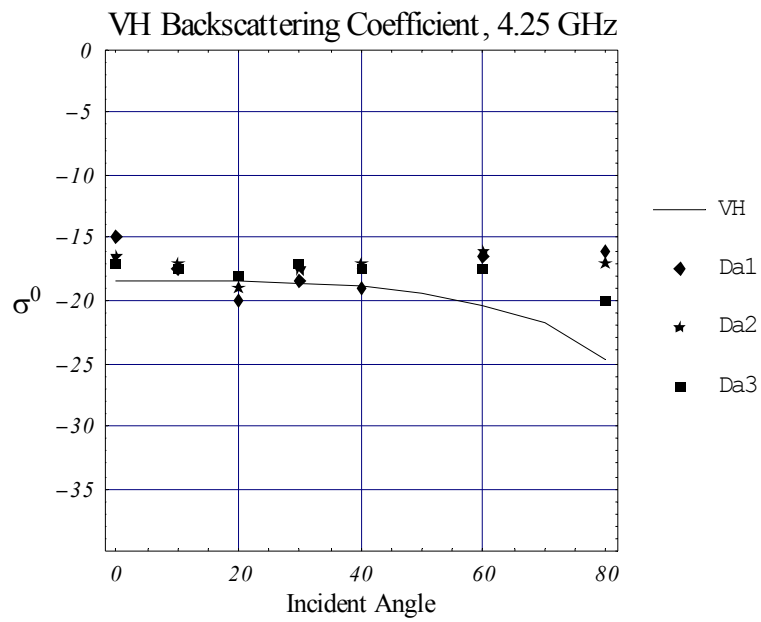


Figure 4.4 . Comparison of model calculations for VH backscattering coefficient with measurements from soybean at 4.25 GHz.

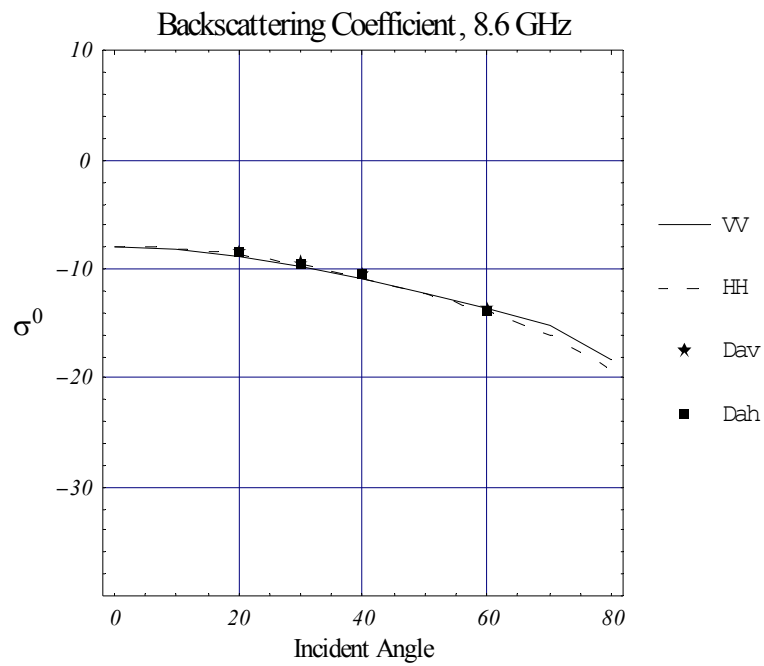


Figure 4.5 . Comparison of model calculations for VV and HH backscattering coefficients with measurements from soybean at 8.6 GHz.

# CHAPTER 5

## SCATTERING FROM A FORESTED AREA

### 5.1 Introduction

We shall use a two-layer model to simulate a forested area: a crown layer and a trunk layer as illustrated in Figure 5.1. Scattering from the soil surface below the trunk layer is modeled using the IEM surface scattering model for a randomly rough surface [7]. The development of such a scattering model is given in the next section. This is followed by Section 5.3 on theoretical studies of the scattering model and then Section 5.4 on comparisons of the scattering model with measurements.

### 5.2 Description of Forest Scattering Model

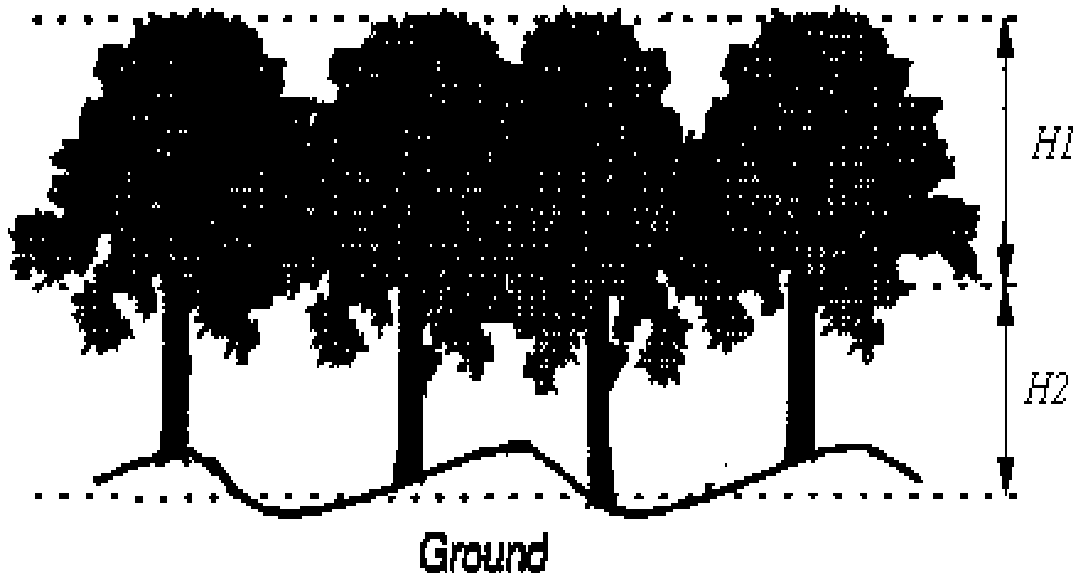


Figure 5.1 Geometry of a forested area.

For the geometry of the canopy shown in Figure 5.1, the canopy is represented by a two-layer medium above a rough surface. The top layer is consisted of tree components: leaves,

branches and twigs with a layer height of  $H_1$ . The bottom layer contains only vertically oriented trunks with an average height of  $H_2$ . Each scatterer is described by having a permittivity, a size distribution, an orientation distribution and a number density.

Consider a plane wave incident along  $\hat{i}(\pi - \theta_i, \phi_i)$  direction with an electric field polarized in the  $\hat{q}$  direction,

$$\overline{E}_i(\vec{r}) = \hat{q} E_0 e^{-jk(\hat{i} \cdot \vec{r})} \quad (5.1)$$

where  $k = (2\pi)/\lambda$  is the wave number and  $\hat{q} = \hat{v}_i$  or  $\hat{h}_i$  is the polarization unit vector defined as follows

$$\hat{i} = \sin \theta_i (x \cos \phi_i + y \sin \phi_i) - \hat{z} \cos \theta_i \quad (5.2)$$

$$\hat{h}_i = \frac{\hat{z} \times \hat{i}}{|\hat{z} \times \hat{i}|} = y \cos \phi_i - x \sin \phi_i \quad (5.3)$$

$$\hat{v}_i = \hat{h}_i \times \hat{i} = -\cos \theta_i (x \cos \phi_i + y \sin \phi_i) - \hat{z} \sin \theta_i \quad (5.4)$$

Based upon an iterative solution of the radiative transfer equation with respect to the albedo of the volume scattering medium, the bistatic scattering coefficient for the scattering layer can be written as

$$\sigma_{pq} = \sum_{v=0}^V \sigma_{pq}^v \quad (5.5)$$

where  $v$  is the order of the iterative solution of the radiative transfer equation. The explicit form of each order is given in the sections to follow.

### 5.2.1 The Zeroth-Order Solution

The zeroth-order solution of the radiative transfer equation (shown in Figure 5.2) is independent of the albedo of the scattering layer. In this case, it involves only the scattering from the soil surface attenuated as it passes through the vegetation layer on its way down to the soil surface and on its way back to the receiving antenna.

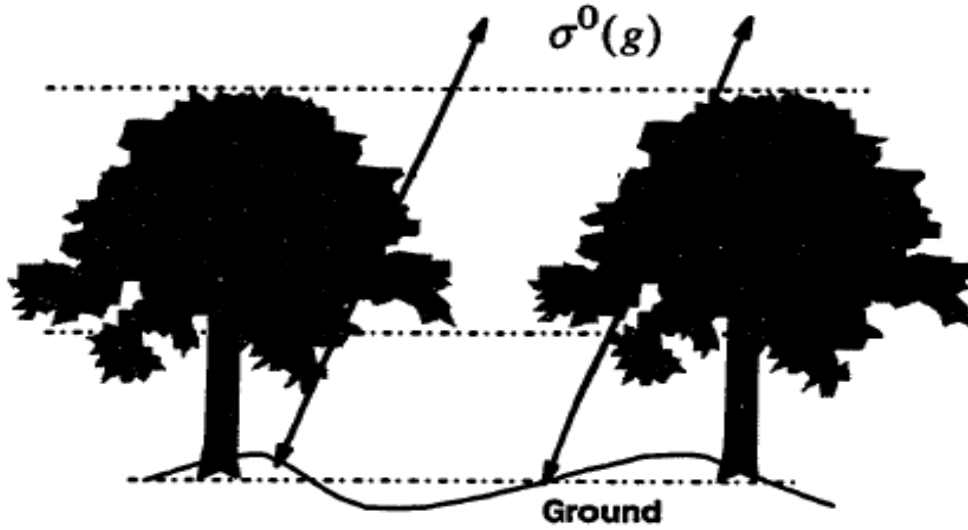


Figure 5.2 Scattering Mechanisms of the Zeroth-Order Solution

The zeroth order scattering coefficient can be written as

$$\sigma_{pq}^0 = L_{cp}(\theta_s)L_{tp}(\theta_s)\sigma_{pq}^s(\theta_s, \phi_s; \pi - \theta_i, \phi_i)L_{tq}(\theta_i)L_{cq}(\theta_i) \quad (5.6)$$

where  $\theta_s, \phi_s$  is the angular pair denoting the scattering direction, and  $\sigma_{pq}^s(\theta_s, \phi_s; \pi - \theta_i, \phi_i)$  is the  $pq$ -element of the  $4 \times 4$  bistatic scattering coefficient matrix of the surface given in [7] repeated in Appendix B.  $L_{cq}(\theta_i)$  and  $L_{tq}(\theta_i)$  are the  $q$  polarized crown and trunk attenuation factors in the incident direction defined as

$$L_{jq}(\theta_i) = \exp[-k_{jq}(\theta_i)H_j \sec \theta_i], \quad j = c, t \quad (5.7)$$

where  $k_{jq}(\theta_i)$ ,  $j = c, t$  are the crown and trunk layer extinction coefficients respectively [38,39] in the incident direction.  $H_j$ ,  $j = c, t$  are the heights of the crown and trunk layers. Similarly,  $L_{cp}(\theta_s)$  and  $L_{tp}(\theta_s)$  are the  $p$  polarized crown and trunk attenuation factors in the scattering direction. The extinction coefficient of the crown layer containing  $N_c$  types of scatterers can be expressed as

$$k_{cp}(\theta_i) = \sum_{m=1}^{N_c} n_{cm} \langle \sigma_{cmp}(\theta_i) \rangle \quad (5.8)$$

where  $n_{cm}$  is the group number density, and  $\sigma_{cmp}(\theta_i)$  is the extinction cross section of the scatterer in the  $m^{th}$  group. The ensemble average in (5.8) is taken over the orientation distribution  $P_{cm}(\alpha, \beta)$  of the scatterer in the group:

$$\langle k_{cmp}(\theta_i) \rangle = \frac{1}{2\pi} \int d\beta \int d\alpha P_{cm}(\alpha, \beta) k_{cmp}(\theta_i) \quad (5.9)$$

The extinction coefficient of the trunk layer can be defined in a analogous way, although the number of groups may be considerably smaller.

$$k_{tp}(\theta_i) = \sum_{m=1}^{N_t} n_{tm} \langle \sigma_{tmp}(\theta_i) \rangle \quad (5.10)$$

where  $N_t$  is the group number density and  $\sigma_{tmp}(\theta_i)$  is the extinction cross section of a scatterer in the  $m^{th}$  group in the trunk layer. The ensemble average is defined similar to that of (5.9) but with the trunk orientation distribution function.

### 5.2.2 The First-Order Solution

Figure 5.3 shows the two possible forms of the first-order scattering paths: direct volume scattering and volume-ground interactions. Accordingly, the first-order solution of the radiative transfer equation leads to a bistatic scattering coefficient in the following form

$$\sigma_{pq}^1 = \sigma_{pq}(c) + \sigma_{pq}(c \leftrightarrow g) + \sigma_{pq}(t) + \sigma_{pq}(t \leftrightarrow g) \quad (5.11)$$

where  $\sigma_{pq}(c)$  accounts for crown scattering;  $\sigma_{pq}(c \leftrightarrow g)$  for the crown-ground interaction;  $\sigma_{pq}(t)$  for trunk scattering, and  $\sigma_{pq}(t \leftrightarrow g)$  for the trunk-ground interaction.

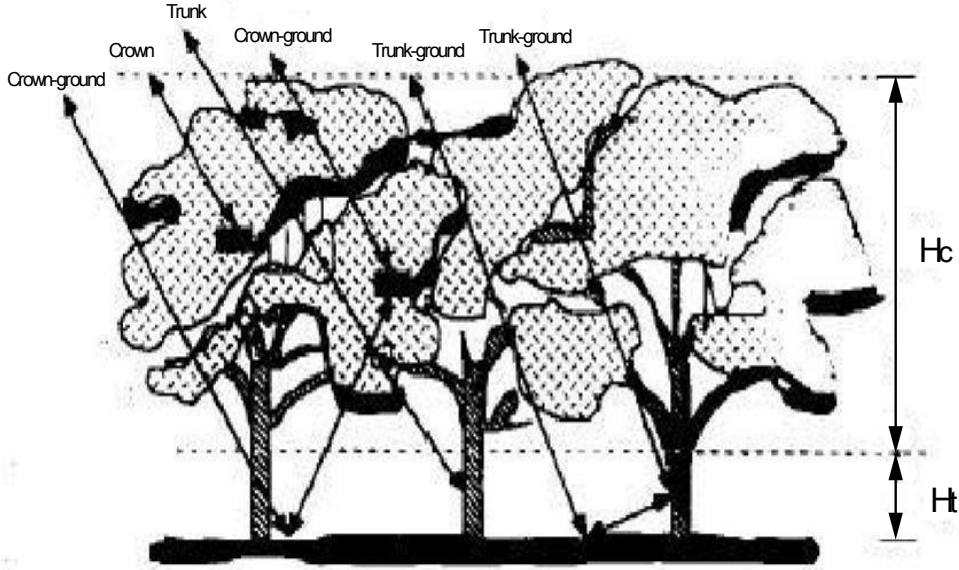


Figure 5.3 Scattering Mechanisms of the First-Order Solution

The scattering coefficient due to volume scattering from the crown layer can be expressed as

$$\sigma_{pq}(c) = 4\pi Q_{cpq}(\theta_s, \phi_s; \pi - \theta_i, \phi_i) \cdot \left\{ \frac{1 - L_{cp}(\theta_s)L_{cq}(\theta_i)}{k_{cp}(\theta_s)\sec\theta_s + k_{cq}(\theta_i)\sec\theta_i} \right\} \quad (5.12)$$

$$Q_{cpq}(\theta_s, \phi_s; \pi - \theta_i, \phi_i) = \sum_{m=1}^{IV_c} n_{cm} \langle |F_{cmpq}(\hat{s}, \hat{i})|^2 \rangle \quad (5.13)$$

where  $F_{cmpq}(\hat{s}, \hat{i})$  is the element of the scattering amplitude matrix for a scatterer within the  $m^{th}$  group. The ensemble average is taken over its group orientation distribution similar to



(5.9). The quantity  $Q_{cpq}(\theta_s, \phi_s; \pi - \theta_i, \phi_i)$  represents scattering from a unit volume within the crown region.

From (5.13), the crown scattering includes  $N_c$  types of scatterers and they are attenuated by the leaves, the stems and the branches.

The Crown-Ground interaction scattering coefficient is illustrated in Figure 5.3. It consists of two terms as

$$\sigma_{pq}(c \leftrightarrow g) = \sigma_{pq}(c \rightarrow g) + \sigma_{pq}(g \rightarrow c) \quad (5.14)$$

where the first item represents scattering from the crown followed by scattering from the ground and the second term represents scattering from the ground followed by scattering from the crown.

$$\sigma_{pq}(c \rightarrow g) = L_{cp}(\theta_s) L_{tp}(\theta_s) \int_0^{2\pi} d\phi_t \int_0^{\frac{\pi}{2}} \sin \theta_t d\theta_t \sum_{u=v, h} L_{tu}(\theta_t) \quad (5.15)$$

$$\cdot \sigma_{pu}^s(\theta_s, \phi_s; \theta_i, \phi_i) Q_{cuq}(\pi - \theta_i, \phi_i; \pi - \theta_s, \phi_s) \cdot \cos \theta_i \left( \frac{L_{cu}(\theta_t) - L_{cq}(\theta_i)}{k_{cq}(\theta_t) \cos \theta_t - k_{cu}(\theta_i) \cos \theta_i} \right)$$

$$\sigma_{pq}(g \rightarrow c) = L_{cq}(\theta_i) L_{tq}(\theta_i) \int_0^{2\pi} d\phi_t \int_0^{\frac{\pi}{2}} \sin \theta_t d\theta_t \sum_{u=v, h} L_{tu}(\theta_t) \quad (5.16)$$

$$\cdot \sigma_{uq}^s(\theta_i, \phi_i; \pi - \theta_s, \phi_s) Q_{cpu}(\theta_s, \phi_s; \theta_i, \phi_i) \cdot \cos \theta_i \left( \frac{L_{cp}(\theta_s) - L_{cu}(\theta_t)}{k_{cu}(\theta_t) \cos \theta_t - k_{cp}(\theta_s) \cos \theta_i} \right)$$

The bistatic scattering coefficient of the trunk can be written as

$$\sigma_{pq}(t) = 4\pi L_{cp}(\theta_s) L_{cq}(\theta_i) Q_{tpq}(\theta_s, \phi_s; \pi - \theta_i, \phi_i) \left\{ \frac{1 - L_{tp}(\theta_s) L_{tq}(\theta_i)}{k_{tp}(\theta_s) \sec \theta_s + k_{tq}(\theta_i) \sec \theta_i} \right\} \quad (5.17)$$

$$Q_{tpq}(\theta_s, \phi_s; \pi - \theta_i, \phi_i) = \sum_{m=1}^{N_t} n_m \langle |F_{mpq}(\hat{s}, \hat{i})|^2 \rangle \quad (5.18)$$

where  $F_{mpq}(\hat{s}, \hat{i})$  is the element of the scattering amplitude matrix for the  $m^{th}$  trunk group. The scattered signal from the trunk layer in (5.18) is modified by the attenuation factor  $L_{cp}(\theta_s)L_{cq}(\theta_i)$  because it must pass through the crown layer in both upward and downward directions.

The trunk-ground interaction shown as Figure 5.3 can be expressed as

$$\sigma_{pq}(t \leftrightarrow g) = \sigma_{pq}(t \rightarrow g) + \sigma_{pq}(g \rightarrow t) \quad (5.19)$$

The first term in (5.19) represents scattering from the trunk followed by scattering from the ground and the second term represents scattering from the ground followed by scattering from the trunk.

$$\begin{aligned} \sigma_{pq}(t \rightarrow g) = & L_{cp}(\theta_s)L_{cq}(\theta_i)L_{tp}(\theta_s) \int_0^{2\pi} d\phi_t \int_0^{\frac{\pi}{2}} \sin\theta_t d\theta_t \\ & \sum_{u=v,h} \sigma_{pu}^s(\theta_s, \phi_s; \theta_t, \phi_t) \cdot Q_{tuq}^s(\pi - \theta_t, \phi_t; \pi - \theta_i, \phi_i) \cdot \cos\theta_i \left[ \frac{L_{tu}(\theta_t) - L_{tq}(\theta_i)}{k_{tq}(\theta_i)\cos\theta_t - k_{tu}(\theta_t)\cos\theta_i} \right] \end{aligned} \quad (5.20)$$

$$\begin{aligned} \sigma_{pq}(g \rightarrow t) = & L_{cp}(\theta_s)L_{cq}(\theta_i)L_{tp}(\theta_i) \int_0^{2\pi} d\phi_t \int_0^{\frac{\pi}{2}} \sin\theta_t d\theta_t \\ & \sum_{u=v,h} \sigma_{uq}^s(\theta_t, \phi_t; \pi - \theta_i, \phi_i) \cdot Q_{tpu}^s(\theta_s, \phi_s; \theta_t, \phi_t) \cdot \cos\theta_i \left[ \frac{L_{tp}(\theta_s) - L_{tq}(\theta_t)}{k_{tu}(\theta_t)\cos\theta_s - k_{tp}(\theta_s)\cos\theta_t} \right] \end{aligned} \quad (5.21)$$

The quantities,  $Q_{ipu}^s(\theta_s, \phi_s; \theta_t, \phi_t)$  and  $Q_{tuq}^s(\pi - \theta_t, \phi_t; \pi - \theta_i, \phi_i)$ , are the scattered intensity per unit volume in the trunk layer.

### 5.2.3 The Second-Order Solution

The second-order solution [7] of the radiative transfer equation within the crown layer is obtained by using the first-order intensity as an exciting source. This solution contains many terms, but most of these terms are small compared to the first-order solution. Only two dominant terms shown in Figure 5.4 and Figure 5.5 due to scattering within the crown layer are kept.

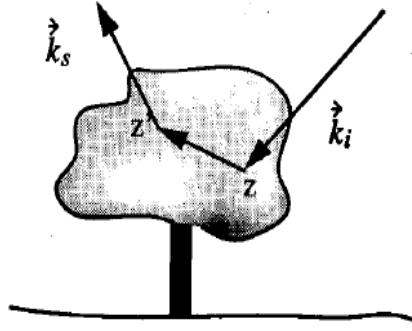


Figure 5.4 Crown-Crown interaction:  $\sigma_{pq}(u, u, d)$ . The incident signal is scattered upward twice before propagating towards the receiving antenna.

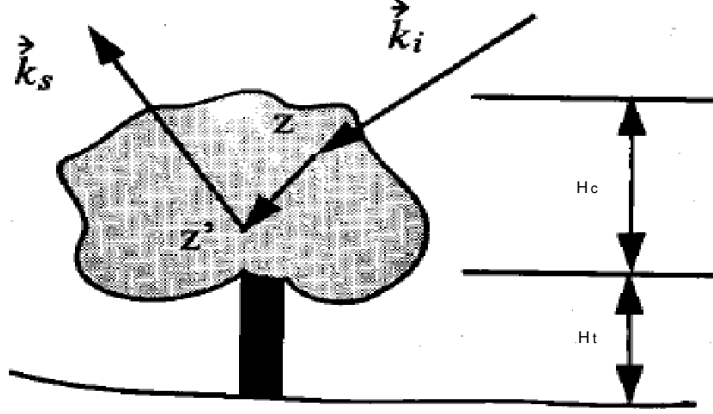


Figure 5.5 Crown-Crown interaction:  $\sigma_{pq}(u, d, d)$ . The incident signal is scattered downward first and then upwards towards the receiving antenna.

$$\sigma_{pq}(u, u, d) = 4\pi \int_0^{2\pi} d\phi \int_0^{\frac{\pi}{2}} \sin\theta d\theta \quad (5.22)$$

$$\left\{ \sum_{u=v,h} \frac{\sec\theta_s Q_{cpu}^s(\theta_s, \phi_s; \theta, \phi) Q_{cuq}^s(\theta, \phi; \pi - \theta_i, \phi_i)}{k_{cq}(\theta_i) \sec\theta_i + k_{cu}(\theta_s) \sec\theta} \right. \\ \left[ \frac{1 - L_{cp}(\theta_s) L_{cq}(\theta_i)}{k_{cq}(\theta_i) \sec\theta_i + k_{cp}(\theta_s) \sec\theta_s} + \frac{L_{cq}(\theta_i) [L_{cq}(\theta) - L_{cp}(\theta_s)]}{k_{cu}(\theta) \sec\theta - k_{cp}(\theta) \sec\theta_s} \right. \\ \left. + 2Re \left( \frac{\sec\theta_s Q_{1p3}^s(\theta_s, \phi_s; \theta, \phi) Q_{13q}^s(\theta, \phi; \pi - \theta_i, \phi_i)}{k_{cq}(\theta_i) \sec\theta_i + k_{13}(\theta) \sec\theta} \right) \right. \\ \left. \left. \left[ \frac{1 - L_{cp}(\theta_s) L_{cq}(\theta_i)}{k_{cq}(\theta_i) \sec\theta_i + k_{cp}(\theta_s) \sec\theta_s} + \frac{L_{cq}(\theta_i) [L_{13}(\theta) - L_{cp}(\theta_s)]}{k_{13}(\theta) \sec\theta - k_{cp}(\theta_s) \sec\theta_s} \right] \right] \right\}$$

$$\sigma_{pq}(u, d, d) = 4\pi \int_0^{2\pi} \int_0^{\frac{\pi}{2}} \sin\theta d\theta \quad (5.23)$$

$$\left\{ \sum_{u=v, h} \frac{\sec\theta_s Q_{cpu}^s(\theta_s, \phi_s; \pi - \theta, \phi) Q_{cuq}^s(\pi - \theta, \phi, \pi - \theta_i, \phi_i)}{k_{cp}(\theta_s) \sec\theta_s + k_{cu}(\theta) \sec\theta} \right. \\ \left[ \frac{1 - L_{cp}(\theta_s) L_{cq}(\theta_i)}{k_{cq}(\theta_i) \sec(\theta_i + k_{cp}(\theta_s) \sec\theta_s)} + \frac{L_{cp}(\theta_s) [L_{cu}(\theta) - L_{cq}(\theta_i)]}{k_{cu}(\theta) \sec\theta - k_{cq}(\theta_i) \sec\theta_i} \right] \\ + 2Re \left( \frac{\sec\theta_s Q_{1p3}^s(\theta_s, \phi_s; \pi - \theta, \phi) Q_{13q}^s(\pi - \theta, \phi; \pi - \theta_i, \phi_i)}{k_{cp}(\theta_s) \sec\theta_i + k_{13}(\theta) \sec\theta} \right. \\ \left. \left[ \frac{1 - L_{cp}(\theta_s) L_{cq}(\theta_i)}{k_{cq}(\theta_i) \sec\theta_i + k_{cp}(\theta_s) \sec\theta_s} + \frac{L_{cp}(\theta_s) [L_{13}(\theta) - L_{cq}(\theta_i)]}{k_{13}(\theta) \sec\theta - k_{cq}(\theta_i) \sec\theta_i} \right] \right) \Bigg\}$$

where  $Q_{cuq}^s(\theta_p, \phi_t; \pi - \theta_i, \phi_i)$  and  $Q_{c3q}^s(\theta_p, \phi_t; \pi - \theta_i, \phi_i)$  are scattering intensities which represent scattering by a unit volume from  $\hat{i}(\pi - \theta_i, \phi_i)$  to direction  $\hat{i}(\theta_p, \phi_t)$ ,  $Q_{cpu}^s(\theta_s, \phi_s; \theta_p, \phi_t)$  and  $Q_{cp3}^s(\theta_s, \phi_s; \theta_p, \phi_t)$  are scattering intensities which represent scattering from  $\hat{i}(\theta_p, \phi_t)$  to the observation direction  $\hat{s}(\theta_s, \phi_s)$ . The contents of  $Q_{cu3}^s$  and  $Q_{13u}^s$ , with  $u = v, h$  and the subscript 3 stands for the third Stokes, are as follows:

$$Q_{1v3}^s(\theta_s, \phi_s; \theta, \phi) = \sum_{j=1}^{N_c} n_j \langle F_{jvv}(\vec{k}_s, \vec{k}_i) F_{jvh}^*(\vec{k}_s, \vec{k}_i) \rangle \quad (5.24)$$

$$Q_{13v}^s(\theta_s, \phi_s; \theta, \phi) = \sum_{j=1}^{N_c} n_j \langle F_{jvv}(\vec{k}_s, \vec{k}_i) F_{jhv}^*(\vec{k}_s, \vec{k}_i) \rangle \quad (5.25)$$

$$Q_{13h}^s(\theta_s, \phi_s; \theta, \phi) = \sum_{j=1}^{N_c} n_j \langle F_{jvh}(\vec{k}_s, \vec{k}_i) F_{jhh}^*(\vec{k}_s, \vec{k}_i) \rangle \quad (5.26)$$

$$Q_{1h3}^s(\theta_s, \phi_s; \theta, \phi) = \sum_{j=1}^{N_c} n_j \langle F_{j_{hv}}(\vec{k}_s, \vec{k}_i) F_{j_{hh}}^*(\vec{k}_s, \vec{k}_i) \rangle \quad (5.27)$$

$$k_{13}(\theta) = \frac{1}{2}[k_{cv}(\theta) + k_{ch}(\theta)] + \frac{2\pi j}{k} Re \left[ \sum_{m=1}^{N_c} n_m \langle F_{m_{vv}}(\vec{k}_i, \vec{k}_i) - F_{m_{hh}}(\vec{k}_i, \vec{k}_i) \rangle \right] \quad (5.28)$$

$$L_{13}(\theta) = \exp[-k_{13}(\theta)H_c \sec \theta]$$

### 5.2.4 Theoretical Study of Forest Model

A frequency study of two forest components is carried out to demonstrate the importance of these components at different frequency ranges. Here the needles (radius is 0.1cm and length is 1cm) and branches (radius is 0.2cm and length is 30cm) have been chosen to conduct the frequency study. The result of the frequency study is displayed in Figure 5.6 where comparison of scattering between randomly oriented needles and branches are shown for VV and HH polarizations. It is found that, at low frequency, backscattering from branches is dominating over that of the leaves up to about 7.5 GHz. When frequency increases beyond 12.5 GHz it is the backscattering from the leaves that dominates over that of the branches. This means that in a forested environment, generally, it requires more than one frequency to explore the internal structure of the forest.

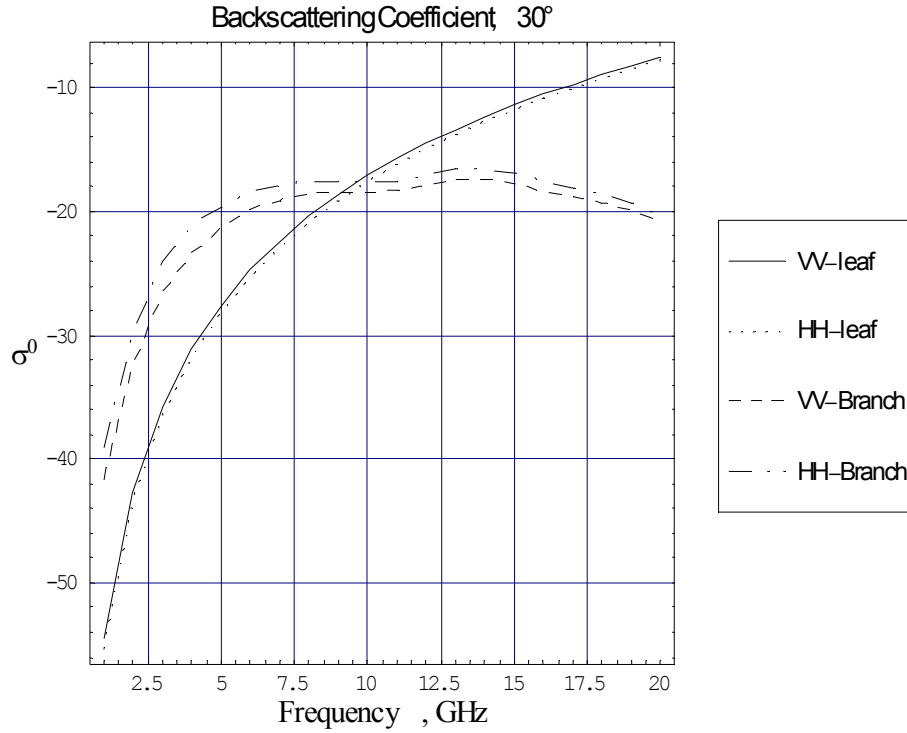


Figure 5.6 Behavior of Backscattering Coefficient of different scatterers (needle, cylinder) versus to variation of frequency.

## 5.3 Comparison with Measurements

### 5.3.1 Introduction

In the previous sections, a multilayer scattering model for a forested area has been described in detail based on the radiative transfer theory. In order to verify the validity of the theoretical model, two sets of data have been chosen for comparison. For the deciduous forest, we choose data sets acquired from a Walnut Orchard [41]; for the coniferous forest, we shall study the data from Japanese Cypress [22].

### 5.3.2 Walnut tree

The walnut canopy and its parameters [41] are described as follows:

The canopy consists of 6-year-old black walnut trees with an average height of  $4.8m$ . Their geometry data were collected in two parts. Skeleton geometry measurement is claimed as measurements involving branches with diameter greater than 4 cm and the rest is termed as the higher order measurements. A group of 16 walnuts was chosen for the canopy geometry and ground truth measurements. The heights, width across the row and the length down the row were measured.

In this study, a two-layer model (crown layer and trunk layer) is constructed to model the structure of a walnut orchard and the scattering from the ground surface is modeled by the IEM model [7]. The parameters of the walnut crown layer used for model predictions are listed in Table 5.1. where the crown layer consists of leaf, branch group 1(stems), branch group 2, branch group 3, and branch group 4



**Table 5.1. Parameters of the Crown Layer for Modeling a Walnut Orchard**

Walnut Crown	Parameter
Height	3.0m
Parameters of Leaf	
Density/ $m^3$	250
Dimension	a = 3.6cm, c = 0.1mm
Number of leaflet in a group	11
Dielectric Constant	L band: 19.58-j 5.54 X band: 14.9-j4.9
Parameters of Branch 1(stem)	
Density/ $m^3$	250
Dimension	r = 0.10cm; L=18cm
Dielectric Constant	L band: 27.3-j8.4 X band: 20.0-j9.7
Parameters of Branch 2	
Density/ $m^3$	11.4
Dimension	r=1.28cm; L=14cm
Dielectric Constant	L band: 27.3-j8.4 X band: 20.0-j9.7
Parameters of Branch 3	
Density/ $m^3$	0.43
Dimension	r=2.60; L=32cm
Dielectric Constant	L band: 27.3-j8.4 X band: 20.0-j9.7
Parameters of Branch4	
Density/ $m^3$	0.33
Dimension	r=5.00cm; L=58cm
Dielectric Constant	L band: 27.3-j8.4 X band: 20.0-j9.7

The parameters for the trunk layer and rough surface are displayed in Table 5.2..

**Table 5.2. Parameters of the Trunk Layer and Ground Surface for Modeling Walnut Orchard**

Walnut Trunk	Parameter
Height	1.7m
Density/ $m^3$	0.14
Dimension	r=9.0cm; L=76cm
Dielectric Constant	L band: 27.3-j8.4 X band: 20.0-j9.7
Ground Surface	
Gaussian correlation function	$\sigma = 0.021m$ ; $correL = 0.25m$
Dielectric Constant	L band: 5.0-j0.7 X band: 5.0-j0.7

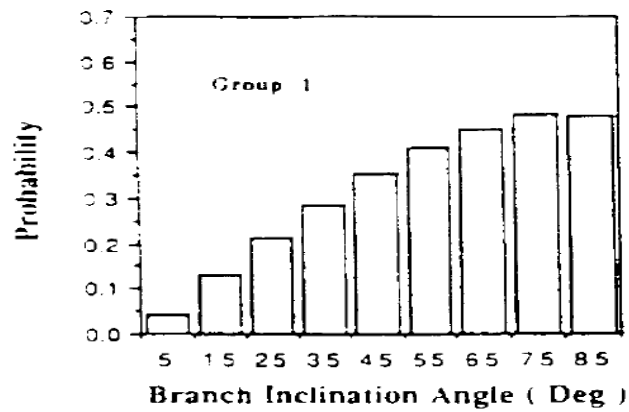


Figure 5.7 The probability distribution of the inclination angles for branch 1

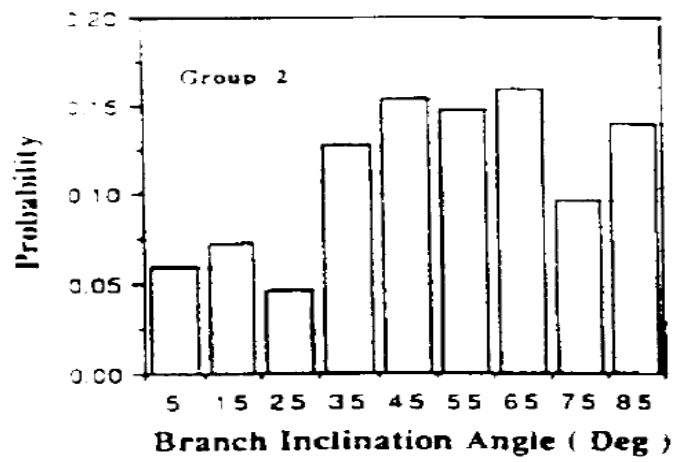


Figure 5.8 The probability distributions of the inclination angles for branch 2

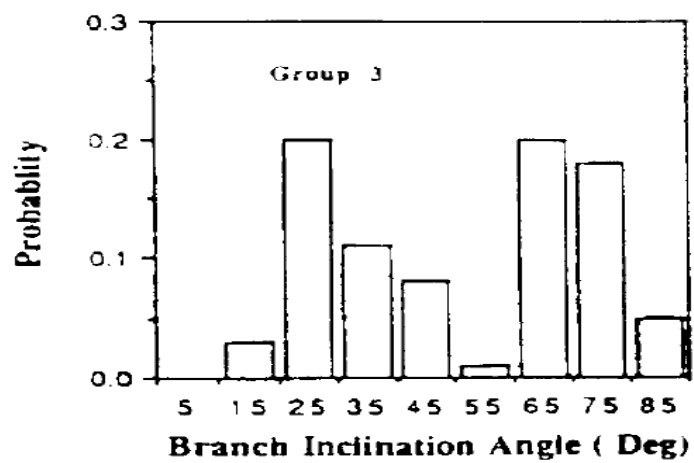


Figure 5.9 The probability distributions of the inclination angles for branch 3

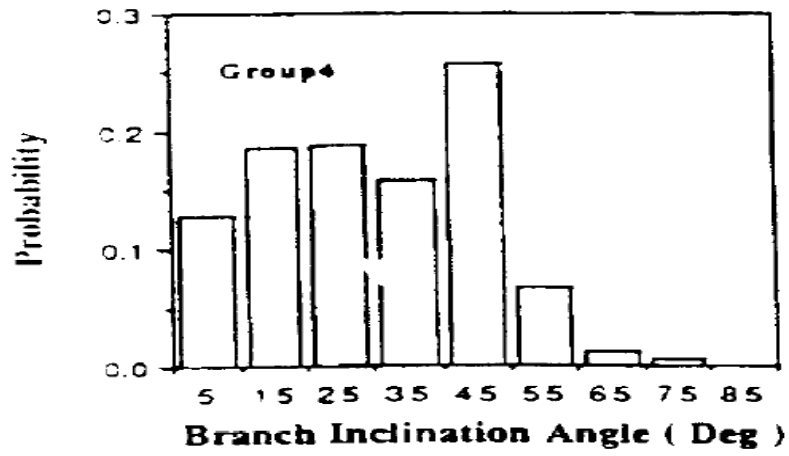


Figure 5.10 The probability distributions of the inclination angles for branch 4

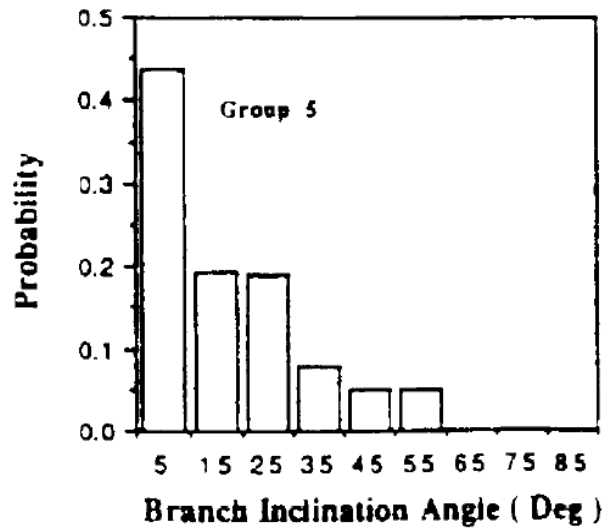


Figure 5.11 The probability distributions of the inclination angles for trunk

The probability distribution of the inclination angles for different groups of branch and trunk are given in the Figure 5.7, 5.8, 5.9, 5.10, and 5.11 [6]. The leaf has a probability distribution function equal to  $\sin\beta$  ( $0^\circ < \beta < 90^\circ$ ) over the inclination angle.

In Figure 5.16, we show comparisons between our model predications and measurements from walnut trees for VV, HH and VH polarizations at 9.6GHz (X-band). In the model predi-

cations, we use a group of leaves to model the coherent effect between leaflets in a compound leaf, since walnut trees possess compound leaves. The specific choices of leaf parameters are indicated in the figure legend. Very good agreements are obtained in both level and angular trends. In Figure 5.17, we show comparisons of the VV data with model predictions by investigators from Michigan [1~3] and Malaysia [19~21]. It is seen that their predicted angular curves are flat and do not show a peaking that is present in the data. This peaking is believed to have come from coherent scattering. A similar comparison in Figure 5.14 for the HH data reveals the same information, namely, the use of a purely coherent approach assuming independent scattering by all scatterers cannot predict the peaking that is present in the Hh data set. Finally, we show in Figure 5.15 the comparisons of VH data with the model predictions by other investigators. The model from Malaysia gives the correct level but shows a flat angular trend. The Michigan model predicts a level that is too low, because only the first-order scattering was accounted for.

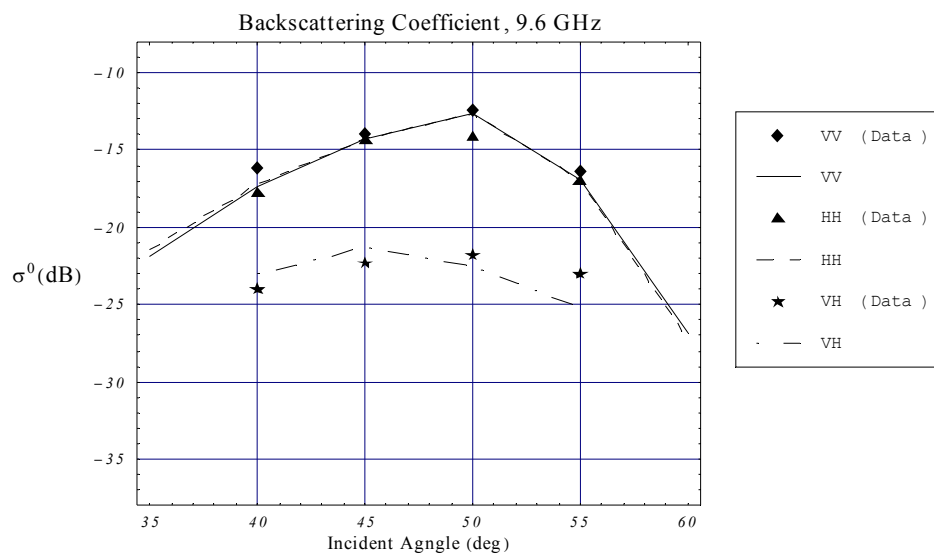


Figure 5.12 Comparison on backscattering coefficient between model predictions

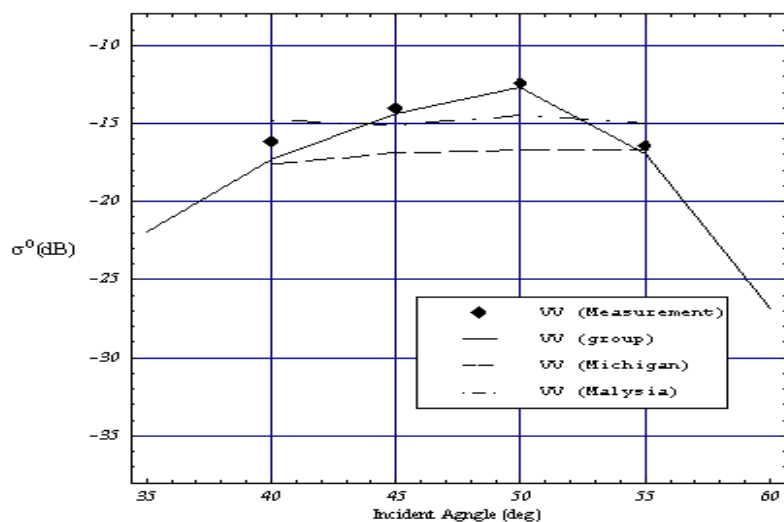


Figure 5.13 Comparison on VV backscattering coefficient between model predictions and measurement data of walnut orchard at 9.6 GHz (X-band)

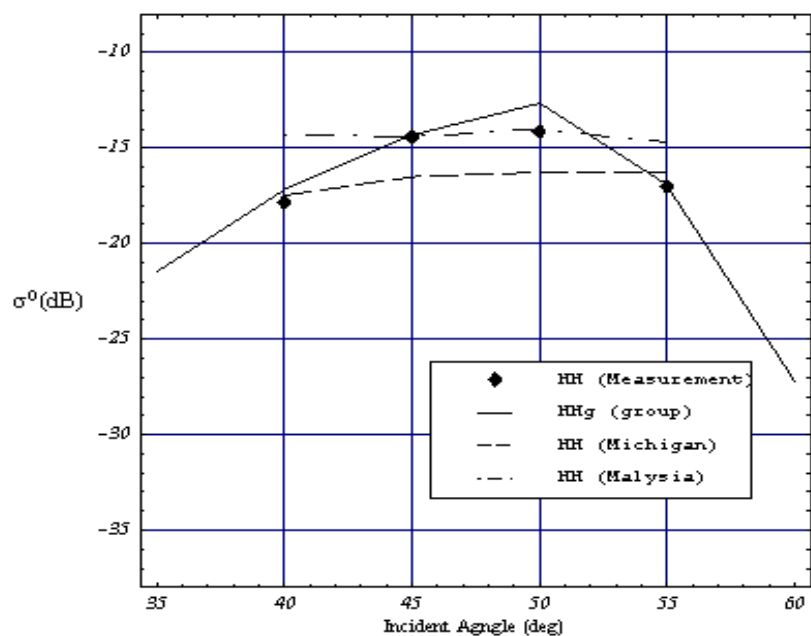


Figure 5.14 Comparison on HH backscattering coefficient between model predictions and measurement data of walnut orchard at 9.6 GHz (X-band)

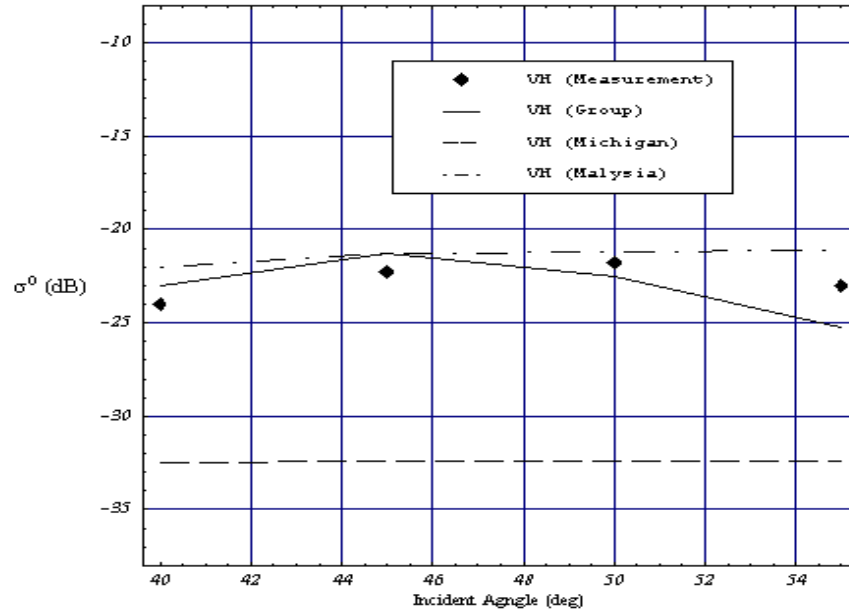


Figure 5.15 Comparison on VH backscattering coefficient between model predictions and measurement data of walnut orchard at 9.6 GHz (X-band)

### 5.3.3 Japanese Cypress

Backscattering Measurements from Japanese Cypress with and without leaves were carried out in 1986 (S-band, X-band) and 1987 (C-band) by Hirosawa et al.[22]. A single layer model constructed with randomly oriented cylinders and needles is adopted to conduct theoretical predictions based on the architecture of the Japanese Cypress. The input parameters are chosen according to the measured physical parameters given in Table 5.3.. Comparisons between model predictions and measurements with leaves at three different bands (X, C and S bands) are displayed in figures 5.16, 5.17 and 5.18 correspondingly.

According to Hirosawa et al. [22], the ground was covered with microwave absorbers. Therefore, the possible contributions from the ground and volume-ground interaction to scattering are not included in the model prediction. As seen from the figures, the model predictions are in general agreement with the data for all polarizations, VV, HH and VH and over all three frequency bands for the Japanese Cypress.

**Table 5.3. Parameters Used in the Model Computation for Comparison with Japanese Cypress Measurement**

Japanese Cypress	Parameters used in Model
Canopy height	70 cm
Needle:	
Volume fraction	0.15%
Gravimetric moisture content	58% (S and X bands) 55% (C band)
Radius	1mm
Half length	0.5cm
Branch:	
Volume fraction	0.045%
Gravimetric moisture content	58% (S and X bands) 55% (C band)
Radius	0.3cm
Length	30cm



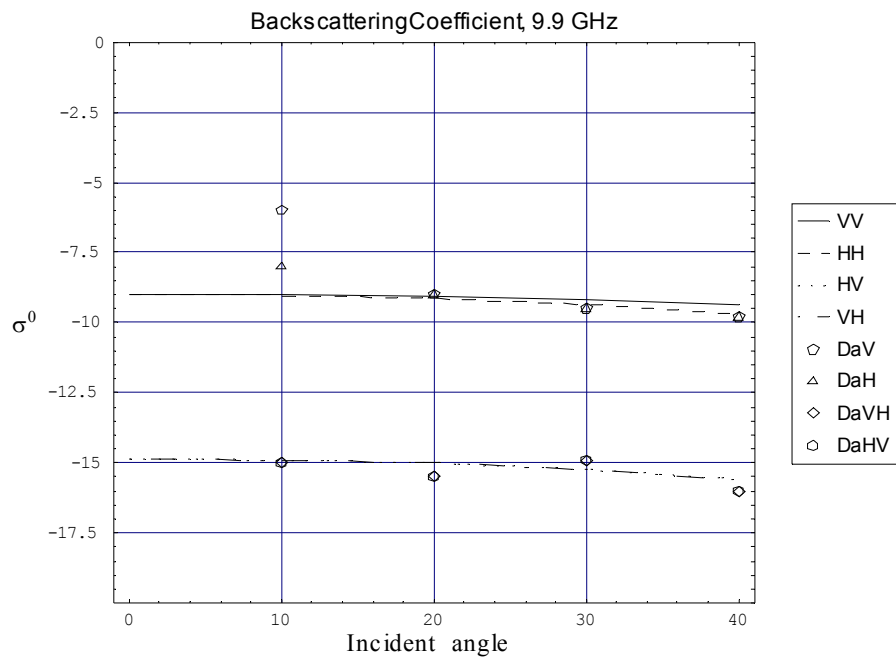


Figure 5.16 Comparison on backscattering coefficient between model predictions and measurement data of Japanese Cypress at 9.9 GHz (X-band)

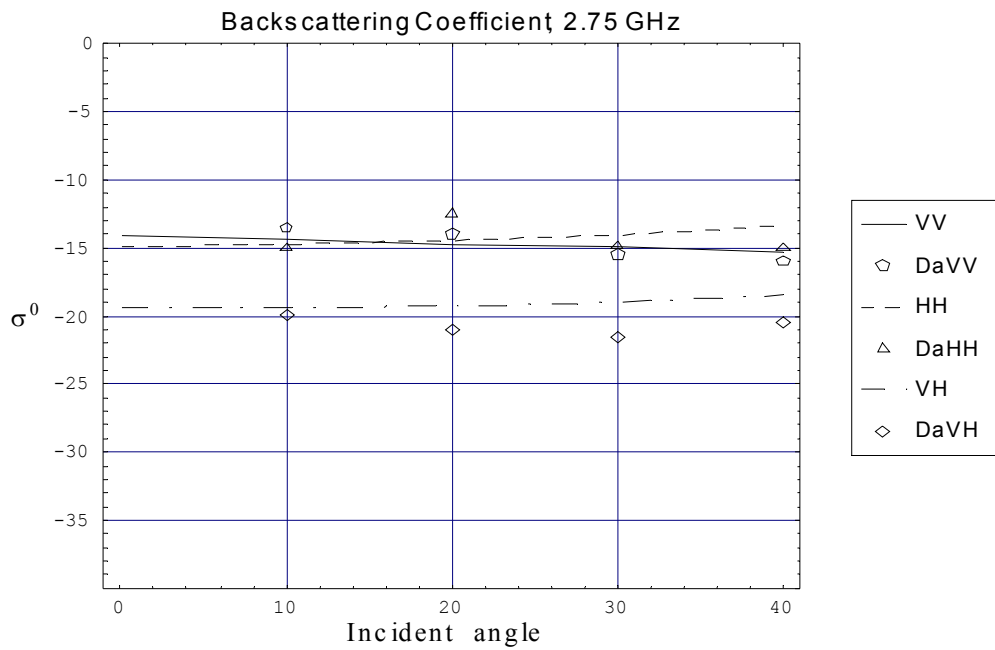


Figure 5.17 Comparison on backscattering coefficient between model predictions and measurement data of Japanese Cypress at 4.0 GHz (C-band)

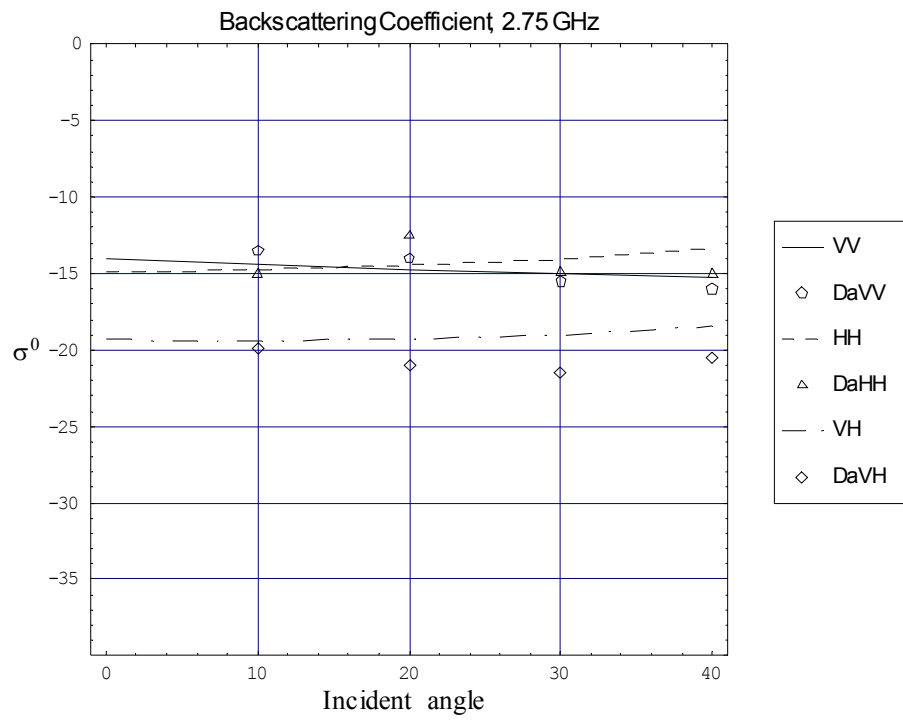


Figure 5.18 Comparison on backscattering coefficient between model predictions and measurement data of Japanese Cypress at 2.75 GHz (S-band)

## **CHAPTER 6**

### **CONCLUSIONS**

#### **6.1 General Conclusions**

In this dissertation, multilayer microwave scattering models based on the second-order solution of the radiative transfer equation have been developed to study scattering from deciduous and coniferous vegetation. The approach to the scattering phase function has generalized earlier studies on the same subject by extending the scattering phase function to include coherent scattering from a group of scatterers with a specific leaf-pattern. This is done for both the deciduous and coniferous vegetations. A real world example was given to demonstrate the need for having such a model.

#### **6.2 Future Study**

It is believed that the approach used in this study can be extended to model other vegetation types involving palmately compound leaves and even-pinnately compound leaves.

In previous field campaigns, the possible coherence effect among leaves in a group was not recognized. Hence, there was no attempt to select vegetations with compound leaves for study. As a result, there is a lack of data to verify scattering from such vegetation types. This is particularly true of coniferous vegetation.

It is also worth noting that coherence effect among leaves may change with frequency. Thus, in acquiring data multifrequency measurements are crucial for validating models and contributing to better understanding of the scattering mechanisms.

## REFERENCES

- 1 F. T. Ulaby, K. Sarabandi, K. McDonald, M. Whitt, and M. C. Dobson, "Michigan microwave canopy scattering model," *Int. J. Remote Sensing*, vol. 11, no. 7, pp. 1223-1253, 1990.
- 2 K.C. McDonald, M.C. Dobson and F.T. Ulaby, "Modeling Multi-frequency Diurnal Backscatter from a Walnut Orchard," *IEEE Trans. Geosci. and Remote Sensing*, vol. 29, No. 6, pp. 852-863, 1991.
- 3 K.C. McDonald, M.C. Dobson and F.T. Ulaby, "Using MIMICS to Model L-band Multiangle and Multitemporal Backscatter from a Walnut Orchard," *IEEE Trans. Geosci. Remote Sensing*, vol. 28, No. 4, pp. 477-491, 1990.
- 4 Lang, R. H. and J. Sidhu, "Electromagnetic Scattering from a Layer of Vegetation: A Discrete Approach," *IEEE Trans. Geosci. Remote Sensing*, vol. GE-21, pp. 67-71, 1983.
- 5 N. S. Chauhan, R. H. Lang, and K.J. Ranson, "Radar modeling of a boreal forest," *IEEE Trans. Geosci. Remote Sensing*, vol. 29, no. 4, pp. 627-638, 1991.
- 6 M. A. Karam, A. K. Fung, R. H. Lang and N. S. Chauhan, " A microwave scattering model for layered vegetation", *IEEE Trans. Geosci. Remote Sensing*, vol. 30, pp. 767-784, July 1992.
- 7 Adrian K. Fung, *Microwave scattering and emission models and their applications*, Boston, Artech House, (Chapter 11), 1994
- 8 F. Amar, "Design of an efficient retrieval scheme for forest parameters based on canopy models and radar measurements," dissertation 1996.

- 9 C. C. Hsu, H. C. Han, R. T. Shin, J. A. Kong, A. Beaudoin, and T. Le Toan, "Radiative transfer theory for polarimetric remote sensing of pine forest at P band," *Int. J. Remote Sensing*, vol. 15, no. 14, pp. 2943-2954, 1994.
- 10 S. H. Yueh, J. A. Kong, J. K. Jao, R. T. Shine, and T. Le Toan, "Branching model for vegetation", *IEEE Trans. Geosci. Remote Sensing*, vol. 30, pp. 390-402, Mar, 1992.
- 11 C. C. Hsu, "Theoretical Models for Microwave Remote Sensing of Forests and Vegetation," dissertation 1996.
- 12 T.C. Chiu, "Electromagnetic scattering from rough surfaces covered with short branching vegetation." dissertation 1998.
- 13 Y. Lin and K. Sarabandi, "A Monte Carlo coherent scattering model for forest canopies using fractal-generated trees", *IEEE Trans. Geosci. Remote Sensing*, vol. 37, pp. 440-451, Jan 1999.
- 14 T. Chiu and K. Sarabandi, "A coherent second-order scattering model for short vegetation," *Proc. IGARSS' 98*, Seattle, WA, pp. 1626-1628.
- 15 K. Sarabandi, P. F. Polatin and F. T. Ulaby, "Monte Carlo Simulation of Scattering from a Layer of Vertical Cylinders", *IEEE Trans. Geosci. Remote Sensing*, vol. 41, no. 4, April 1993.
- 16 L. Tsang, K. H. Ding, G. F. Zhang, C. C. Hsu and J. A. Kong, "Backscattering Enhancement and Clustering Effects of Randomly Distributed Dielectric Cylinders Overlying a Dielectric Half Space Based on Monte-Carlo Simulations," *IEEE Trans. Ant. and Prop.* vol. 43, no. 5, May 1995.
- 17 T. Chiu and K. Sarabandi, "Electromagnetic Scattering from Short Branching Vegetation", *IEEE Trans. Geosci. Remote Sensing*, vol. 38, no. 2, 2000.

- 18 H. T. Chuah, S. Tjuatja, A. K. Fung, and J. W. Bredow, " A phase matrix for dense discrete random medium: Evaluation of volume scattering coefficient," IEEE Trans. Geosci. Remote Sensing, vol. 34, pp. 1137-1143, Sept. 1996.
- 19 H. T. Ewe, H. T. Chuah, "Electromagnetic Scattering from an Electrically Dense Vegetation Medium," IEEE Trans. Geosci. Remote Sensing, vol. 38, No. 5, Sept. 2000.
- 20 H. T. Ewe, "A Microwave Scattering Model for an Electrically Dense Discrete Random Medium," dissertation 1999.
- 21 H. Hirosawa, Y. Matsuzaka, and O. Kobayashi, "Measurement of microwave backscatter from a cypress with and without leaves," IEEE Trans. Geosci. Remote Sensing, vol. 27, pp. 698-701, Nov. 1989.
- 22 C. Dobson, H. Stiles, D. Brunfeldt, "Data documentation: 1976 MAS 1-8 and MAS 8-18 vegetation experiments," Technical Report. RSL TR 264-15, Remote Sensing Lab, University of Kansas, Centre for Res., Inc., Lawrence, Kansas.
- 23 H. Hirosawa, H. Ishida, T. Ochi and Y. Matsuzaka, "Measurement of microwave backscatter from trees," Proceedings of the 3th International colloquium on Spectral Signatures of Objects in Remote Sensing, Les Acs, France.
- 24 G. W. D. Symonds, The Tree Identification Books: A New Method of the Practical Identification and Recognition of Trees, Quill, New York, 1958.
- 25 Mostafa A. Karam, Adrian K. Fung, "Scattering from Randomly Oriented Circular Discs with Application to Vegetation", Radio Science, Vol. 18, pp. 557-565, July-August, 1983.
- 26 Mostafa A. Karam, Adrian K. Fung, "Leaf Shape Effects in Electromagnetic Wave Scattering from Vegetation", IEEE Transaction on Geoscience and Remote Sensing, pp. 687-697, Vol. 27, NO. 6, November 1989

- 27 Mostafa A. Karam, Adrian K. Fung, Yahia M. M. Antar, Electromagnetic wave scattering from some vegetation samples, IEEE Transaction on Geoscience and Remote Sensing, issue 6, pp. 799-808, vol. 26, Nov., 1988.
- 28 C. Acquista, "Light Scattering by tenuous particles: a generalization of the Rayleigh-Gans-Rocard Approach", Appl. Opt., Vol. 15, No. 11, pp. 2932-2936, 1976.
- 29 H. C. Van de Hulst, "Light Scattering by Small Particles", New York: Dover, 1981.
- 30 J. A. Osborn, "Demagnetizing factors of the general ellipsoid", Phy. Rev., vol. 67, pp. 351-357, 1945.
- 31 N. G. Khlebtsov, "Integral Equation for Problems of Light Scattering by Particles of the Medium", Opt. Spectrosc. (USSR). vol. 57, no. 4, pp. 399-402, 1984.
- 32 R. Schiffer and K. O. Thielheim, "Light Scattering by dielectric needles and disks", J. Appl. Phys., Vol. 50, No. 4, pp. 2476-2483, 1979.
- 33 M.A. Karam and A.K. Fung, "Electromagnetic Scattering from a layer of finite randomly oriented, dielectric circular cylinders over a rough interface with application to vegetation", Int. J. Remote Sensing, Vol. 9, No. 6, pp. 1109-1134, 1988.
- 34 M. A. Karam and A. K. Fung, "Propagation and Scattering in Multilayered random media with rough interfaces," Electromagnetics, Vol. 2, pp. 239-256, 1982.
- 35 A. Ishimaru, "Wave Propagation and Scattering in Random Media", Academic Press, New York, 1978.
- 36 L. Tsang, J. A. Kong, and R.T. Shin, "Theory of Microwave Remote Sensing", John Wiley & Sons, New York, pp. 139-140, 1985.
- 37 A. Ishimaru and R.L.T. Cheung, "Multiple Scattering Effects on Wave Propagation due to Rain", Ann. Telecommunication, Vol. 35, pp. 373-379, 1980.

- 38 L. Tsang and J.A. Kong, "Radiative Transfer Theory for Active Remote Sensing of Half Space Random Media", Radio Science, Vol. 13, 1978, pp. 763-773.
- 39 M.A. Karam, F. Amar, A.K. Fung, E. Mougin, A. Lopes and D.M. Levine, "A Microwave Scattering Model for a Forest Canopy Based on Vector Radiative Transfer Theory", Remote Sensing of Environment, Vol. 53, No. 1, 1995.
- 40 J. Cimino, M. C. Dobson, D. Gates, E. Kasischke, R. Lang, J. Norman, J. Paris, F. T. Ulaby, S. Ustin, V. Vanderbilt, and J. Wber, "EOS synergism study 1987 field experiment data report", JPL Tech. Rep., May 1988.
- 41 E. X. Huang and A. K. Fung, " Electromagnetic Wave Scattering from Vegetation with Odd-Pinnate Compound Leaves", Journal of Electromagnetic Wave and Applications, Vol. 19, issue 2, pp. 231-244, 2005.
- 42 Tsang, L., M. C. Kubaschi, and J. A. Kong, "Radiative transfer theory for active remote sensing of a layer of small ellipsoidal scatterers", Radio Science, 16(3), 321-329, 1981.



## BIOGRAPHICAL STATEMENT

Xiaoyan Huang joined University of Texas at Arlington since August 2000. Before she joined the UTA, she was a software engineer in IEI Technology (China) Ltd, Beijing. Her research interest is in computational electromagnetics, wave scattering and emission from rough surface and random media, and medical imaging processing.